POLITECNICO DI TORINO

Collegio di Ingegneria Chimica e dei Materiali

Master of Science Course
in Chemical and Sustainable Processes Engineering

Master of Science Thesis

Influence of preparation mode for supported $NiFe/CeO_2$ bimetallic catalysts for dry reforming in a fixed bed reactor

Tutor

Eng. Giuseppe Pipitone

Co-Tutor

Prof. Lluís Soler

Candidate

Adriana Parisi

Alla mia famiglia, che mi ha insegnato il valore
dei sogni e della perseveranza.
Spero di rendervi sempre orgogliosi di me.

A me stessa, alla mia determinazione, ai miei sogni.

Attraverso le difficoltà, verso le stelle.

Tables of Contents

Abstract

The increase in greenhouse gases, particularly CO2 and CH4, represents a significant challenge for environmental sustainability. The dry reforming of methane (DRM) converts CH_4 and CO_2 into syngas, which can be utilized in fuel production and other chemical processes. This study examines the catalytic performance of Ni-based catalysts supported on CeO2, focusing on the effect of Fe addition and comparing two synthesis methods: incipient wetness impregnation (IWI) and ball milling (BM).

All experiments were conducted in a fixed-bed reactor using a gas mixture (CH4, CO2, and N2) with a total flow rate of 125 mL/min at atmospheric pressure. Activity and selectivity tests were carried out at temperatures ranging from 550°C to 950°C, with 50°C increments and a one-hour reaction period per interval. Stability tests were performed at 700°C over 24 hours.

Activity and selectivity results indicate that the bimetallic catalyst with 8 wt% Ni and 2 wt% Fe exhibits significantly higher catalytic activity and selectivity than the other two catalysts, which differ in composition, regardless of the synthesis method employed. Specifically, at 750°C, the BM-prepared bimetallic catalyst with 2wt% Fe achieved an average CH4 conversion of 80%, whereas monometallic catalysts and those with lower Fe content reached conversions of 45% and 50%, respectively.

The influence of synthesis methods was further investigated by comparing BM and IWI catalysts. Although the BM catalyst demonstrated slightly higher average values in reagent conversion and H2/CO ratio, the performance differences between BM and IWI remained within error margins, indicating similar effectiveness across methods.

Catalyst stability was evaluated on the two bimetallic catalysts with 2 wt% Fe, synthesized by BM and IWI. Both catalysts exhibited deactivation, with an initial CH4 conversion above 80% that decreased to less than 15% after 24 hours. However, the BM catalyst displayed a more linear and less pronounced deactivation trend.

Characterization through XPS, SEM, and Raman spectroscopy revealed structural differences between Ni-Fe catalysts synthesized by BM and IWI. BM catalysts presented a larger specific surface area and a higher surface concentration of Ni, which enhance active site accessibility and catalytic activity compared to IWI catalysts. Although both catalysts showed tendencies toward deactivation, the structural properties of BM catalysts improve operational stability, reducing susceptibility to deactivation and coke formation.

In conclusion, Ni-Fe bimetallic catalysts, especially those synthesized by BM, show considerable promise as alternatives to Ni monometallic and costly platinum-group metal-based catalysts. The synergy between Ni and Fe provides an economically advantageous and sustainable catalytic solution for DRM, with BM synthesis enhancing both catalytic efficiency and stability.

List of Figures

List of Tables

List of Abbreviations

Abbreviation	Definition
ATR	Autothermal Reforming
BM	Ball Milling
COPrOX	Carbon monoxide preferential oxidation
DRM	Dry reforming of methane
GHGs	Greenhouse gases
GHSV	Gas hourly space velocity
IEA	International Energy Agency
IWI	Incipient Wetness Impregnation
OSC	Oxygen Storage Capacity
POX	Partial Oxidation
RWGS	Reverse water-gas shift
SEM	Scanning Electron Microscopy
SR	Steam Reforming
WGS	Water-gas shift
XPS	X-ray Photoemission Spectroscopy

1. Introduction

1.1 The current Energy Scenario

The rapid growth of the global population and increasing industrialization have intensified the need for alternative energy sources. Our predominant reliance on fossil fuels presents significant challenges due to their finite availability and the greenhouse gas (GHG) emissions they produce. As fossil fuel reserves deplete and concerns about climate change rise, governments are investing more in strategies to minimize environmental impact. According to data from the International Energy Agency (IEA), carbon dioxide (CO_2) emissions from the fossil fuel sector reached record levels in 2022 (Mhadhbi, 2024).

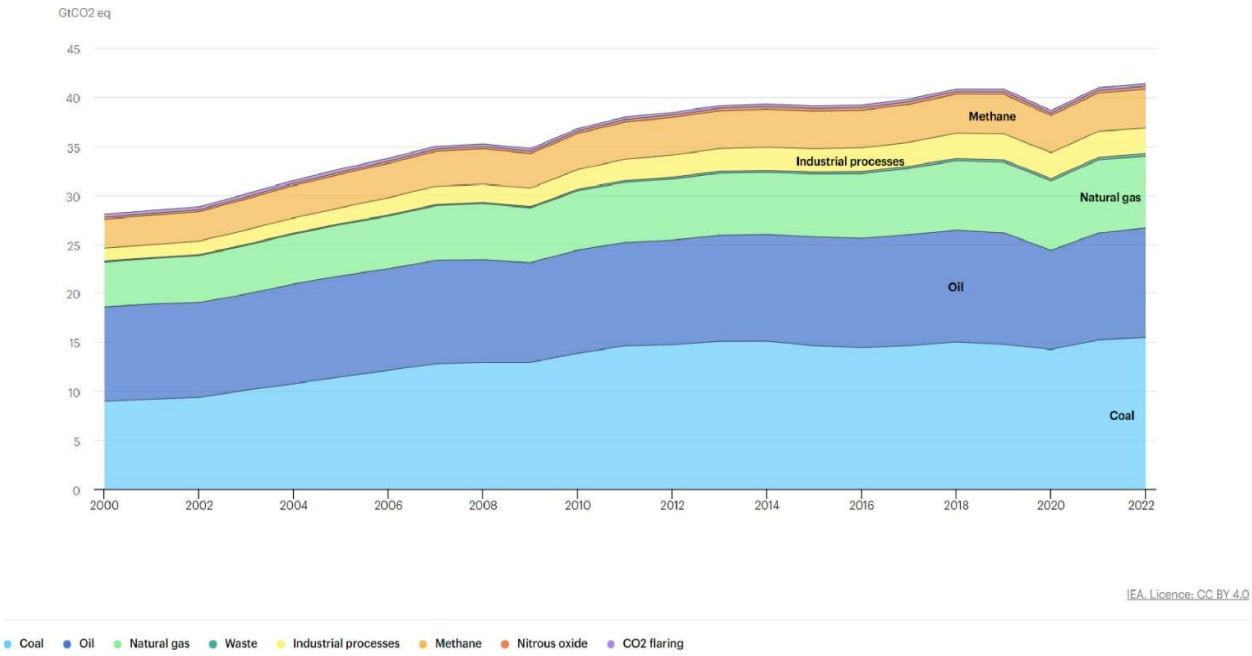

***Figure 1**: Global energy-related greenhouse gas emissions, 2000–2022 (Mhadhbi, 2024).*

In response, there is a shift towards renewable energy sources such as solar, wind, and hydroelectric power, offering a hopeful path for the future. In addition, there is a growing recognition of the importance of energy efficiency and sustainable practices across industries. Innovations in energy storage technologies and smart grid systems are essential for integrating renewable energy into existing infrastructure.

Despite these efforts, transitioning to a low-carbon economy remains a complex and multifaceted challenge. Socioeconomic factors, geopolitical considerations, and technological barriers contribute to the complexity of the transition process. Furthermore, meeting the ambitious goals of international agreements like the Paris Agreement, which aims to limit global temperature rise to 1.5 °C above pre-industrial levels, requires not just coordinated global action, but a sense of unity and collaboration. Addressing the urgent challenges of climate change and ensuring a sustainable energy future demands an integrated approach considering environmental, social, and economic factors. By embracing innovation, fostering partnerships, and implementing effective policies, we can create a more resilient and equitable energy landscape.

Uncontrolled emissions of greenhouse gases contribute to global warming through *the greenhouse effect*. While this effect is beneficial in retaining some solar radiation and maintaining a stable temperature, excess greenhouse gases trap more heat, causing a harmful temperature rise. This situation disrupts ecosystems and natural balance, posing significant consequences.

Carbon dioxide is the primary greenhouse gas, but other substances, like methane (CH_4), have a higher warming potential per unit. Therefore, GHGs are often measured in terms of carbon dioxide equivalents (CO_2eq) (Filonchyk et al., 2024).

The energy sector is responsible for about two-thirds of total anthropogenic GHG emissions, highlighting the need for investment in infrastructure and research to ensure climate stability. Completely replacing fossil fuels is challenging, especially with rising energy demand. The global population is projected to grow from 8 billion to approximately 9.7 billion by 2050 (*Population Pyramids of the World from 1950 to 2100*, n.d.).

The European Union has proposed a binding agreement with member states to reduce carbon emissions by 30% by 2030 (European Commission, n.d.). Similarly, the World Energy Outlook 2020 advocates for net-zero emissions by 2050, outlining necessary measures for gradual emission reductions. Four trends drive the future of global energy: reduced reliance on hydrocarbons, rapid growth in renewables, increased electrification, and greater use of low-carbon hydrogen (Energy Outlook, 2023). Hydrogen (H_2) has significant potential for a sustainable energy system, with its share in the total energy consumption expected to grow from 0.2% in 2020 to 15% by 2050 (Scheller et al., 2023).

1.2 Hydrogen

Experts recognize hydrogen (H_2) as a crucial energy carrier during the transition toward sustainable energy. Despite lingering uncertainties surrounding the development of production, transportation, and storage costs, hydrogen has the potential to play a pivotal role in energy transition strategies and

trajectories. While its current applications are primarily concentrated in the fertilizer, refining, and petrochemical sectors, there is growing anticipation that renewable hydrogen could decarbonize challenging sectors like steel production and other energy-intensive industrial processes. Moreover, hydrogen is considered a valuable energy storage solution, particularly for managing the variability and intermittence of renewable energy sources within the power grid (Seck et al., 2023a).

1.2.1 Properties of Hydrogen

Hydrogen, represented by the chemical symbol H, occupies the first position in the periodic table, making it the lightest element with an atomic mass of 1.00794 atomic mass units. Two hydrogen atoms can covalently bond to form a diatomic molecule, denoted as H_2. This molecule is a colorless, odorless, and tasteless gas, highly flammable, and is typically produced under standard atmospheric pressure and room temperature conditions (Hydrogen | H2 | CID 783 - PubChem).

***Table 1**: Properties of Hydrogen (H_2).*

PROPERTY	VALUE	UNIT OF MEASUREMENT
Molecular Weight	2.016	g/mol
Gas density (at 0 °C and 1 atm)	0.0899	kg/m^3
Boiling point	-253	°C
Melting point	-259	°C
Auto-ignition Temperature	560	°C
Explosive limits	4 -75	% vol in air
Vapor Pressure (at 25 °C)	165320	kPa
Solubility in water (at 21 °C)	1.62	mg/l

Hydrogen is the most abundant element, constituting approximately 93% of the universe. However, due to its reactivity, the amount of molecular hydrogen under normal conditions on Earth is meager (Eric Hand, 2023).

In contrast, the presence of hydrogenated compounds, such as water and hydrocarbons, is exceptionally high. This abundance allows the extraction and synthesis of hydrogen from various sources. The selection of appropriate origins is crucial because it determines the environmental impacts of hydrogen production.

Hydrogen's versatility positions it as a key player in future energy landscapes. With its high gravimetric energy density and eco-friendly electrochemical conversion in Fuel Cell devices, hydrogen is poised to lead the charge in clean energy transitions. Its potential extends beyond fuel, offering solutions for energy storage, transportation, and industry. As markets and technology progress, we expect hydrogen's diverse applications to fuel innovation and make significant strides toward combating climate change and achieving sustainability objectives.

1.2.2 Hydrogen Economy

Although the "hydrogen economy" concept originated in the 1970s, its energy model has not yet achieved widespread implementation. Currently, industries predominantly use hydrogen as a commodity chemical, with a global production of ca. 95 MTn/year. H_2 is mainly employed in ammonia production, which consumes approximately 54% of it, refineries and the chemical industry, which use 35%, methanol production, which takes 6%, and other industrial sectors that utilize the remaining 5% (Maria Valenti, 2009). Nevertheless, most of the H_2 consumed in these processes is linked to CO_2 emissions through the methane steam reforming reaction to produce it. Now, there is a pressing need to broaden the utilization of hydrogen within the global energy sector, thereby harnessing its potential to enhance overall sustainability.

Hydrogen is not a primary energy source like oil, natural gas, wind, or solar power. Instead, it is an energy carrier capable of transferring energy from one form to another. Therefore, it is required a primary energy source to produce H_2 molecules. There are multiple advantages associated with the use of hydrogen as an energy vector:

- The combustion of hydrogen is considered highly clean, as it primarily produces water as the only byproduct. The reaction stoichiometry is as follows:

  $$H_2 + \frac{1}{2}O_2 \leftrightarrow H_2O \quad (1)$$

  Unlike other energy vectors, this process avoids the synthesis of CO_2 and other greenhouse gases (GHGs), such as SO_2. However, if air is used as the oxygen source, the nitrogen present in the air can react at high temperatures to form nitrogen oxides (NO_x), thus not entirely eliminating pollutant emissions.
- It is possible to produce H_2 from different primary resources.
- This component exhibits a significantly higher gravimetric energy content compared to alternative energy vectors. It is estimated to be 141.6 MJ/kg (39.3 kWh/kg), in contrast to the 44.4 MJ/kg (3.12 kWh/kg) found in gasoline.

At the same time, it is necessary to consider the following drawbacks to obtain a clear overview of this energy carrier:

- The energy loss is inevitable during the transformation from one energy form to another.
- Economic and technological competitiveness has yet to be achieved to enable production from renewable sources (electrolysis and other emerging processes such as photocatalysis, photoelectrocatalysis or thermochemical cycles, among others).
- The volumetric energy density of H_2 is very low, around 0.010–0.011 MJ/L for gaseous hydrogen at 1 bar and 20°C. Consequently, storing or using hydrogen at atmospheric pressure and temperature requires a substantial amount of space. Fortunately, there are solutions to this issue. By compressing hydrogen to high pressures or liquefying it, the volumetric energy density can be significantly increased, making storage and transportation more practical (even if more expensive as well).
- Storage and distribution techniques are still evolving.

Although uncertainties persist regarding the advancement of production, transportation, and storage costs associated with hydrogen, it can be a pivotal component within energy transition strategies and pathways (Seck et al., 2023b).

1.2.3 Synthesis Methods

Estimates indicate that industries produce 95 million tons of hydrogen yearly, and they project their consumption to increase by around 6% annually (Internation Energy Agency, 2023). Hydrogen production is primarily based on two processes: reforming or partial oxidation of hydrocarbons and water electrolysis. However, the majority is currently derived from the first process, as water electrolysis accounts for only a small percentage of global hydrogen production.

Reforming and partial oxidation processes transform hydrocarbons into a gaseous mixture enriched with hydrogen. Specifying that the feedstocks employed may originate from fossil sources, such as natural gas and coal, or from renewable sources, using specific biomass, is essential. Therefore, hydrogen production can be sourced from various energy reservoirs, enabling each country to optimize resource utilization more efficiently. Processes implemented on an industrial scale rely on the use of fossil sources and include steam reforming (SR), partial oxidation (POX), and autothermal reforming (ATR).

Steam reforming (SR) is characterized by high efficiencies and low operational and production costs, making it one of the most widely used industrial processes, especially in the chemical and petrochemical industries. The predominant raw material is natural gas, from which methane (CH_4) can be extracted; however, multiple alternatives exist, including ethanol (Braga et al., 2023).

The SR reaction is catalytic and requires specific catalysts to lower the activation energy and enhance the reaction rate. The properties of these catalysts are influenced by both the active phase and the support used. While noble metals like Platinum (Pt), Palladium (Pd), Ruthenium (Ru), and Rhodium (Rh) are

highly active in this reaction, their high cost makes them impractical for industrial-scale applications. Instead, Nickel-based catalysts are preferred because of their favorable combination of stability, activity, and cost-effectiveness (Ladna & Gam, 2010). In addition to the active phase, the catalyst's activity is also correlated with the support used, which must ensure thermal stability and a high surface area for metal adhesion.

In the overall reaction scheme, it is necessary to consider a purification pretreatment to remove sulphur, as this component acts as a poison for the catalysts employed in the process. Following this reaction, the feed undergoes preheating before entering the reactor, where steam reforming (SR) and the *water-gas shift* (WGS) reaction occur.

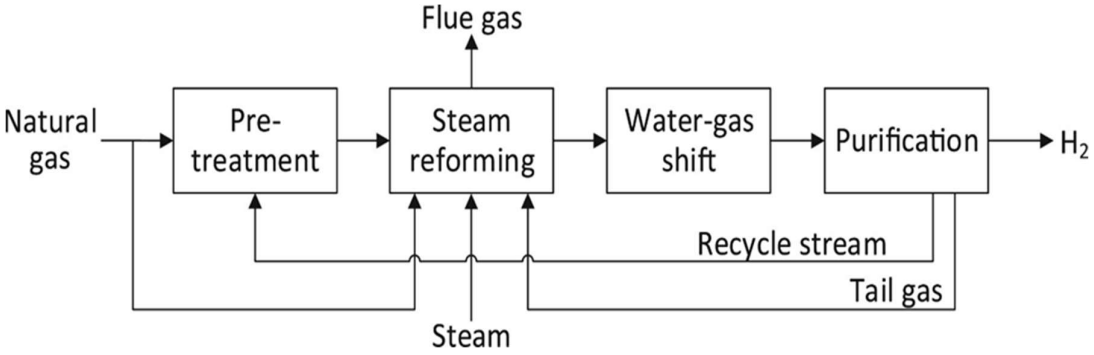

***Figure 2**: Process steps of H_2 production by methane steam reforming (Hermesmann & Müller, 2022).*

$$CH_4 + H_2O \leftrightarrow CO + 3H_2 \qquad (\Delta rH° = +206.3\ kJ/mol) \qquad (2)$$

$$CO + H_2O \leftrightarrow CO_2 + H_2 \qquad (\Delta rH° = -41.2\ kJ/mol) \qquad (3)$$

Due to its endothermic nature, the Methane Steam Reforming reaction (2) requires high temperatures, typically between 700°C and 1100°C. In industrial settings, this reaction is conducted under high pressures, normally ranging from 3 to 25 bar, to minimize the operational volume of the reactor and streamline subsequent compression stages (Castro-Dominguez et al., 2016). However, this operational setup is thermodynamically disadvantageous, resulting in reduced methane conversion. To overcome this challenge, higher temperatures are employed, along with an excess of steam, S/C=3, compared to the stoichiometric quantity required, S/C=1. The water-gas shift reaction (3) is slightly exothermic and supplies heat in situ through proper recirculation. However, this heat is not sufficient to sustain the endothermic SMR reaction, which still requires substantial external heat input for efficient operation. . Moreover, the WGS reaction decreases the CO content while increasing the hydrogen concentration in the outgoing stream.

In addition to the primary reactions driving syngas production, secondary reactions that lead to the formation of by-products must also be considered.

$$2CO \leftrightarrow C + CO_2 \qquad (\Delta rH° = -172\ kJ/mol) \qquad (4)$$

$$CH_4 \leftrightarrow C + 2H_2 \qquad (\Delta rH° = +75\ kJ/mol) \qquad (5)$$

$$C + H_2O \leftrightarrow CO + H_2 \qquad (\Delta rH° = +131\ kJ/mol) \qquad (6)$$

The *Boudouard reaction* (4) occurs within a temperature range of 450-600°C, typically occurring downstream of the reactor due to the subsequent rapid temperature reduction. Simultaneously, the methane cracking reaction (5) facilitates additional hydrogen production but also leads to coke formation, which can potentially deactivate the catalyst. In addition, the gasification reaction (6) is characterized by its heterogeneous nature and low reaction rate. As a concluding step, removing CO and CO_2 is imperative to enhance the purity of the outlet stream. CO_2 elimination involves absorption processes that employ either chemical or physical methods depending on the chosen solvent. Meanwhile, CO is usually separated from the H_2 stream through methanation, a process opposite to SR, but preferential oxidation of carbon monoxide (COPrOX) units can be also employed (Poggio-Fraccari et al., 2022).

Another alternative process for syngas production is *partial oxidation* (POX): it is a non-catalytic reaction that operates with nonstoichiometric fuel-to-air mixtures at high temperatures (1300-1500 °C) and elevated pressures. Alternatively, thanks to the addition of an appropriate catalyst, it is possible to reduce the operating temperature to approximately 700-900°C and the pressure to 1 atm. The reaction scheme, considering the use of methane, is as follows:

$$CH_4 + \frac{1}{2}O_2 \leftrightarrow CO + 2H_2 \qquad (\Delta rH° = -35.9\ kJ/mol) \qquad (7)$$

In this reaction scheme, it is essential to consider the second synthesis step characterized by the water-gas shift (3), which enhances the overall hydrogen yield. Finally, separation technologies remove any by-products similar to those used in the preceding steam reforming reaction.

The reaction exhibits significant exothermicity, releasing heat that renders this technology less energy-intensive than SR. It is estimated that POX requires 10-15% less energy compared to conventional SRM processes (Freni et al., 2000).

POX can be carried out under high gas hourly space velocity (GHSV), which translates to lower investment and production scale to achieve the same capacity as SRM (Khajenoori et al., 2013). In fact, while in SRM the contact time is on the order of seconds, in POX the contact time is on the order of milliseconds, leading to an estimated 25-30% lower capital investment compared to SRM (Freni et al., 2000).

Nonetheless, there are associated challenges, including the elevated expenses linked to pure oxygen utilization and safety issues due to the mixture's explosive potential. Indeed, hydrogen exhibits a broad range of flammability.

Catalysts commonly employed for converting natural gas typically consist of Nickel (Ni) or Rhodium (Rh). However, Nickel tends to undergo coking, while the cost of Rhodium has surged significantly. The thermal efficiency of Partial Oxidation (POX) reactors using methane as a fuel generally falls within 60% to 75% (Kalamaras & Efstathiou, 2013b).

Another technology for hydrogen synthesis from hydrocarbon fuels is autothermal steam reforming (ATR), which is a combination of steam reforming (SR) and partial oxidation (POX) processes. In this way, the overall reaction scheme does not require any significant external heat exchange, such as for fuel preheating.

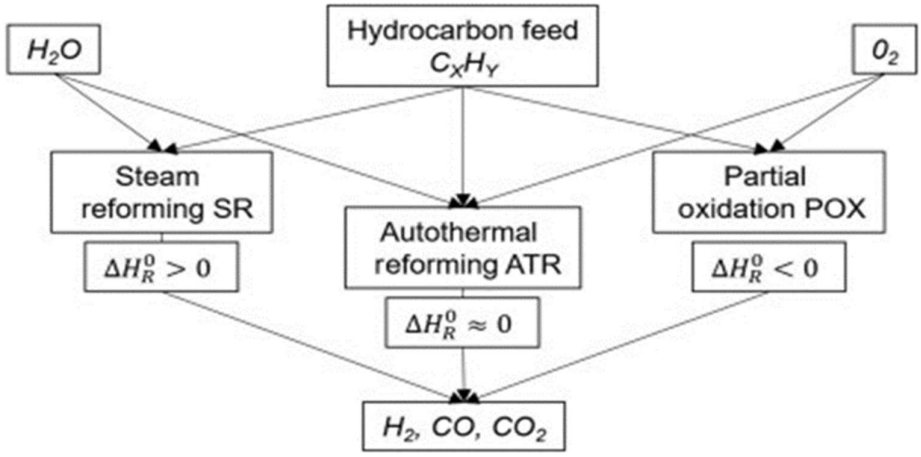

***Figure 3**: Autothermal reforming as a combination of steam reforming and partial oxidation* (Jordan, 2022).

The reaction scheme involves the sum of the reagents and products highlighted in the two previously discussed reactions.

The ATR method integrates the energetic properties and materials and incorporates various other factors, such as efficiency and hydrogen yield, typically around 40%. It emerges as the preferred reforming approach for small-to medium-scale applications, offering the flexibility to use air instead of oxygen, thereby substantially simplifying system complexity.

After thoroughly analyzing these three processes, it becomes evident that they are extensively studied and commonly applied in industrial contexts. However, it is crucial to recognize that each reaction pathway leading to H_2 synthesis presents distinct advantages and disadvantages. In the table below, it is possible to summarize the key points of the different reaction schemes.

***Table 2**: Comparison of the three processes* (Manna, 2024).

PROCESS	ADVANTAGES	DISADVANTAGES
Steam Reforming (SR)	• Mature technology with extensive industrial experience • Oxygen is not needed • Lowest process temperature • Best H_2/CO ratio for H_2 production	• Highest emissions
Partial Oxidation (POX)	• Desulphurization requirement is minimum • A catalyst is not required • Low methane slip	• Low H_2/CO ratio • Soot formation • Require oxygen
Autothermal Reforming (ATR)	• Lower process temperature than POX • Low methane slip	• Limited industrial experience • Require oxygen or air

Among the synthesis routes explained and analyzed previously, dry methane reforming (DRM) stands out as a promising method for utilizing both CO_2 and CH_4 to produce syngas with a desirable H_2/CO ratio of approximately 1. This process not only offers an efficient way to convert greenhouse gases into valuable chemicals but also provides a feedstock suitable for subsequent synthesis processes such as Fischer-Tropsch synthesis and methanol production (Bahari et al., 2024). Detailed mechanisms, catalytic systems, and the thermodynamic and kinetic aspects of the dry methane reforming reaction will be discussed comprehensively in Chapter 3.

In contrast to traditional fossil fuel reforming processes, water electrolysis emerges as a promising technology for sustainable hydrogen generation. This method uses electrical energy to induce a redox reaction that decomposes water into its elemental components, hydrogen and oxygen, in the form of gases (Bossel & Eliasson, n.d.). While water electrolysis requires significant energy consumption, primarily to overcome the water's bond energy and resistive losses within the electrolytic system, it offers crucial advantages in terms of environmental sustainability and energy independence.

Currently, only about 4% of the global hydrogen production originates from this method, largely due to economic challenges related to energy efficiency (Bossel & Eliasson, n.d.). However, ongoing research and technological advancements aim to improve the efficiency and reduce the costs of water electrolysis, making it an increasingly competitive solution for clean and renewable hydrogen production.

1.3 Biogas

As the world transitions towards a low-carbon economy, both hydrogen and biogas have emerged as significant renewable energy sources in reducing carbon emissions. In previous sections, we explored the potential of hydrogen to play a key role in this shift. However, hydrogen is not the only alternative; biogas also offers substantial benefits that complement those of hydrogen, reinforcing the global effort to mitigate climate change and promote sustainability.

Biogas is a renewable energy source produced through the anaerobic digestion of organic matter, like plant and animal waste. This process, facilitated by various microorganisms, particularly methanogenic bacteria, results in a mixture of gases primarily composed of methane (CH_4) and carbon dioxide (CO_2), with trace amounts of hydrogen sulfide (H_2S) and nitrogen (N_2). The typical composition of biogas is about 55-70% methane and 30-40% carbon dioxide. The higher the methane content, the greater the energy efficiency of the biogas (Jameel et al., 2024).

The production of biogas offers several environmental and economic benefits, making it an ideal alternative energy source. It provides a sustainable way to manage organic waste, converting it into valuable energy and nutrient-rich fertilizer. This not only reduces environmental pollution but also enhances soil quality and agricultural productivity. Furthermore, the combustion of biogas results in a net reduction of greenhouse gas emissions. Methane, the primary component of biogas, is 21 times more effective at trapping heat in the atmosphere than carbon dioxide. By capturing and utilizing methane from organic waste, biogas production helps mitigate climate change (Christopher A. Badurek, 2024).

Biogas is a versatile energy source with multiple applications. It can be used directly for heating and lighting or converted into electricity through combustion engines or turbines. The integration of biogas into the energy mix supports the transition to a low-carbon economy by providing a renewable and sustainable alternative to fossil fuels. Additionally, biogas production contributes to improved public health and sanitation by reducing the odors, insects, and pathogens associated with traditional manure stockpiles (Jameel et al., 2024).

The adoption of biogas technology aligns with the principles of a circular economy, emphasizing nutrient recycling, greenhouse gas emission reduction, and bioremediation. By incorporating biogas into the broader energy strategy, we can enhance energy diversification and resilience, reduce dependence on non-renewable energy sources, and promote a more sustainable and environmentally friendly energy future.

In conclusion, biogas, alongside hydrogen, plays a crucial role in the transition towards a low-carbon economy. Its environmental benefits, coupled with its role in renewable energy generation and waste management, make biogas an indispensable resource in the global effort to reduce carbon emissions and

promote sustainability. As we move forward, the continued development and integration of biogas technologies will be essential in achieving our environmental and energy goals.

1.4 Syngas

Nowadays, syngas (synthesis gas) has emerged as a versatile and valuable renewable energy source, complementing other alternative fuels like hydrogen and biogas. Syngas is a highly combustible mixture primarily composed of hydrogen (H_2) and carbon monoxide (CO), with smaller amounts of carbon dioxide (CO_2) and methane (CH_4). This gas is used extensively in the production of hydrocarbon fuels, like diesel and methanol, and industrial chemicals, particularly ammonia. When derived from waste materials and biomass, syngas represents a form of renewable energy that contributes significantly to reducing carbon emissions and promoting environmental sustainability (Khosravani et al., 2023).

The utility of syngas as a fuel was notably realized during World War II in Germany when gasoline shortages necessitated alternative fuels for transportation. At the time, processes like the Bergius process, developed by Friedrich Bergius, and the Fischer-Tropsch (FT) reaction, developed by Franz Fischer and Hans Tropsch, were employed to convert coal into liquid hydrocarbons. Today, syngas is primarily generated through the thermal conversion of biomass by gasification, a process that involves the steam reforming of methane or partial oxidation. At high temperatures, and in the presence of steam or oxygen, gasification converts carbon-containing materials into hydrogen, carbon monoxide, and carbon dioxide, without requiring combustion. This method can achieve conversion rates exceeding 99%, making it highly efficient (Rogers Kara, 2023).

Syngas production involves several steps, starting with the selection of feedstock, which can include natural gas, coal, or various hydrocarbons. Natural gas, mainly composed of methane, is the most common and cost-effective feedstock for syngas production. Given that methane emissions significantly contribute to global warming, developing technologies to convert methane into valuable products is crucial. Conventional processes for producing syngas from methane include steam reforming, dry reforming, and partial oxidation, with newer technologies such as plasma processes also being explored (Rogers Kara, 2023).

Once produced, syngas must be purified to remove harmful contaminants like hydrogen chloride and coal tar. Clean syngas can be burned like natural gas, with a portion used to power the gasification plant itself and the remainder sold to utility companies for electricity production. The environmental benefits of using syngas are substantial, as it not only reduces reliance on fossil fuels but also repurposes waste materials, thereby reducing pollution and greenhouse gas emissions.

The applications of syngas are diverse and impactful. It serves as a critical intermediate for manufacturing chemicals such as ammonia, methanol, and synthetic hydrocarbon fuels. In the Fischer-Tropsch process, syngas is converted into synthetic crude oil, lubricants, and various hydrocarbon fuels. The versatility of syngas extends to its use in producing hydrogen, which is essential for making numerous chemicals (Khosravani et al., 2023).

Despite its advantages, using syngas as a fuel presents certain challenges. The presence of moisture and tars in the feedstock can complicate the gasification process, and the high combustibility of hydrogen necessitates modifications to internal combustion engines to prevent preignition and backfiring. Even with such modifications, engine output may be reduced. Nonetheless, the benefits of syngas as a renewable energy source far outweigh these challenges (Khosravani et al., 2023).

In conclusion, syngas is a crucial component of the low-carbon economy, offering a renewable and efficient alternative to traditional fossil fuels. Its production from various feedstocks, including waste and biomass, supports environmental sustainability and energy diversification. By integrating syngas into the broader energy strategy, we can reduce carbon emissions, promote cleaner industrial processes, and enhance energy security. As we move towards a more sustainable future, the continued development and utilization of syngas technologies will play a vital role in achieving our environmental and energy goals.

1.5 Aims of this thesis

The primary focus of this study is to investigate the synthesis of Syngas mixture through the dry reforming reaction. This process, which involves the conversion of two major greenhouse gases, carbon dioxide (CO_2) and methane (CH_4), into carbon monoxide (CO) and hydrogen (H_2), holds significant promise. By using these gases as feedstocks, we not only have the potential to reduce environmental pollution but also to produce valuable energy carriers. A key aspect of this investigation is the synthesis and characterization of the catalyst, which will be based in a bimetallic active site looking for an enhancement of the overall catalytic properties of the resultant material. However, our interest extends beyond the mere execution of the reaction to encompass the synthesis and evaluation of the catalyst's properties, which play a crucial role in determining the reaction yield.

The initial step involves synthesizing of the support material, CeO_2, with a high specific surface area. This preparatory stage is crucial for ensuring optimal adhesion of metal particles, thereby enhancing catalytic activity. The high surface area of CeO_2 maximizes the catalyst's effectiveness in promoting the desired chemical transformations. After preparing the support, six distinct catalysts were synthesized. This comprehensive approach considers three different compositions and employs two distinct synthesis

methods: incipient wetness impregnation (IWI) and ball milling (BM). The primary aim of catalyst production is to investigate the impact of synthesis methods and to assess the diverse influences of monometallic and bimetallic catalysts on the reaction. The synthesized catalysts exhibit various compositions, including:

- 10% by weight of Ni on CeO_2 support via IWI synthesis.
- 10% by weight of Ni on CeO_2 support via BM synthesis.
- 9% by weight of Ni and 1% by weight of Fe on CeO_2 support via IWI and BM synthesis, resulting in a $^{Ni}/_{Fe}$ atomic ratio of 8.56.
- 8% by weight of Ni and 2% by weight of Fe on CeO_2 support via IWI and BM synthesis, resulting in a $^{Ni}/_{Fe}$ atomic ratio of 3.81.

Furthermore, a comprehensive characterization study of the catalysts is conducted, encompassing pre- and post-reaction analyses. This examination aims to elucidate any chemical and physical alterations induced by the catalytic process. Techniques such as scanning electron microscopy (SEM), Raman spectroscopy and X-ray photoelectron spectroscopy (XPS) are employed to provide detailed insights into catalyst behavior and performance.

Furthermore, this study thoroughly investigates the reaction behavior under varying temperature conditions, ranging from 550 to 950 °C. This temperature range is strategically chosen to explore the progression of the endothermic reaction across a spectrum of operating parameters. By subjecting the reaction to different temperatures, the research aims to discern how the catalysts respond regarding stability, selectivity, and activity under diverse thermal environments. This comprehensive approach allows for a nuanced understanding of the interplay between temperature and catalytic performance, shedding light on crucial factors influencing the efficiency and effectiveness of the dry reforming process.

Through this multifaceted investigation, the goal is to not only analyze the influence of temperature on reaction yield but also to assess the distinctive effects of monometallic and bimetallic catalysts. By systematically exploring these factors, this study seeks to enhance our understanding of catalytic processes and pave the way for advancements in sustainable energy production.

2. Heterogeneous Catalysis

The term catalysis was initially introduced by the Swedish chemist Berzelius in 1835 (Berzelius, 1836). However, it was not until many years later, in 1894, that Ostwald provided a concise definition, stating that catalysis involves 'the acceleration of a slow chemical process due to the presence of a foreign substance' (Roduner, n.d.). The study of catalysis has since become crucial in overcoming the limitations of slow reaction kinetics, which can prevent thermodynamically favored reactions from reaching equilibrium. Investigating reaction kinetics and the potential use of specialized catalytic systems is essential for enhancing reaction efficiency. Catalysis facilitates alternative reaction pathways with lower activation energies, thereby increasing reaction rates and overall process efficiency.

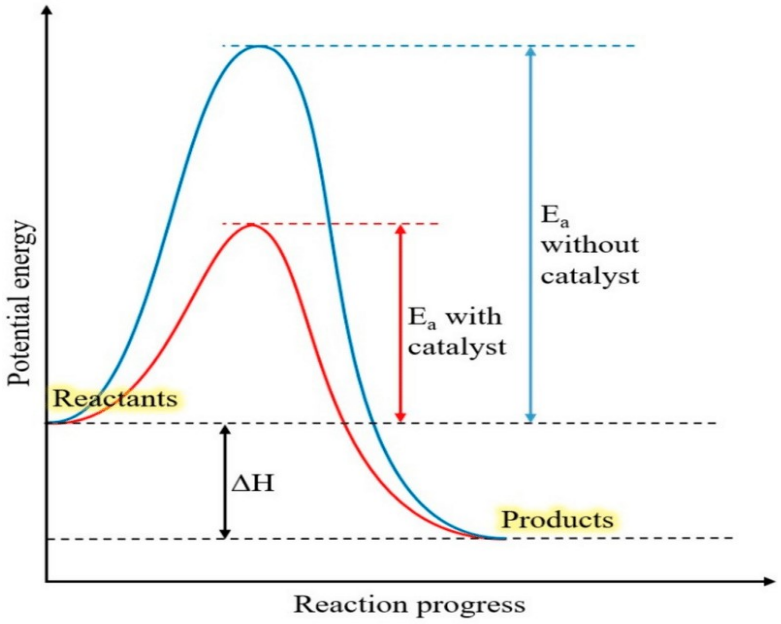

***Figure 4**: The activation energy of reaction with and without catalyst* (Sinar Mashuri et al., 2020).

Catalysts are broadly classified into two categories: homogeneous and heterogeneous. Homogeneous catalysts exist in the same phase as the reactants, while heterogeneous catalysts are in a different phase,

such as solid-liquid or solid-gas systems. The dry reforming of methane (DRM) reaction, discussed in detail in Chapter 3, employs a heterogeneous catalyst.

Each catalyst is defined by three fundamental properties:

- The *Intrinsic Activity*: This defines the catalyst's overall influence on the reaction rate and is primarily governed by the chemical composition and structural configuration of the active sites on its surface.
- The S*electivity*: This property determines the distribution of reaction products, allowing for the optimization of desired outcomes and minimizing byproducts.
- The *Stability*: This describes the catalyst's ability to maintain activity and selectivity over time, minimizing deactivation processes.

In industrial applications, heterogeneous catalysts are often preferred over homogeneous ones due to their ease of handling, separation from reaction mixtures, recovery, and reuse. Solid catalysts offer additional advantages, including good stability, low toxicity, and the ability to resolve compatibility issues related to solubility and functionality. However, designing catalysts with well-defined structural and electronic characteristics is more challenging for solids than for discrete molecules. The need for high selectivity in catalytic processes to optimize feedstock consumption, eliminate separation steps, and minimize byproducts has become increasingly important. Achieving the same level of selectivity with heterogeneous catalysts as with homogeneous ones remains a significant goal in catalysis research (Cesário et al., 2022).

Catalysis has become a powerful tool for controlling water and air pollutants and plays a vital role in many industrial processes. It is estimated that 85%–90% of all products manufactured in the chemical industry involve catalytic processes (Cesário et al., 2022). The increasing demand for faster and more efficient processes underscores the importance of choosing the right catalytic material for optimal performance. Catalysts influence reaction rates and directions, along with other factors such as temperature, pressure, and contact time.

The operation of a heterogeneous catalyst can be described by the following cycle:

1. Diffusion of Reactants: Reactants diffuse to the catalyst's surface.
2. Adsorption: Reactants adsorb onto the catalytic sites, which are specific locations on the catalyst surface where the reaction occurs.
3. Chemical Reaction: Adsorbed reactant molecules undergo a chemical reaction.
4. Desorption: Reaction products desorb from the catalytic sites.
5. Regeneration: The catalytic site is regenerated for a new catalytic cycle.

Throughout this cycle, the catalyst is not consumed but assists in binding and breaking reactant molecules, facilitating the formation and release of products, and regenerating the active site for continuous use (Cesário et al., 2022).

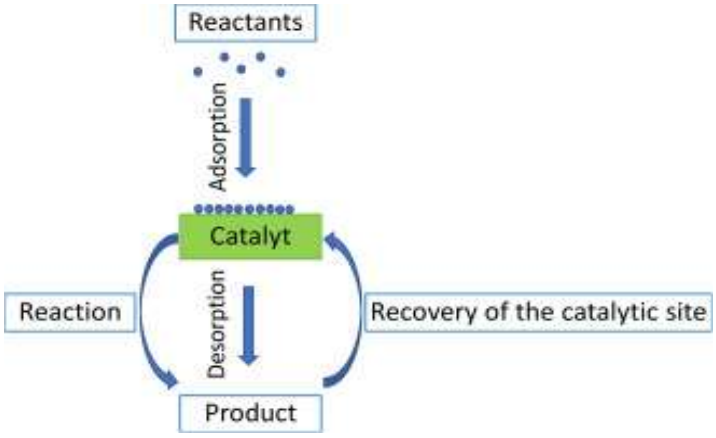

***Figure 5**: Elementary steps of the heterogeneous catalytic reaction (Cesário et al., 2022).*

2.1 Catalyst Deactivation Mechanisms

In the realm of industrial catalytic processes, the longevity of a catalyst emerges as a pivotal economic consideration, underscored by the substantial costs associated with shutdowns, catalyst replacements, and the appropriate disposal of spent materials. The catalyst is conventionally defined as a substance that increases the rate of a chemical reaction without undergoing any permanent chemical alteration itself. However, catalytic materials can undergo chemical, physical, and mechanical modifications that may affect their performance over time (Cimino & Lisi, 2019). Various phenomena can lead to catalyst deactivation, characterized by a loss of activity or selectivity over time. The following briefly outlines the main deactivation processes to be considered (Martín et al., 2022).

I. *Fouling, coking and carbon deposition*. Fouling presents a formidable challenge in industrial catalytic processes, marked by the deposition of fluid-phase species onto the catalyst surface. This physical or mechanical deposition can obstruct active sites and pores, culminating in a discernible decline in catalytic performance. As fouling progresses, catalyst particles may disintegrate, and reactor voids can become obstructed, posing significant operational hurdles. The terms 'carbon' and 'coke' are commonly used in this context, albeit somewhat arbitrarily defined based on their origins. Carbon typically results from CO disproportionation, while coke is formed through the decomposition or condensation of hydrocarbons on catalyst surfaces, often comprising polymerized heavy hydrocarbons. However, coke forms vary widely, ranging from high molecular weight hydrocarbons to primarily carbonaceous substances like graphite,

influenced by various formation and aging conditions (Bartholomew, 2001). Catalytic reactions accompanied by carbon or coke formation can broadly be classified as coke-sensitive or coke-insensitive. In coke-sensitive reactions, inert coke deposits on active sites lead to decreased activity. In contrast, in coke-insensitive reactions, relatively reactive coke precursors formed on active sites are easily removed by hydrogen (or other gasifying agents). The rapid formation of a carbon encapsulating layer around the active surface can physically limit the diffusion of gaseous molecules, resulting in a swift loss of activity. Carbon can also diffuse within metal particles, forming metal carbide species and precursors for carbon nanofiber formation, which can mechanically compromise the catalytic material's structure.

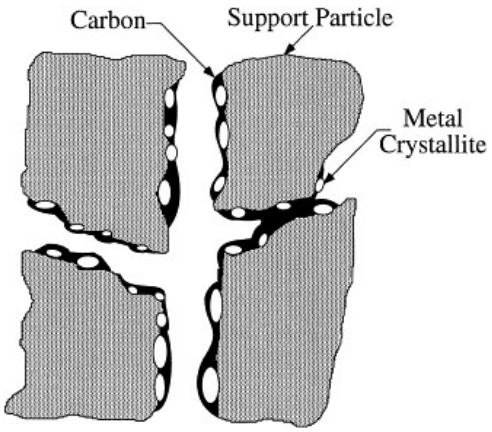

***Figure 6**: Fouling, Crystallite Encapsulation, and Pore Plugging of a Supported Metal Catalyst due to Carbon Deposition (Bartholomew, 2001).*

II. *Sintering*, a thermal phenomenon, involves the gradual fusion and aggregation of initially dispersed metal nanoparticles into larger entities, thereby reducing their surface area-to-volume ratio. This process loosens their interaction with the support and leads to an increase in particle size. Smaller nanoparticles, which typically exhibit higher catalytic activity due to a higher concentration of exposed surface atoms, may lose some of their highly active sites due to sintering, as the reduction in surface area limits the availability of these sites. The Tamman temperature, approximately half of the melting point for a given metal, serves as a pivotal threshold where surface atoms gain sufficient thermal energy to undergo free movement, initiating the diffusion-driven sintering process. In heterogeneous catalysis, where the active phase is often engineered at the nanoscale, smaller nanoparticles have a lower effective melting temperature than bulk materials, making them more susceptible to migration and coalescence. Elevated operating temperatures exacerbate sintering kinetics, as increased thermal energy facilitates the migration of metallic species, enabling them to overcome diffusion barriers more readily. In addition, the catalytic environment plays a crucial role in modulating sintering rates; environments rich in water and oxygen typically accelerate sintering, while hydrogen-rich

environments tend to mitigate the phenomenon by minimizing surface oxidation and promoting surface reconstruction. The strength of the interaction between the metal nanoparticles and the support material profoundly influences sintering dynamics. A robust interaction, characterized by strong metal-support interactions, anchors and stabilizes the active phase, thereby impeding particle migration and aggregation (Cimino & Lisi, 2019).

III. *Poisoning* occurs when specific molecules from reactants or byproducts chemically bind to catalytic sites, rendering them inactive. The degree to which a substance acts as a poison depends on the strength of its adsorption relative to other species competing for catalytic sites. In addition to physically blocking sites, adsorbed poisons can induce changes in the surface's electronic or geometric structure, further diminishing catalytic activity. While some poisoning effects are reversible, like physical blockages, many are irreversible, like sulfur chemisorption on metals. Sulphur, a notable poison for heterogeneous catalysts, forms stable compounds with transition metals even at low concentrations, significantly reducing catalytic activity. Promoters can be added to mitigate poisoning effects by altering surface properties, thereby hindering poison adsorption and preserving catalytic function. These promoters, often metal oxides or compounds, interact with the catalyst surface to enhance its resistance to poisoning. Their addition can also modify the surface chemistry, making sites less susceptible to poison adsorption or facilitating the removal of adsorbed poisons during regeneration processes.

3. Dry Reforming Reaction of Methane

Industrial activities emit significant amounts of carbon dioxide, a major greenhouse gas contributing to climate change. Although CO_2 is non-toxic to humans, excessive CO_2 emissions have adversely affected ecosystems, weather patterns, and sea levels. On the other hand, methane, primarily sourced from livestock farming, landfills, and fossil fuel extraction, possesses potent greenhouse properties, trapping heat in the atmosphere up to about twenty-five times more than CO_2 over 100 years. Despite their environmental impact, these pollutants offer potential as valuable resources when utilized efficiently. In particular, CO_2 can be used in the dry reforming process, which allows for the synthesis of syngas, a mixture of hydrogen and carbon monoxide. This process holds promise for addressing environmental concerns while producing valuable energy resources.

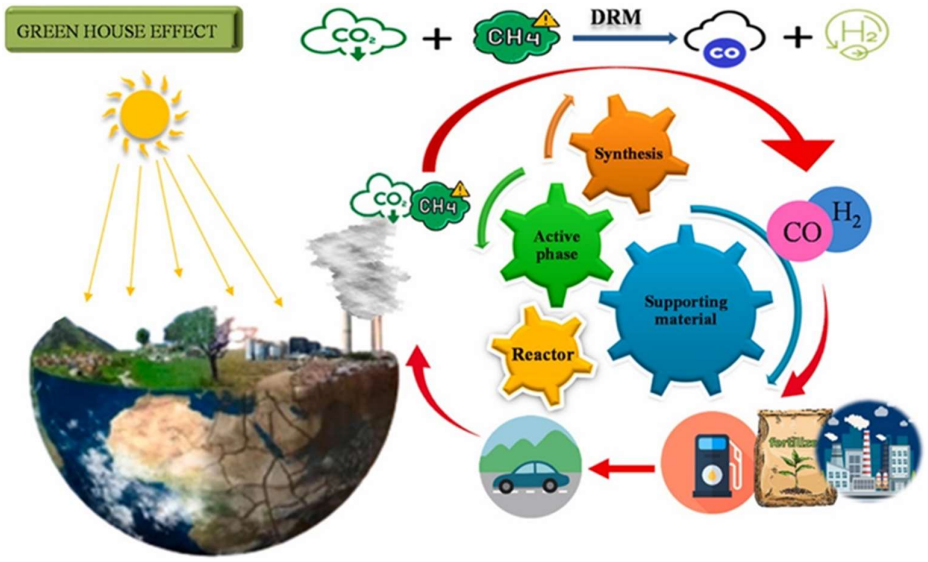

***Figure 7**: General representation of dry reforming reaction of methane (DRM)* (Alhassan et al., 2023).

The Dry Reforming response was first studied by Franz Fischer and Hans Tropsch in 1928 (Fischer & Tropsch, 1928). Their interest was sparked by scarcity of raw materials for liquid fuel production in Western Europe during the period of the two world wars. Since then, researchers have dedicated significant efforts to refining and leveraging this process. It is only in recent times, however, that syngas production through dry reforming of hydrocarbons using heterogeneous catalysts has garnered

widespread interest. This surge in attention is evident from the escalating number of publications, as illustrated in Figure 8.

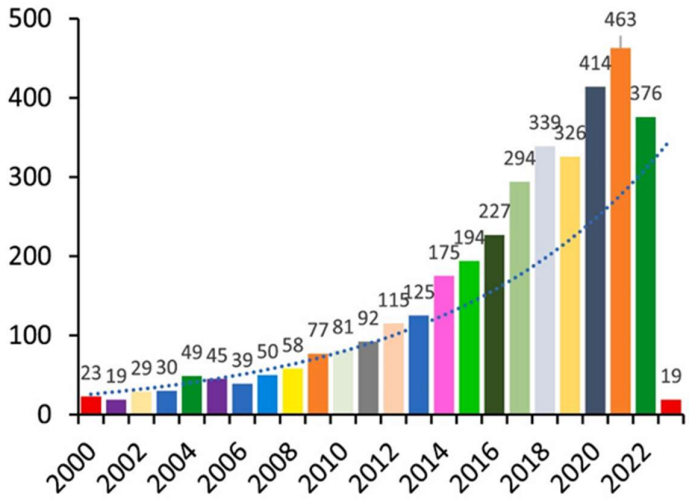

***Figure 8**: The annual number of DRM-related publications on 'Web of Science" between 2000 and 2022, filtered by the term "Dry Reforming of Methane" (Alhassan et al., 2023).*

3.1 Thermodynamics of Reaction

In a chemical process, the conversion of reactants into products is governed by the equilibrium dynamics and reaction kinetics. To understand the evolution of the reaction and predict the composition of the outlet stream, a thorough investigation into reaction thermodynamics is imperative. This study offers crucial insights into product behavior and equilibrium dynamics. Furthermore, it provides the opportunity to assess the optimal reaction conditions to maximize yields and minimize the synthesis of secondary or undesired reactions. The following equation describes the reaction of Dry Reforming of Methane (DRM):

$$CH_4 + CO_2 \leftrightarrow 2H_2 + 2CO \qquad (\Delta rH°=247.3 kJ/mol) \qquad (8)$$

This reaction not only ensures the reduction of overall emissions and the production of syngas but also serves as the starting point for methanol and ammonia synthesis, as well as for Fischer-Tropsch reactions (Minardi et al., 2015). The reaction is strongly endothermic and reversible and involves an increase in the number of moles, making it favorable at high temperatures and low pressures. CO_2 acts as the oxidizing agent in the DRM, constituting a highly stable molecule, thus rendering the process more energy-demanding than steam and autothermal reforming. The latter employs steam and oxygen as the oxidizing agents, respectively.

In addition to the main reaction (8), the presence of secondary reactions, which become competitive depending on the various operating conditions, must be considered.

Reverse water-gas-shift (RWGS) $CO_2 + H_2 \leftrightarrow CO + H_2O$ ($\Delta rH° = 41$ kJ/mol) (9)

Hydrogenation of CO_2 $CO_2 + 2H_2 \leftrightarrow C + 2H_2O$ ($\Delta rH° = -90$ kJ/mol) (10)

Hydrogenation of CO $H_2 + CO \leftrightarrow H_2O + C$ ($\Delta rH° = -131$ kJ/mol) (11)

In addition to these reactions, it is important to consider the secondary reactions of CO disproportionation (4) and methane decomposition (5), as previously discussed in Section 1.2.3. These reactions can lead to the formation of coke, which is a significant concern in the synthesis process.

The graphical depiction of the process's thermodynamics aids in understanding how these reactions impact the composition of the effluent stream.

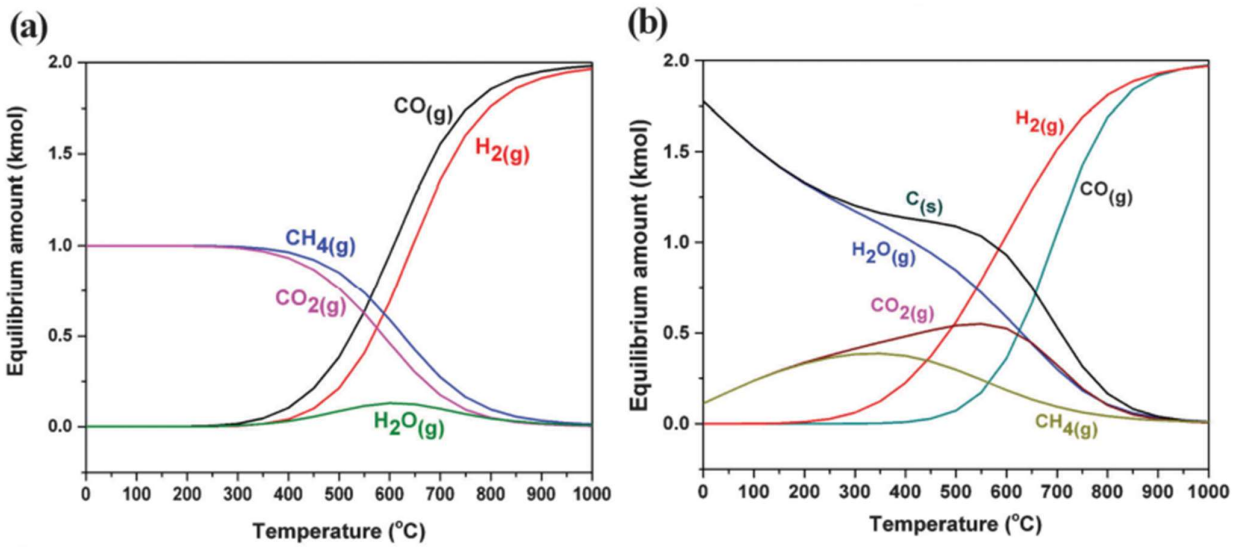

***Figure 9**: Thermodynamic equilibrium plots for DRM at 1 atm, from 0–1000 °C and at inlet feed ratio of CO2/CH4 = 1. (a) Assuming no carbon formation occurs, (b) assuming carbon formation occurs (Pakhare & Spivey, 2014).*

As depicted in Figure 9, within the temperature range of 400 to 800°C and with elevated CO_2 concentrations in the feed, the secondary reaction of reverse water gas shift becomes competitive. This results in the synthesis of water and a reduction in the H_2/CO ratio obtained through reforming. The Boudard reaction (4) and the reduction of CO and CO_2 (10,11) occur spontaneously at low temperatures, while methane decomposition (5) takes place at high temperatures. Thermodynamic analysis shows that coke formation in the DRM process is inevitable at standard operating temperatures; however, temperatures above 900°C can prevent it. Therefore, the choice of catalyst utilized assumes significant relevance, in order to introduce the role of reaction kinetics to boost selectivity towards syngas production and minimize coke formation.

Including a catalyst within the reaction scheme becomes essential to optimize reaction efficiency, particularly as it addresses challenges arising from high temperature demands. However, secondary reactions lead to the synthesis of carbon, which deposits on the catalyst surface. This phenomenon, known as carbon deposition or coking, gradually diminishes the catalyst's activity over time, posing a significant challenge in sustaining long-term catalytic performance. As the carbon layer builds up, it creates physical barriers obstructing reactant molecules' access to the active sites on the catalyst surface, thereby impeding the desired chemical transformations. Consequently, maintaining catalyst stability and activity necessitates the development of strategies to mitigate carbon deposition, such as employing catalyst formulations with improved resistance to coking or implementing periodic regeneration procedures to remove accumulated carbonaceous species. By addressing these issues, catalyst performance can be enhanced, enabling prolonged operation and improved overall process efficiency. Additionally, carbon formation contributes to operational challenges, such as the formation of hot spots and the blockage of the entire catalytic bed, further hindering the overall production process.

3.2 Catalyst System of Reaction

The remarkable stability and chemical inertness of CO_2 and CH_4, characterized by Gibbs free energies of approximately -394 kJ/mol and -50.7 kJ/mol, respectively, present significant challenges to their activation. Overcoming this hurdle requires substantial energy input and the utilization of highly active metallic catalysts (Alhassan et al., 2023). These catalysts are instrumental in reducing the activation energy required for the reaction while concurrently enhancing selectivity towards H_2 and CO. It is essential to note that modifying the components, promoters, and even the preparation method of catalysts can lead to completely different behaviors.

Diverse metals, including Ruthenium (Ru), Rhodium (Rh), Platinum (Pt), Iridium (Ir), Nickel (Ni), and Cobalt (Co), have been identified as active catalysts for dry reforming. These metals are typically supported on various substrates such as Zirconia (ZrO_2), Cerium dioxide (CeO_2), Alumina (Al_2O_3), and Silica (SiO_2). Non-noble metals like Nickel (Ni), Cobalt (Co), and Iron (Fe) are commonly favoured in industrial dry reforming due to their cost-effectiveness, widespread availability, and catalytic efficiency. However, despite their advantages, these metals often encounter challenges related to catalyst deactivation, primarily due to coke formation, which adversely affects operational efficiency. In contrast, noble metal catalysts offer superior resistance to coke deposition, increased stability, and enhanced catalytic activity. Nevertheless, their extensive use in industries is constrained by their high cost and limited availability (Aziz et al., 2019). The different performances of noble and non-noble metals in reactions involving gaseous carbon can be attributed to differences in the solubility and diffusivity of solid carbon solutions within the lattice structure of metals. Specifically, carbon exhibits

higher diffusivity in non-noble metals, potentially leading to its accumulation and subsequent interference with catalytic capabilities through the synthesis of species, which alter the initial properties (YANG, 1990).

The catalysts employed to achieve the DRM are considered bifunctional, necessitating the presence of suitable supports capable of multifaceted functions. This characteristic arises from the reaction's dual activation requirement of methane and carbon dioxide. While methane typically undergoes activation on metallic surfaces, carbon dioxide requires activation on either basic or acidic supports. These supports, often metallic oxides, are pivotal in optimizing the catalyst's efficiency. They not only facilitate the efficient dispersion of the active phase but also impart enhanced mechanical robustness and a larger surface area for optimal adhesion. Furthermore, these supports actively interact with the reaction reagents regardless of their acidity or basicity. Acidic supports facilitate reactant activation by forming formates and hydroxyls, whereas basic supports facilitate activation via the formation of oxycarbonates (Pakhare & Spivey, 2014).

Moreover, incorporating a promoter within the overall structure of the catalytic system can be considered. This component aims to enhance the catalyst's activity in the dry reforming of methane reaction and promote the dispersion of the active metal, resulting in increased methane activation compared to unpromoted catalysts. Examples of promoters include V_2O_5, Zn, and Sn (Pakhare & Spivey, 2014).

3.2.1 Reaction Mechanism of DRM

Despite extensive research efforts and many studies, a conclusive research work elucidating the DRM mechanism still needs to be discovered. This can be attributed to the diverse operational conditions and the substantial impact of catalyst characteristics on reaction outcomes. In fact, two general classes of proposed mechanisms of DRM exist to date: the monofunctional and bifunctional mechanisms. The monofunctional mechanism involves the activation of both CO_2 and CH_4 on metal sites, while the bifunctional mechanism follows a different route, with CH_4 being activated on metallic surfaces and CO_2 on the support (Aramouni et al., 2018a).

It is interesting to study the implications of the DRM process's bifunctional nature by analyzing the activation of the reaction reagents on the two different available sites, as illustrated in Figure 10. Furthermore, the transfer of reactive intermediates between active sites will be explored to elucidate the role of catalyst structure in DRM catalysis (Aziz et al., 2019).

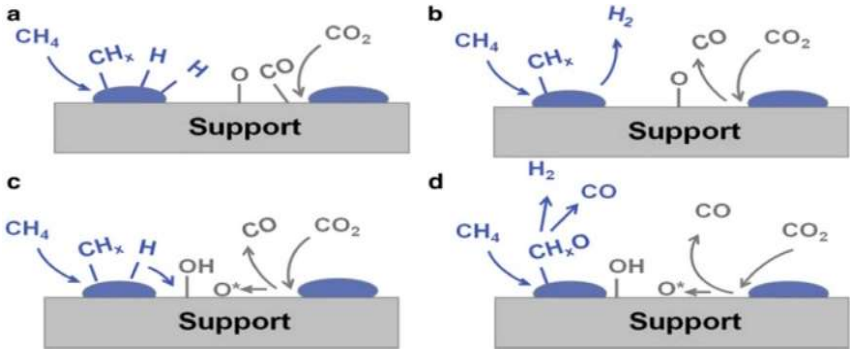

***Figure 10**: Reaction mechanism for the dry reforming of methane (Aziz et al., 2019).*

- *CH_4 activation on metal sites*

$$CH_{4\,(gas)} \leftrightarrow CH_{x\,(metal)} + (4-x)H_{(metal)} \quad (12)$$

$$2H_{(metal)} \leftrightarrow H_{2(gas)} \quad (13)$$

$$OH_{(support)} \leftrightarrow OH_{(metal)} \quad (14)$$

$$OH_{(metal)} \leftrightarrow O_{(metal)} + H_{(metal)} \quad (15)$$

$$H_{(metal)} + OH_{(metal)} \leftrightarrow H_2O_{(gas)} \quad (16)$$

$$O_{(metal)} + CH_{x(metal)} \leftrightarrow CO_{(metal)} + xH_{(metal)} \quad (17)$$

$$CO_{(metal)} \leftrightarrow CO_{(gas)} \quad (18)$$

CH_4 is adsorbed and dissociated on the active surface of the metal to produce hydrogen and hydrocarbons (CH_x) (12). The energy required to break CH_x-H bonds varies depending on the surface characteristics. The hydroxyl groups on the support sites can migrate towards nearby metal sites (14), ultimately undergoing dissociation to form adsorbed oxygen and hydrogen (15). Subsequently, the dissociated oxygen species react with intermediate CH_x species at the metal-support interfaces (17). This reaction leads to the formation of products like H_2 and CO (13,18). The temperature of the reaction significantly influences various reaction steps, including the quantity of adsorbed hydrogen on metal sites, the mobility of oxygen species, and the desorption of CO from the catalyst surface. However, the dissociation of methane on the catalyst is the step that predominantly governs the reaction rate or represents the stage that limits the reaction kinetics. Each partially dissociated CH_x species tends to adsorb onto a site that satisfies its need for a complete valency structure; for instance, CH_3 species favor adsorption onto individual metal atoms, whereas CH_2 species preferentially bridge two adjacent metal atoms. It is crucial to highlight that step sites exhibit an amplified capability to facilitate the adsorption and dissociation of methane compared to their flat-surface counterparts (Aziz et al., 2019) .

- *CO_2 activation on support sites*

$$CO_{2\,(gas)} \leftrightarrow CO_{2\,(support)} \quad (19)$$

$$CO_{2\,(support)} + O^{2-}_{(support)} \leftrightarrow CO^{2-}_{3\,(support)} + O_{(metal)} \quad (20)$$

$$CO_{2\,(support)} + OH^{-}_{(support)} \leftrightarrow HCO^{-}_{3\,(support)} \quad (21)$$

$$H_{(metal)} \leftrightarrow H_{(support)} \quad (22)$$

$$CO^{2-}_{3\,(support)} + 2H_{(support)} \leftrightarrow HCO^{-}_{2\,(support)} + OH^{-}_{(support)} \quad (23)$$

$$HCO^{-}_{3\,(support)} + 2H_{(support)} \leftrightarrow HCO^{-}_{2\,(support)} + H_2O_{(support)} \quad (24)$$

$$HCO^{-}_{2(support)} \leftrightarrow CO_{(support)} + OH^{-}_{(support)} \quad (25)$$

$$CO_{(support)} \leftrightarrow CO_{(gas)} \quad (26)$$

$$2OH^{-}_{(support)} \leftrightarrow O^{2-}_{(support)} + H_2O_{(support)} \quad (27)$$

$$H_2O_{(support)} \leftrightarrow H_2O_{(gas)} \quad (28)$$

The oxygen atom of CO_2 chemically interacts with the surface through the metal cation (19), thus establishing the surface as a Lewis acid. Meanwhile, the carbon atom of CO_2 interacts via an O_2^- site, typically a defect site of the support material, which acts as a Lewis base. This interaction leads to the formation of three common forms of CO_2: carbonate ion (CO_3^{2-}) through reaction with the O site (20), bicarbonate ion (HCO_3^-) through reaction with surface OH groups (22) and formate ion (HCO_2^-) (23,24) (Aziz et al., 2019).

3.3 Cerium Oxide as a support material

In heterogeneous catalysis, cerium oxide emerges as an exceptional choice among the available materials due to its unique properties. CeO_2 rare-earth oxides dominate technological catalyst applications for several reasons, including their eco-friendliness, presence of surface-bound defects, outstanding redox capabilities, and remarkable capacity for oxygen storage and release.

Cerium oxide not only serves as a catalyst but also excels as a support for catalytic components thanks to its ability to store, release, and exchange oxygen within its cubic fluorite structure. The rapid redox kinetics of ceria facilitate high oxygen exchange rates, contributing to its oxygen storage capacity

(OSC). Furthermore, cerium's two stable oxidation states enable diverse applications, particularly those involving the redox chemistry of the Ce(IV)/Ce(III) couple (Manan et al., 2022a). Additionally, the reducibility of cerium oxide's surface is crucial for its interaction with metal nanoparticles, fostering strong metal-support interactions that enhance catalytic performance and durability.

Ceria's significance as catalyst support was recognized in 1979 when its ability to promote dispersion surpassed that of conventional supports like Al_2O_3 (Manan et al., 2022a). Supports play a critical role in heterogeneous catalysis by providing a high surface area for metal dispersion, resisting sintering, and stabilizing active sites.

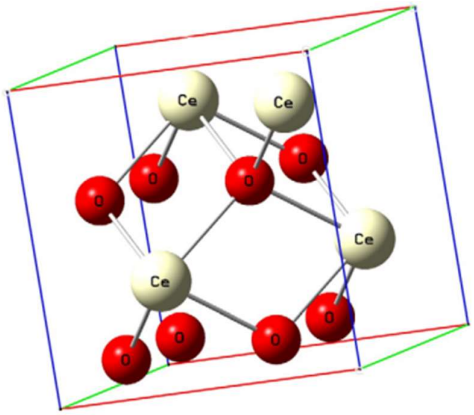

***Figure 11**: The cubic fluorite structure of cerium dioxide* (Bumajdad et al., 2009).

CeO_2 is particularly favored for noble metal catalysts due to its strong metal support, oxygen storage capacity (OSC), reducibility (Ce^{4+}/Ce^{3+}), and resistance to soot. Oxygen vacancies on the CeO_2 surface also facilitate CO_2 dissociation, enhancing reforming activity and carbon deposit removal. However, controlling the size and uniformity of supported metal catalysts remains a significant challenge in catalytic structure-property relations (Manan et al., 2022a).

It is common practice to dope ceria with additional elements to enhance its oxygen storage capacity by inducing lattice defects and reducing the energy barrier for oxygen vacancy formation. Zirconium is frequently employed for this purpose, forming solid solutions with cerium ($Ce_xZr_{1-x}O_{2-y}$). The isovalent Zr^{4+} cation, with its smaller radius compared to Ce^{4+}, introduces lattice strain and distortions that promote the formation of oxygen vacancies. Similarly, other elements such as titanium, lanthanum, gadolinium, praseodymium, samarium, and neodymium are utilized for doping ceria. By incorporating these elements, each with varying radii and valences, into the ceria lattice, the OSC is increased by introducing defects and altering electronic state of cerium (P. Li et al., 2019).

3.3.1 Synthesis of Ceria Support: Conventional Methods

The synthesis techniques employed for nanomaterials play a pivotal role in determining their performance. Various factors contribute to the significant structural and size variations observed in nanomaterials, including the calcination temperature and duration, the choice and concentration of surfactants, as well as the aging time and synthesis temperature. These parameters collectively influence nanomaterials' morphology, size distribution, and properties, enhancing their applicability across diverse fields (Mohd Fadzil et al., 2018). Different methodologies are employed to synthesize ceria nanomaterials. These methods encompass precipitation, co-precipitation, hydrothermal, mechanosynthesis, combustion synthesis, sol-gel, microemulsion and pyrolysis. Among these, precipitation is regarded as the most straightforward technique.

The *precipitation synthesis* method is well-regarded for its simplicity in producing inorganic metal oxides. It involves precipitating metal cations from a solution by introducing specific agents or adjusting the pH, leading to the formation of solid particles. Only three main chemicals are typically required: the cerium precursor, precipitant agent, and surfactant, if necessary. The cerium precursor acts as the source of cerium ions. At the same time, the precipitant agent initiates the precipitation reaction by causing the cerium ions to react and form insoluble cerium hydroxide or another solid cerium compound. The addition of a surfactant may assist in controlling the particle size and morphology during the precipitation process (Mohd Fadzil et al., 2018). One significant advantage of the precipitation method is its minimal reaction time and simple reaction conditions, making it promising for producing monodispersed particles with controlled properties. By adjusting parameters such as the concentration of reactants, reaction temperature, and pH, researchers can fine-tune the synthesis process to achieve desired particle sizes and characteristics. Moreover, the versatility of this method allows for scalability and reproducibility, making it suitable for both laboratory-scale and industrial-scale production. Generally, the synthesis begins preparing an aqueous solution by dissolving a metal precursor in water. The pH of the solution is then adjusted using NH_3 or NaOH solutions until it reaches values of about 9-10. Most of the transition metal cations precipitate as hydroxides at this pH range. This method is also applicable for preparing mixed oxides and doping oxide materials by adding more cations to the solution during co-precipitation synthesis. Figure 12 provides a visual overview of the synthesis of ceria nanoparticles using the precipitation method, illustrating the sequential steps involved in the preparation process.

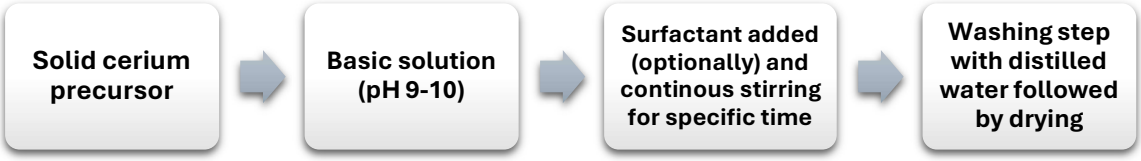

***Figure 12**: Typical steps of precipitation technique for ceria nanoparticles.*

Additionally, modifications to the conventional precipitation technique have been explored to enhance ceria synthesis. For instance, replacing the conventional stirring method with sonication has shown promising results. Sonication modification could yield ceria up to 16% higher than conventional techniques, with a reduced crystallite size of 6nm compared to around 27nm in the conventional approach. However, this modification requires higher energy and may not be as cost-effective as the conventional method (Mohd Fadzil et al., 2018).

Hydrothermal synthesis is another advanced method to prepare inorganic materials with precise control over their properties. This method utilizes different acqueous solutions at high temperature and pressure to create a unique reaction environment that significantly influences the solubility of precursors and products. High-purity, high-crystalline nanomaterials are formed under these conditions, allowing researchers to tailor the properties of the final materials by adjusting parameters such as precursor concentration, solution pH, temperature, pressure, and other variables (Yang et al., 2013).

In this thesis work, the hydrothermal synthesis method was employed to prepare CeO_2 with a higher surface area and better thermal resistance compared to CeO_2 obtained using the previously described precipitation method, which resulted in a lower surface area. Therefore, the supports prepared using the hydrothermal method are identified by the acronym HSA, indicating high surface area.

In addition to hydrothermal synthesis, another advanced method utilized to prepare inorganic materials is *solution combustion synthesis* (SCS). It is known for its simplicity, speed, and cost-effectiveness in producing various nanostructured oxides. During SCS, exothermic reactions occur in an aqueous or sol-gel medium, driven by a redox reaction between a fuel (reducing agent) and metal cations in the presence of oxidizing agents like metal nitrates. This process results in high-purity products with exceptional characteristics, such as large surface areas and narrow particle size distributions, which are crucial for various applications. One advantage of SCS is the rapid generation of gases during combustion, which dissipates heat and prevents premature sintering between particles, leading to a finer product. In contrast to hydrothermal synthesis, which relies on high-temperature and high-pressure water solutions to influence precursor solubility, SCS offers simplicity and cost-effectiveness (Cam et al., 2022).

Expanding our repertoire of synthesis methods, the *sol-gel* approach emerges as a versatile technique for nanostructure fabrication. Unlike high-temperature methods, sol-gel operates at lower temperatures, typically between 70°C and 320°C, allowing for energy-efficient synthesis. The process begins with dissolving a molecular precursor, typically a metal alkoxide, in water or alcohol. This solution undergoes hydrolysis and condensation reactions, leading to the formation of a colloidal suspension called sol. As the sol ages, it undergoes gelation, forming a three-dimensional network known as a gel. The gel is then dried to remove solvent and produce a solid material. This drying process can be tailored to achieve specific properties, such as nanoporosity, which enhances surface area and reactivity. Subsequent calcination transforms the gel into the desired oxide material. Sol-gel synthesis offers several

advantages, including high purity, narrow particle size distribution, and precise control over chemical composition. Its scalability and versatility make it suitable for various applications, from catalyst preparation to optical coatings (Bokov et al., 2021).

3.4 Ni-based catalyst: Enhancing Performance

This chapter introduces different reported strategies for optimizing the performance of nickel-based catalysts for methane dry reforming (DRM) and compares them with the noble metals traditionally used.

In catalysis, noble metals have long been valued for their ability to drive methane dry reforming and resist coke formation. However, their high cost and limited availability have spurred the search for more cost-effective alternatives. Due to their effectiveness and economic feasibility, nickel-based catalysts have emerged as promising candidates. While noble metals excel in breaking the carbon-hydrogen (C-H) bond and preventing carbon deposition, nickel-based catalysts offer a practical solution, given their abundance, economic feasibility, and strong catalytic properties (Manan et al., 2022b).

However, nickel-based catalysts face their challenges. They are prone to sintering and coking at higher temperatures, which can degrade their performance over time. Nonetheless, ongoing research aims to overcome these challenges and improve the effectiveness of nickel-based catalysts in DRM processes.

Several strategies can be employed to reduce carbon formation to optimize the performance of Ni-based methane dry reforming catalysts. One approach involves selecting supports with high oxygen ions mobility, such as ceria-based materials like CeO_2 and CeO_2-ZrO_2 solid solutions. These materials facilitate the reaction with adsorbed carbon species, thereby mitigating carbon accumulation on the catalyst surface. It is important to note that the utilization of ceria-based materials has been previously discussed in Chapter 3.3.

In addition to support selection, surface modification with additives such as potassium or sodium can also effectively suppress carbon formation. These additives impart a basic character to the catalyst surface, which helps reduce carbon deposition. However, it is essential to consider that while these additives may effectively reduce carbon deposition, they might also slightly decrease catalytic activity (Manan et al., 2022b).

Alongside support selection and surface modification, incorporating a second metal into the active phase presents another strategy for improving the performance and stability of Ni-based catalysts for methane dry reforming. Adding a second metal can enhance the catalyst's activity by participating in the reaction or improving the physical properties of the Ni active phase. Noble metals like Pt, Pd, Ru, Rh, and Ir are the most commonly used elements for forming bimetallic Ni-based catalysts. Noble metals promote the reducibility of NiO by activating H_2 at low temperatures and facilitating the diffusion to NiO through

the hydrogen spillover effect. Furthermore, noble metal addition has demonstrated self-activation properties in the presence of just CH_4, without pre-reduction treatment (D. Li et al., 2011). The order of addition of the noble metal also plays a significant role. Sequential impregnation of the noble metal onto the monometallic Ni-based catalyst has generally been the most effective strategy (Morales-Cano et al., 2015). Incorporating a second metal enhances the resistance to sintering of the Ni active phase. For instance, Morales-Cano et al. showed that Ir and Rh could form stable alloys preventing the sintering of Ni, while Ru segregated from the Ni particles and provided less sintering resistance.

Non-noble metals such as Co, Fe, Cu, and Mo have been used to a lesser extent. Despite their low catalytic activity as single elements, bimetallic catalysts have been shown to have positive effects. In particular, Ni-Fe bimetallic catalysts have emerged as an optimal choice due to their ability to enhance the catalyst's activity while minimizing potential deactivation mechanisms. Iron, composing 5% of the earth's crust, is abundant and offers various oxidation states, low toxicity, and a range of electronic properties, making it an ideal functional material (Theofanidis et al., 2019).

This study will investigate and compare the performance of monometallic Ni catalysts with Ni-Fe bimetallic catalysts to evaluate their actual improvement. The increasing interest in nickel-iron alloys among researchers highlights the need for a clearer understanding of their role in mitigating carbon deposition during reforming reactions.

3.5 Catalyst Synthesis

Incorporating the active phase onto the support is a critical stage in heterogeneous catalyst preparation, directly influencing catalytic performance. After examining various support synthesis methods, understanding how adding the active phase influences interactions with the support becomes paramount. These interactions, which govern the distribution of active species, structural stability, and reactivity, are crucial for optimizing catalyst performance. Standard criteria for achieving optimal performance include narrow size distribution and high dispersion on the support. This chapter explores impregnation, ball milling, and deep coating method to understand how they modulate these interactions and catalyst properties. By discussing the advantages, disadvantages, and implications of these methods for catalytic performance, a comprehensive overview of synthesis strategies for designing efficient catalysts is provided.

3.5.1 Impregnation Methods

Impregnation is commonly used to prepare supported metal catalysts, particularly Pt catalysts. There are two main approaches: wet impregnation (WI) and incipient wetness impregnation (IWI). WI involves

using an excess amount of precursor solution, resulting in a thin slurry. On the other hand, IWI limits the solution amount to fill just the pore volume of the support material, ensuring a high degree of dispersion (Hutchings & Védrine, 2004).

The principle of IWI is to match the impregnating solution volume with the pore volume of the support material. This method prevents the impregnated powders from being wetted, as the liquid amount is precisely enough to fill the pores. After saturating the support with the impregnating solution, thermal treatments remove the solvent. This process can be repeated to achieve the desired metal loading. Finally, calcination step is usually performed to anchor the oxidized active phase dispersed on the oxide support material (Hutchings & Védrine, 2004).

IWI results in catalysts characterized by a well-dispersed and homogeneous distribution of active metal nanoparticles. This method efficiently obtains industrially relevant catalysts with precise metal loading and uniform particle size distribution. However, some limitations exist. High metal loadings may require large solvent volumes, posing challenges for materials with low pore volume or metal salt precursors with low solubility. Additionally, particle size obtained through IWI is typically large due to agglomeration and sintering during support drying and calcination steps.

In addition to wet impregnation (WI) and incipient wetness impregnation (IWI), co-impregnation involves simultaneously impregnating two or more metal precursors onto the support material. This method allows for incorporating multiple active metals in a single step, offering potential advantages in catalyst design and performance optimization. (Mehrabadi et al., 2017) .

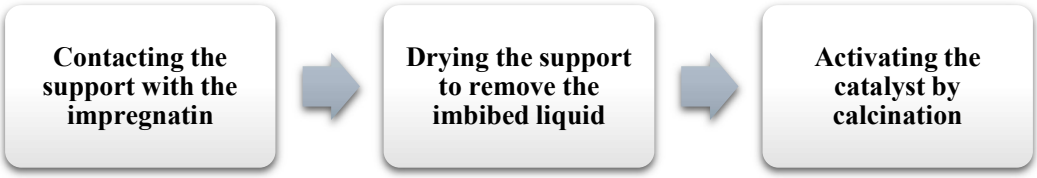

***Figure 13**:Schematic representation of the impregnation method.*

3.5.2 Ball Milling Method: mechanochemistry

In recent years, the chemical industry has witnessed a growing demand for enhanced sustainability, especially concerning the eco-friendly preparation of chemical compounds. While wet chemical methods like incipient wetness impregnation and precipitation synthesis offer simplicity and process control advantages, they also present sustainability challenges. These include the extensive use of water

and solvents, potential pollution from metal precursor release, and the energy-intensive nature of multiple impregnation and drying steps.

Among the methods showing improved sustainability, mechanochemistry has emerged as a promising alternative gaining traction in both academic and industrial research. This ancient form of chemistry employs mechanical forces to induce transformations in materials. When applied to preparing heterogeneous catalysts, mechanochemistry enables solventless synthesis of inorganic materials with tailored properties and precise processing control (Baláž et al., 2013).

Although mechanochemical technologies have yet to be widely utilized at the industrial level for catalyst production, they are extensively employed in other industrial sectors. They offer cost-effective and less sophisticated material processing methods, with promising prospects for scaling mechanochemical synthesis from laboratory to industrial settings (Baláž et al., 2013).

Mechanochemical synthesis presents distinct advantages over traditional methods, such as the ability to produce large quantities of catalysts in shorter timeframes without the need for solvents or prolonged, energy-intensive heating treatments.

Moreover, mechanochemical synthesis presents an opportunity to reduce waste generation by enabling the direct synthesis of catalysts without the need for additional purification steps. The scalability of mechanochemical processes makes them attractive for large-scale industrial applications, potentially leading to significant cost savings compared to traditional wet chemical methods.

Mechanochemical methods are categorized into three types based on the milling device used: attritor mills, planetary mills, and ball mills (Baláž et al., 2013).

- Attritor mills: This device involves a rotating arm inside a tank filled with balls and powders.
- Planetary mills: In this setup, a jar filled with balls and powders rotates around its axis and the center of the mill, similar to a planet's motion.
- Ball mills: This method involves shaking a jar filled with balls and powders in a specific direction.

These methods differ primarily in the energy delivered to the samples and the volume of powder they can process. Planetary mills typically achieve the highest milling intensities and can handle larger volumes of powder, whereas ball mills are smaller and provide less energetic impacts.

As research in mechanochemistry advances, further optimization and exploration of its potential are expected, ultimately leading to broader adoption in the chemical industry for sustainable catalyst synthesis.

Key parameters directly controlled in ball milling include milling frequency, duration, and ball-to-powder mass ratio (BPR). Other factors influencing mechanochemical synthesis include precursor

nature, the use of small amounts of liquids or solvents (wet ball milling), and ball size and quantity, which affect the kinetic energy exchanged during milling impacts and the milling atmosphere. The final calcination step is crucial to ensure proper adhesion to the support, stabilizing the active phase dispersed on the support material and enhancing its overall performance and durability (Thambiliyagodage & Wijesekera, 2022).

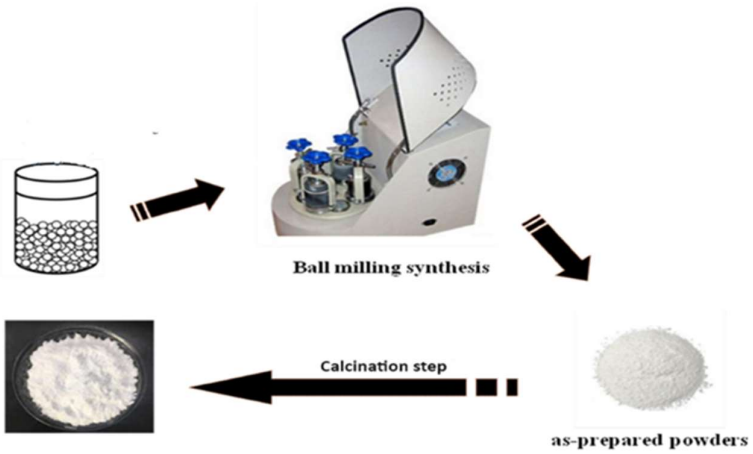

***Figure 14**: Schematic representation of the high-energy ball milling synthesis mechanism* (Aramouni et al., 2018b).

3.5.3 Other Methods

In the *deposition precipitation* (DP) method, highly soluble metal salt precursors are converted into less soluble substances, leading to exclusive precipitations on the support surface. This transformation is achieved by manipulating solution parameters such as pH, adding precipitation agents, introducing reducing agents, or adjusting complexation agent concentrations. Key requirements for successful precipitation solely on the support include establishing a strong interaction between the soluble metal precursor and the support surface and carefully controlling precursor concentrations in the solution to avoid spontaneous precipitations. Maintaining the metal salt concentration within the solubility and supersolubility thresholds is crucial to prevent precipitations in the liquid phase. The practical application of this method involves immersing the support in a solution containing the soluble precursor. However, despite its effectiveness, the DP method faces challenges in achieving precise control over metal distribution and surface composition, making the preparation of accurately defined bimetallic catalysts particularly difficult (Mehrabadi et al., 2017).

In addition to the other methods examined, *colloidal syntheses* offer another approach for catalyst preparation, providing a three-dimensional method involving several steps. Colloidal syntheses involve the preparation of catalyst precursors in a solvent with a protective agent, deposition of colloids onto the support, and reduction of the mixture chemically. These syntheses can offer tiny particle sizes, but using surfactant and protective agents requires the catalyst to be washed in an appropriate solvent several times

or heated to high temperatures in an inert environment to remove these compounds. Before this step, the catalyst needs to be adsorbed into the support to prevent the agglomeration of metal nanoparticles. Therefore, finding alternative routes to create small nanoparticles without protecting agents is desirable to decrease the difficulty level and avoid contamination (Mehrabadi et al., 2017).

3.6 Catalyst Characterization Methods: A Theoretical Perspective

The performance of heterogeneous catalysts is intricately linked to the properties of the materials involved, with a clear correlation existing between their synthesis, structure, and activity. Consequently, characterizing catalytic materials becomes essential to understanding and establishing the relationship between their catalytic behavior and structural attributes.

One of the most notable advancements in catalysis, particularly in recent decades, is the significant development of characterization techniques. This evolution can be attributed to several key factors:

- *Demand for Enhanced Control*: There is a growing necessity for precise control over catalyst properties to optimize existing processes and develop new ones. This requirement necessitates a comprehensive understanding of catalyst characteristics and their dynamic behaviour.
- *Emergence of Novel Solid Classes*: The introduction of new classes of solids with distinct catalytic properties and characteristics—such as zeolites, oxides with controlled porosity, high-porosity silica, and superacids—has spurred the development of advanced characterization techniques.
- *Technological Innovations*: Technological progress and advancements in computing have led to more powerful and user-friendly versions of existing techniques, including Fourier-transform infrared spectroscopy (FT-IR), Fourier-transform Raman spectroscopy (FT-Raman), and calorimetry. Furthermore, novel techniques initially developed for other industries have been repurposed for catalysis research, such as X-ray photoelectron spectroscopy (XPS), extended X-ray absorption fine structure spectroscopy (EXAFS) employing synchrotron light sources, secondary ion mass spectrometry (SIMS), ion scattering spectroscopy (ISS), and electron probe microanalysis (EPMA), among others.

In this section of the thesis, we will provide a theoretical overview of the characterization techniques employed to describe catalysts. By comprehensively understanding these techniques, we can appreciate their utility in elucidating catalyst materials' structural properties and behavior (Leofanti et al., 1997).

3.6.1 Raman Spectroscopy

Raman spectroscopy emerges as a powerful tool in the characterization of heterogeneous catalysts, beneficial for assessing the composition and structure of as-prepared materials and identifying the presence of carbonaceous species in spent catalysts. This analytical method revolves around illuminating the sample surface with a laser and detecting the scattered light resulting from the interaction between the laser light and the vibrational modes of the sample. Despite its effectiveness, it is important to note that Raman scattering is a relatively weak phenomenon, with the intensity of the scattered light typically being about 10^6 times lower than that of the incident light (Hess, 2013).

Like infrared spectroscopy, Raman spectra are recorded in Raman shifts, typically measured in cm^{-1}. The vibrational modes of the sample are characterized by their oscillation frequencies, as described by the equation (29).

$$\omega = \sqrt{\frac{k}{u}} \tag{29}$$

Here, k represents the strength of the bond associated with the vibrational mode, while μ denotes the reduced mass of the atoms involved in the oscillation. Vibrational modes for oxide materials generally exhibit frequencies below 1000 cm^{-1} due to the substantial mass of the atoms, whereas carbonaceous species are typically observed in the range of 1200 to 1600 cm^{-1} (Prochazka, 2016).

In addition to elucidating the composition and structure of catalyst materials, Raman spectroscopy offers valuable insights into the dynamic behavior of catalysts during catalytic reactions. By monitoring changes in Raman spectra under reaction conditions, researchers can better understand catalyst activation, surface restructuring, and intermediate species formation, contributing to the development of more efficient and selective catalytic processes. Moreover, advancements in Raman instrumentation enable real-time monitoring of catalytic reactions, providing invaluable information for catalyst design and optimization.

Throughout this thesis, Raman spectroscopy was employed to analyze CeO_2-based catalysts, facilitating the examination of their initial states and providing qualitative insights into carbonaceous species. The instrumentation for these analyses consisted of a Renishaw IN-VIA microRaman system equipped with a green 532 nm laser operating at 1 mW power on the sample. Measurements were typically conducted using 20x and 50x objectives, with multiple spectra collected for each sample. The Airy disk diameter, serving as an estimate for the sampling size of a Raman microscope, was approximately 1.6 μm for the 20x objective (0.4 NA) and 0.87 μm for the 50x objective (0.75 NA). Prior to each measurement, meticulous attention was given to optimizing the laser focusing distance for each point to maximize the signal-to-noise ratio.

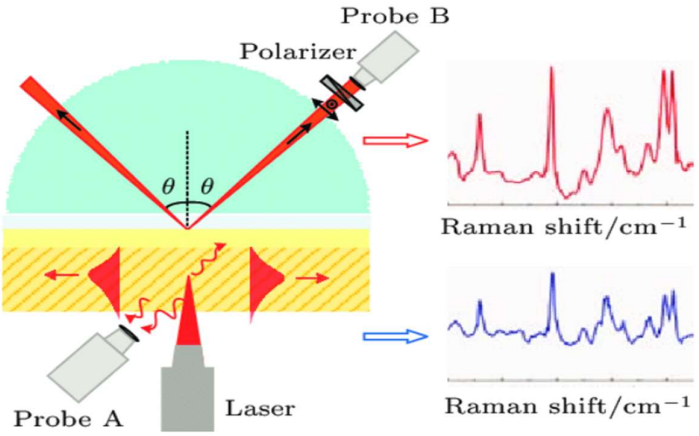

***Figure 15**: Schematic diagram of the Raman spectroscopy setup* (Wan Xiu-Mei et al., 2016).

3.6.2 X-ray Photoemission Spectroscopy (XPS)

X-ray Photoemission Spectroscopy (XPS) is a crucial technique for the characterization of heterogeneous catalysts. Widely used in surface science, XPS provides detailed information about the elemental composition, chemical state, and electronic state of the elements present on a material's surface. Its surface sensitivity makes it especially valuable for studying catalysts, as their facilitated reactions often occur at their surfaces (Stevie & Donley, 2020a).

XPS is based on the photoelectric effect, which involves the emission of electrons from a material when irradiated with X-rays of specific energy. By analyzing the kinetic energy and number of these emitted electrons, researchers can determine the electrons' binding energies within the sample's atoms. This approach allows for the identification of elements and the determination of their chemical states and concentrations. The binding energy of an electron is an intrinsic property of each element, making it possible to identify elements and determine their chemical states and concentrations, and is independent of the X-ray source used to eject it. This ensures that XPS measurements are reliable and comparable across different experimental setups.

In a laboratory based XPS setup, the sample surface is irradiated with an X-ray source of fixed wavelength, typically from an Mg (1256.3 eV) or Al (1486.6 eV) anode (Moulder & Chastain, 1992). The emission of photoelectrons occurs only if the incident photon's energy exceeds the electrons' binding energy plus the material's work function. The kinetic energy (KE) of the ejected photoelectrons can be described by the equation (30):

$$KE = hv - BE - \Phi \tag{30}$$

hv is the energy of the X-ray photons, BE is the electron binding energy, and ϕ is the spectrometer's work function. The binding energy can be calculated by knowing the photon energy and measuring the

kinetic energy of the emitted electrons. Each element has a unique spectrum where peaks at specific binding energies reflect the atom's electronic structure. The intensity of each peak depends on the scattering cross-section, which relates to the probability of photon-electron interaction specific to each electronic orbital. When multiple elements are present, the spectrum is a sum of the individual spectra of each element (Stevie & Donley, 2020).

The surface sensitivity of XPS is due to the strong interaction between electrons and matter. The inelastic mean free path (IMFP) of electrons, the average distance an electron travels in a solid before losing energy through interactions, typically ranges from 0.5 to 2 nm. The number of electrons escaping from the solid decreases exponentially with depth, as described by:

$$\mathrm{I(d)} = \mathrm{I(0)} * \exp\left(-\frac{d}{\lambda(\mathrm{KE})}\right) \tag{31}$$

where $\mathrm{I(d)}$ is the number of electrons from a depth d from the surface, $I(0)$ is the number of electrons ejected from the surface at $d = 0$, and $\lambda\ (KE)$ is the IMFP of an electron with a given kinetic energy. Electrons escaping the surface without losing energy form peaks in the spectrum, while others contribute to the background after losing energy through interactions.

XPS is highly sensitive to each element's chemical state and environment of each element, allowing for detailed chemical analysis of the surface. The position of the photoemission lines varies with the element's oxidation state: higher oxidation states generally result in higher binding energies due to increased nuclear attraction. Different compounds with the same oxidation state can show varying shifts in binding energy depending on the electronegativity of neighboring atoms (Stevie & Donley, 2020).

Quantitative analysis is possible by correctly analyzing the spectra and all the features present in the peak structure. The number of electrons emitted for each element is directly proportional to the number of atoms on the sample surface. The intrinsic intensity of a photoemission line is related to the cross-section, which is reported for common anodes and instrument geometries in XPS databases as relative sensitivity factors (RSF). The relative atomic fraction of the elements present on the surface can be estimated by fitting the areas of the photoemission peaks and dividing by the relative RSF values.

As an electron-based technique, ultra-high vacuum (UHV, around 10^{-9} mbar) is needed to prevent collisions of photoelectrons with atmospheric particles, which would decrease the number of photoelectrons reaching the analyzer, thereby limiting the sensitivity and resolution of the spectroscopy (Stevie & Donley, 2020).

Laboratory-based XPS typically operates under ultra-high vacuum (UHV) conditions to avoid the collision of photoelectrons with the atmosphere, which could affect the sensitivity and resolution of the spectroscopy. However, during catalysis, gases are present at high temperatures and pressures, leading to potential discrepancies in the chemical information obtained under UHV conditions. This

phenomenon, known as the "pressure gap" problem, can be partially addressed by employing *near-ambient pressure XPS techniques* (NAP-XPS) (Velasco-Vélez et al., 2016).

NAP-XPS allows for studying catalytic processes under conditions closer to those encountered in real-world applications, thereby providing more accurate chemical information about catalysts during reaction conditions. By bridging the pressure gap, NAP-XPS contributes to a better understanding of catalytic mechanisms and aids in developing more efficient catalysts. Nevertheless, to ensure a proper signal-to-noise ratio of the spectra, synchrotron light sources are commonly employed to carry out this technique.

During the present work, XPS measurements were conducted using the SPECS instrument at the Barcelona Research Centre in Multiscale Science (UPC), equipped with a Phoibos 150 MCD-9 detector. Typically, measurements were conducted using an Mg X-ray source operated at 300 W, with a 0.1 eV step and a pass energy of 20 eV. A high-pressure cell connected to the XPS chambers allowed for sample treatment at high temperatures and pressures, enabling in situ measurements without atmospheric exposure.

3.6.3 Scanning Electron Microscopy (SEM)

Scanning Electron Microscopy (SEM) is an advanced technique for obtaining detailed images of surfaces at the nanoscale, providing valuable topographical information about various devices. Unlike traditional optical microscopes that employ light, SEM uses a focused beam of electrons, offering significant advantages in resolution and depth of field.

SEM functions by directing a high-energy electron beam onto the surface of a sample. The electrons interact with the atoms in the sample, generating various signals that can be detected and utilized to produce an image. These signals include secondary electrons, backscattered electrons, and characteristic X-rays, each providing distinct information about the sample's surface morphology and composition. Secondary electrons, low-energy electrons ejected from the sample surface, yield high-resolution images of surface topography. Backscattered electrons, which high-energy electrons reflected from the sample, provide contrast based on atomic number differences, aiding in the differentiation of materials. In addition, X-rays are produced when the electron beam dislodges inner-shell electrons in the sample atoms, enabling elemental analysis through energy-dispersive X-ray spectroscopy (EDS) (Egerton, 2016).

SEM typically offers a resolution range of 1 nm to 10 nm, allowing visualization of minimal surface features. One of its primary advantages over optical microscopy is its considerable depth of field, enabling a significant portion of the sample to remain in focus simultaneously. Samples for SEM

analysis must be solid and conductive. Non-conductive samples require a thin conductive coating, typically carbon or gold, to prevent charging under the electron beam, thereby preserving image quality. SEM's high resolution enables detailed visualization of tiny surface features, revealing intricate details not observable with optical microscopes. Its significant depth of field provides a comprehensive view of surface morphology, which is essential for analyzing structural features and detecting defects. Additionally, SEM facilitates elemental analysis through EDS, aiding in identifying the sample's elemental composition.

However, SEM also has limitations, including the high cost of purchasing and maintaining instruments, the requirement for high vacuum conditions, and sensitivity to vibrations. Despite these limitations, SEM remains a powerful tool for characterizing surface features at the nanoscale, and it is widely used in materials science, biology, and electronics (Vladár & Hodoroaba, 2020).

In conclusion, SEM's capabilities make it indispensable in scientific research and industrial applications despite the associated costs and sample preparation requirements. SEM plays a crucial role in advancing our understanding of material properties and behaviors.

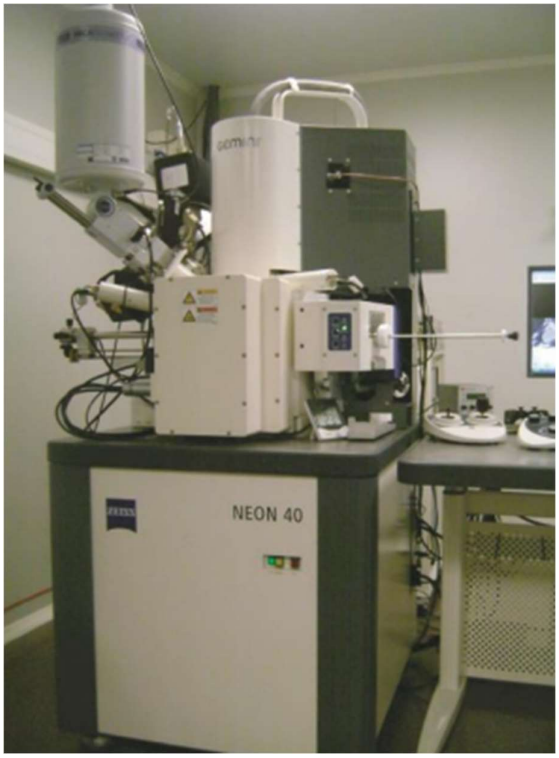

***Figure 16**: Image of the SEM-EDX microscope of the UPC Multiscale facility,*

4. Experimental Methodology

This chapter elucidates the experimental procedures employed in the preparation and characterization of monometallic and bimetallic nickel-based catalysts supported on CeO_2 for the dry reforming of methane. These catalysts were synthesized using incipient wetness impregnation and ball milling methodologies, resulting in six catalysts with three distinct compositions. The primary objective of this phase is to assess how variations in composition and synthesis methods influence the catalytic properties of the materials.

The experimental work was conducted at the Universitat Politècnica de Catalunya (UPC), within the NEMEN research group, specializing in heterogeneous catalysis studies. This section provides a comprehensive overview of the synthesis procedures, emphasizing key parameters and techniques. Stringent adherence to laboratory protocols ensures both safety and reproducibility of results.

4.1 Preparation of the support

The CeO_2 support used in this study is prepared through the hydrothermal method, a process consisting of seven sequential steps. This methodological approach is informed by the research of Ohtake et al. and the patented work of Aozasa et al., ensuring a robust and systematic synthesis protocol (OHTAKE et al., 2017) (Aozasa, 2008).

I. Preparation of Solutions

The initial phase of the hydrothermal synthesis process involves the meticulous preparation of three distinct solutions fundamental for subsequent reactions. These solutions are tailored to provide the necessary chemical environment conducive to CeO_2 formation:

- Solution A: Prepared with a concentration of 1.0 mol/l of $Ce(NH_4)^2(NO_3)^6$ dissolved in deionized water. This solution serves as the precursor for cerium ions in the synthesis.
- Solution B: Formulated with a concentration of 0.35 mol/l of NH_3 in deionized water.
- Solution C: Prepared with a concentration of 2.0 mol/l of NH_3 in deionized water.

II. Mixing of Solution A with Solution B

In this step, the gradual mixing of Solution A with Solution B is essential to ensure a uniform distribution of cerium ions and prevent sudden pH changes. Under vigorous stirring, 195 mL of Solution B is added dropwise to 100 mL of Solution A. This meticulous addition elevates the initial pH from approximately 2 to a final pH of 5. The slow and controlled addition of Solution B, as shown in Figure 17 facilitates the desired chemical reactions, which is crucial for the subsequent synthesis process.

***Figure 17**: Dropwise addition of Solution B into Solution A using a dropping funnel, while constant stirring is maintained with a magnet at 400 rpm.*

III. Reflux Heating

After thoroughly mixing Solutions A and C, the solution undergoes reflux heating for 4 hours at atmospheric pressure. This process, conducted under elevated temperatures, initiates the dissolution of cerium ions and ammonia species, fostering the nucleation and growth of CeO_2 nanoparticles.

As the solution reaches boiling point, transitioning from orange to dark red and finally to light yellow, as seen in Figure 18, thermal hydrolysis occurs, precipitating $Ce(OH)_4$ nanoseeds. This visual transformation marks the onset of crucial chemical reactions essential for the synthesis of CeO_2 nanoparticles. Maintaining reflux conditions throughout ensures the completion of desired chemical transformations, yielding CeO_2 nanoparticles tailored for subsequent catalytic applications.

IV. Centrifugation of the reaction mixture

After the reflux heating, the reaction mixture is centrifugated to separate the solid CeO_2 nanoparticles from the liquid phase. This step ensures efficient separation and recovery of the desired product. Now

containing a yellow precipitate, the mixture is evenly distributed into centrifuge tubes. Centrifugation is conducted under controlled conditions: a speed of approximately 3000 rpm, with a 1-minute ramp-up, 8 minutes of centrifugation, and a 1-minute ramp-down. These parameters optimize the separation process, ensuring that the solid nanoparticles are effectively collected at the bottom of the tubes.

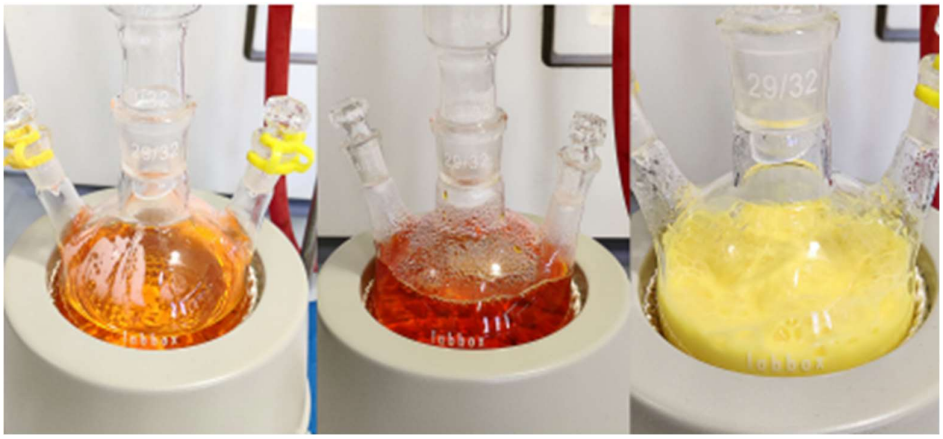

Figure 18: *Precipitation of $Ce(OH)_4$ seeds during the thermal hydrolysis process, coinciding with a noticeable colour change of the solution.*

V. Separation and Retrieval of Wet Cake

The solid CeO_2 nanoparticles settle at the bottom of the centrifuge tubes after centrifugation, forming a wet cake. The acidic liquid remains on top and is carefully decanted to separate it from the solid nanoparticles. The wet cake, composed of the CeO_2 nanoparticles, is then retrieved from the bottom of the tubes and prepared for further processing, as represented in Figure 19.

Figure 19: *CeO_2 nanoparticles settle at the bottom of centrifuge tubes after centrifugation and liquid separation.*

VI. Autoclave treatment

The wet cake obtained from centrifugation is dissolved in 90 mL of Solution C to remove the precipitate. This mixture is then transferred to a stainless-steel autoclave vessel, as depicted in Figure 20.

In the autoclave, the wet cake undergoes hydrothermal synthesis under controlled temperature and pressure conditions. The process is conducted at 180°C and 10 bar of auto-thermal pressure for 2 hours, promoting further crystallization and growth of CeO_2 nanoparticles. This treatment also facilitates solvent removal and nanoparticle consolidation.

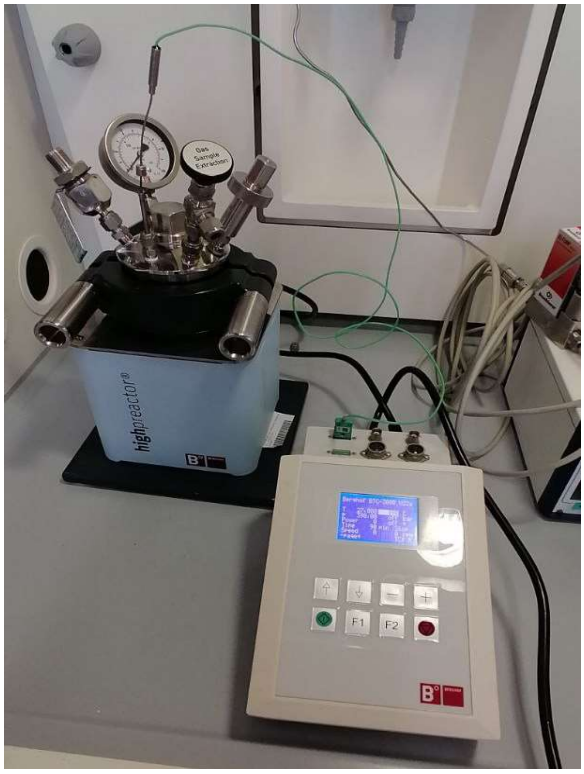

***Figure 20**: Transfer of the mixture into the autoclave chamber, consisting of three components: the hydrothermal bath, the heater, and the thermocouple.*

VII. Filtration and calcination

The final stages of the synthesis protocol involve filtration and calcination of the autoclaved mixture. Filtration is used to separate any impurities from the synthesized CeO_2 nanoparticles, as represented in Figure 21. After filtration, the product undergoes a drying step at 110°C overnight to remove any remaining moisture.

Following drying, the filtered product is subjected to calcination. This step involves heating the product to high temperatures to enhance crystallinity and remove residual solvent molecules. The calcination is

conducted at 950°C for 5 hours in air, with a heating ramp of 5°C per minute. This process is optimized to achieve the desired CeO_2 particle size and phase purity.

***Figure 21**: Filtration process using a ceramic filter connected to a pump and a Kitasato flask, with filter paper inserted, to separate the solvent from the synthesized material.*

4.2 Preparation of catalysts

Before delving into the detailed laboratory procedures followed for catalyst synthesis, the table below outlines catalysts' compositions to be used for the DRM reaction.

***Table 3**: Composition of synthesized catalysts.*

	Ni/CeO_2	**$Ni\text{-}Fe/CeO_2$**	**$Ni\text{-}Fe/CeO_2$**	**Ni/CeO_2**	**$Ni\text{-}Fe/CeO_2$**	**$Ni\text{-}Fe/CeO_2$**
Support	CeO_2_HSA	CeO_2_HSA	CeO_2_HSA	CeO_2_HSA	CeO_2_HSA	CeO_2_HSA
Active phase	Ni 10% w/w_{cat}	Ni 9% w/w_{cat} Fe 1% w/w_{cat} $Ni/_{Fe} = 8.56$	Ni 8% w/w_{cat} Fe 2% w/w_{cat} $Ni/_{Fe} = 3.81$	Ni 10% w/w_{cat}	Ni 9% w/w_{cat} Fe 1% w/w_{cat} $Ni/_{Fe} = 8.56$	Ni 8% w/w_{cat} Fe 2% w/w_{cat} $Ni/_{Fe} = 3.81$
Synthesis technique	Incipient wetness impregnation (IWI)			Ball Milling (BM)		

Regarding the active sites, the total metal content is 10 wt% in all cases. However, in the first case, the catalyst is monometallic, containing only Ni, while in the other two cases, the catalysts are bimetallic with $^{Ni}/_{Fe}$ atomic ratios of 8.56 and 3.81, respectively.

4.2.1 Incipient Wetness Impregnation Method (IWI)

In this study, some monometallic and bimetallic Ni-Fe catalysts were synthesized using the Incipient Wetness Impregnation (IWI) technique, to be used as control samples prepared by a conventional methodology. The IWI method was chosen for its ability to achieve a uniform distribution of metal precursors on the support material. Specifically, three of the six catalysts were prepared using this technique, while the remaining catalysts were synthesized via ball milling, with the aim of comparing both fabrication methodologies in terms of catalytic performance.

For the IWI technique, iron nitrate ($Fe(NO_3)_3 \cdot 9H_2O$) and nickel acetate tetrahydrate ($Ni(CH_3COO)_2 \cdot 4H_2O$) were dissolved in a water and ethanol (1:1) mixture. For bimetallic catalysts, the impregnation was conducted simultaneously. The IWI-prepared catalysts served as reference samples to be directly compared with the ball-milled counterparts.

The experimental procedure was the following:

I. *Drying of Support Material*:

The support oxide material was dried overnight at 110°C in the air to remove any adsorbed moisture. This step ensured that the support was in an optimal state for impregnation.

II. *Estimation of Absorbable Volume*

The volume of liquid that the support could adsorb was determined by adding deionized water until incipient wetness was reached. This approach allowed for the precise calculation of the liquid volume needed to fill the support's pores without excess.

III. *Preparation of Precursor Solution*

Iron nitrate ($Fe(NO_3)_3 \cdot 9H_2O$) and nickel acetate tetrahydrate ($Ni(CH_3COO)_2 \cdot 4H_2O$) were dissolved in a 1:1 water mixture. The total volume of the solution was kept as low as possible to match support's pore volume, ensuring efficient impregnation. For bimetallic catalysts, the precursors were combined in the same solution.

IV. *Impregnation Process*

The calculated volume of the precursor solution, corresponding to the incipient wetness, was added dropwise to the dried support while stirring with a glass rod to ensure homogeneous distribution.

The support material was mixed thoroughly even to coat the precursor on the support.

V. Drying Steps

After each impregnation step, the impregnated powders were dried at 110°C for 2 hours in the air to remove the solvent and fix the precursor on the support. The impregnation and drying steps were repeated until all the precursor solutions had been added to the support.

VI. Final Calcination

The impregnated and dried material was subjected to a final calcination at 400°C for 5 hours in air, with a heating ramp rate of 5°C/min. This step decomposed the nitrate salts, forming active metal oxides and ensuring strong adhesion of the active phases to the support.

An essential aspect of the synthesized catalysts is their distinct visual characteristics, allowing for easy differentiation. The monometallic catalyst containing 10 wt% of Ni is characterized by a typical green color before calcination, which turns to grey-light grey after the calcination step, as can be seen in Figure 22. In contrast, the bimetallic catalysts containing Ni and Fe exhibit a yellow-pale yellow color before calcination, which changes to brown-dark brown after calcination. These visual cues provide a straightforward method to distinguish between the different types of catalysts prepared in this study.

The method described above resulted in catalysts with high metal dispersion and strong interaction between the active components and the support. The final yield of the catalyst precursor was approximately 90-95%, depending on the number of impregnation steps required to achieve the desired metal loading. Typically, the entire impregnation process for Ni-Fe catalysts could be completed within one day, ensuring efficiency and reproducibility in catalyst preparation.

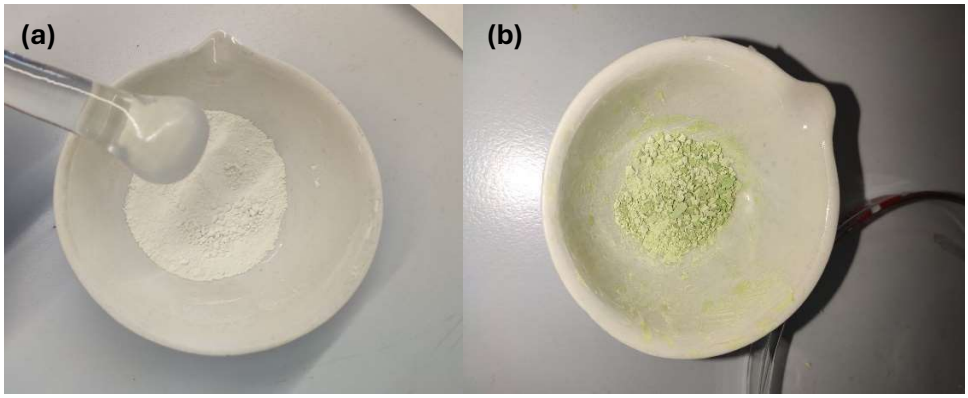

***Figure 22**: Visual comparison of CeO_2 support before (a) and after (b) the impregnation steps with a solution containing 10 wt% of Ni.*

4.2.2 Ball Milling Method

In this master thesis, in comparison with the three catalysts synthesized using the incipient wetness impregnation (IWI) method, a ball miller was used to prepare three out of the six total catalysts. These

samples were prepared using a Pulverizette 23 Mini-Mill (FRITSCH), which is a ball miller equipped with a ZrO_2 jar with an internal volume of 10 mL and a single ZrO_2 ball weighing approximately 10 g and having a diameter of 15 mm. This method can be used to prepare up to 1 g of sample. Alternatively, slightly different millers can be employed for multi-gram synthesis, highlighting the flexibility and scalability of the ball milling technique.

The key to successful catalyst preparation using ball milling lies in the careful selection of milling parameters, which significantly influence the final properties of the catalysts. Based on a previous internal report of the research group, the following parameters were chosen: a milling frequency of 30 Hz, a milling duration of 15 minutes, and a ball-to-powder (BPR) weight ratio of 20. These parameters were previously optimized to ensure efficient energy transfer and homogeneity of the samples.

The milling process begins with placing nickel and iron precursors, $Ni(CH_3COO)_2 \cdot 4H_2O$ and $Fe(NO_3)_3 \cdot 9H_2O$ respectively, into the ZrO_2 jar along with the support material. The high-frequency vertical movement of the ball miller facilitates stable bonding between the active metals and the support. This process is less complex than the IWI method, involving fewer steps while achieving an effective, reproducible and scalable catalyst synthesis by mechanochemistry.

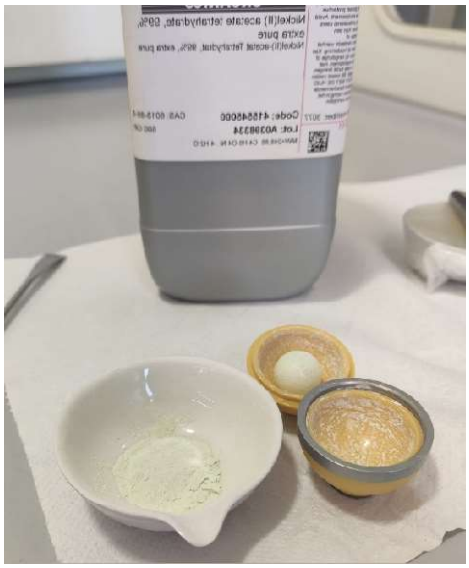

***Figure 23**: The ZrO_2 jar and single ZrO_2 ball used in synthesizing the 10% by weight Ni catalyst on CeO_2.*

After milling, the samples are subjected to a post-processing step involving drying and calcination. The milled samples are kept in an oven at 110°C for 2 hours to remove residual moisture. This step is followed by calcination at 400°C for 5 hours, ensuring the adhesion of the active metal phases onto the support. The controlled heating process promotes the decomposition of metal precursors and the formation of active metal oxides, which are crucial for catalytic activity.

As previously mentioned, the visual appearance of the catalysts, specifically their color changes, provides a practical indicator for differentiation. Similar to the IWI synthesis method, distinct color transitions occur before and after the final calcination step, allowing for straightforward identification of the catalysts prepared.

From a comparison between the two methods, the ball milling method offers a streamlined and efficient approach to catalyst synthesis, with fewer steps compared to the IWI method. While IWI involves multiple impregnation and drying cycles to ensure uniform metal distribution, ball milling achieves this through high-energy mechanical forces in a single step. This reduction in complexity not only saves time but also minimizes the use of solvents and energy, enhancing the sustainability of the process.

Ball milling provides greater control over the milling parameters, such as frequency, time, and ball-to-powder ratio, which can be precisely adjusted to tailor the catalyst properties. In contrast, IWI relies heavily on achieving the correct impregnation volume and ensuring thorough drying at each step, which can introduce variability.

In summary, while the IWI method is well-established in the field of heterogeneous catalysis and provides excellent control over the metal loading on the support, ball milling emerges as a highly efficient and sustainable alternative. It simplifies the synthesis process, reduces the number of steps involved, and offers scalability for larger quantities. The distinct visual characteristics of the catalysts synthesized by both methods further aid in their differentiation and comparison, providing valuable insights into the effectiveness of each technique.

4.3 Catalytic Testing

Catalytic activity tests were performed using a fixed-bed reactor system, exemplified in Figure 24, and operated with Microactivity Effi Solo equipment (Process Integral Development Eng & Tech). Prior to these tests, meticulous calibration ensured precision. Mass flow controllers were fine-tuned to regulate gas flow rates accurately, employing various gas mixtures for validation. Similarly, gas chromatograph (GC) signals were calibrated using diverse gas mixtures to precisely quantify reaction product concentrations. These steps optimized the experimental setup for consistent and reliable results.

The setup comprised four gas feeds: hydrogen (H_2) for catalyst reduction, nitrogen (N_2) as a sweeping gas, and the reactants methane (CH_4) and carbon dioxide (CO_2). The fixed-bed reactor, constructed from a high-quality quartz tube with an internal diameter of 10 mm, featured a catalytic bed positioned centrally. This bed, consisting of foam materials, was protected by a layer of quartz wool to prevent contamination, ensuring optimal catalytic performance.

The reactor was loaded with 100 mg of catalyst sample, diluted with silicon carbide (Alfa Aesar, 46 grit) at a mass ratio 12 to enhance the total bed volume. Temperature regulation was achieved through a sophisticated heating system controlled by an Omega controller, a variable transformer, and a K-type thermocouple in direct contact with the catalytic bed. Precision pressure gauges on each gas feed line monitored pressure drops, ensuring accurate data collection.

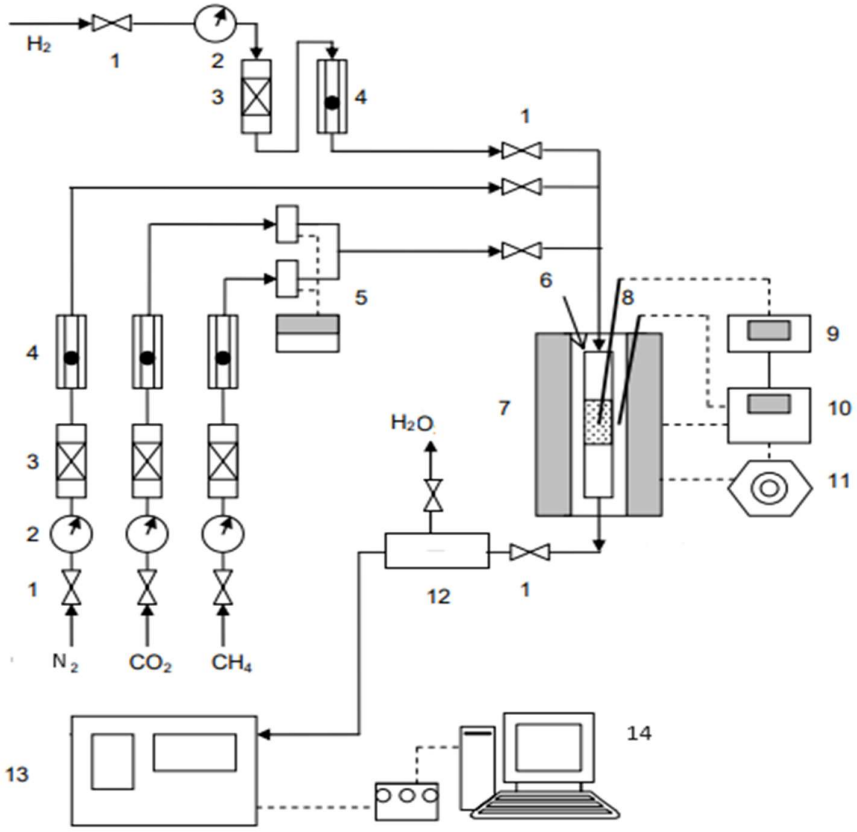

***Figure 24**: Scheme of the reaction system used.(1) Shut-off valve (2) Pressure gauge (3) Desiccator (4) Rotameter (5) Mass flow control system (6) Reactor (7) Electric Furnace (8) Thermocouple (9) Thermometer (10) Temperature control (11) Variable Transformer (12) Condenser (13) Gas Chromatography (14) Data Acquisition.*

A condenser at the reactor outlet removed liquid water from the gas stream, sealed by a dedicated valve to prevent gas losses. The gaseous effluent was analyzed using a 490 Micro GC (Agilent Technologies) with an advanced molecular sieve, a Stabilwax and a PoraPlot U columns technology, ensuring accurate gas concentration quantification.

Before initiating the methane reforming reaction, a catalyst activation process through reduction must be conducted. This step involves exposing catalyst samples to 10% hydrogen dilutes in a nitrogen stream for one hour at 400°C, with a controlled heating rate of 5°C/min and a total flow of 50 ml/min. This thermal treatment effectively reduces the catalyst precursors, preparing a stable and highly reactive catalytic environment for the subsequent reaction.

Catalytic tests were conducted under specific conditions: a total gas flow rate of 125 ml/min and a CO_2:CH_4:N_2 ratio of 1:1:4, achieving a gas hourly space velocity (GHSV) of 10,000 h^{-1}.

***Figure 25**: Quartz reactor showing a fixed bed composed of foam support, a quartz wool layer, and a silicon carbide catalytic bed with a nickel monometallic catalyst.*

Throughout the DRM reaction tests, the temperature played a crucial role in influencing catalytic activity and product selectivity. For this reason, the reaction temperature was systematically varied between 550°C and 950°C, with intervals of 50°C. At each temperature step, the reaction conditions were carefully maintained for 45 minutes to allow sufficient time to establish a steady-state reaction regime. This approach enabled a comprehensive investigation of the temperature dependence of catalytic activity, providing valuable insights into reaction kinetics and catalyst performance under varying conditions.

The gaseous effluent from the reactor was then analyzed using the gas chromatograph. The amount of N_2 served as an internal standard to calculate the total dry flow at the GC. This approach was adopted because the volume and corresponding moles of N_2 remain constant throughout the process. These calculations are essential because it is necessary to consider that the number of moles of products is greater than the number of moles of reactants. As a result, we expect the outgoing flow to be consistently higher than the incoming flow.

Furthermore, manual flow measurements were taken during the catalytic testing to compare with the calculated flows. Subsequently, an Excel spreadsheet was used to analyze the GC files, calculating the molar flows from the total flow and each gas percentage. This comprehensive analysis facilitated the

determination of catalytic activity quantities, such as methane conversion and hydrogen selectivity, providing valuable insights into the catalytic performance under the tested conditions.

In addition to the activity tests, stability tests were conducted on bimetallic catalysts with more iron, which were synthesized by ball milling and incipient wetness impregnation methods. Stability tests were carried out over 24 hours at 700°C under the same flow and gas hourly space velocity as for the catalytic tests. The outlet stream was analyzed every 20 minutes using the same microGC. After the tests, the spent catalyst was separated from the SiC by sieving the catalytic bed using a 200 µm sieve to characterize the post-reaction samples.

5. Results and Discussion

In this chapter, we will delve into the results obtained from the six synthesized catalysts. Our primary objective is to compare the performance and characteristics of catalysts prepared using two different synthesis methods, Incipient Wetness Impregnation (IWI) and Ball Milling (BM), as well as three distinct compositions. This comparative analysis will enable us to identify the most suitable conditions for the dry reforming of methane (DRM) reaction.

We will begin by examining the catalytic performance of each catalyst in the DRM reaction. Subsequently, we will conduct a comprehensive characterization of the catalysts both before and after the reaction. This characterization will include techniques like Raman spectroscopy, X-ray photoemission spectroscopy (XPS), and scanning electron microscopy (SEM) to investigate changes in catalyst structure, composition, and morphology.

5.1 Activity tests

After carefully preparing the reaction setup, the analysis of the activity tests was conducted. The results were plotted to show the relative conversion of the two reactants involved, CH_4 and CO_2, as well as the ratio between the two desired products, H_2 and CO. The objective is to maximize hydrogen production as much as possible; therefore, the molar ratio of the two products is a crucial indicator of the performance and applicability of the catalytic process used. Relative conversion, X_i, and ratio, R, were calculated according to the following expressions (32, 33), where $n_{i,IN}$ and $n_{i,OUT}$ represent the inlet and outlet molar flows of species i (mol/min). The results of the activity tests are consistent because they represent the average of three different experiments conducted under the same operating conditions. For this reason, appropriate error bars have been included, indicating an error range of 4% to 6% for each value associated with different temperatures.

$$X_i = \frac{n_{i,IN} - n_{i,OUT}}{n_{i,IN}} * 100 \tag{32}$$

$$R = \frac{n_{H_2,OUT}}{n_{CO,OUT}} \tag{33}$$

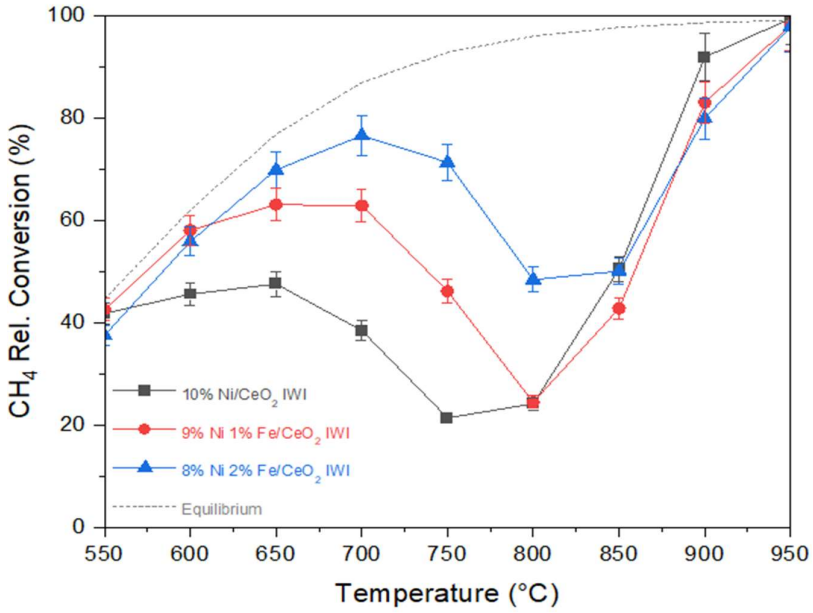

***Figure 26**: Effect of the Temperature on CH_4 Relative Conversion for Catalysts Synthesized via IWI Method.*

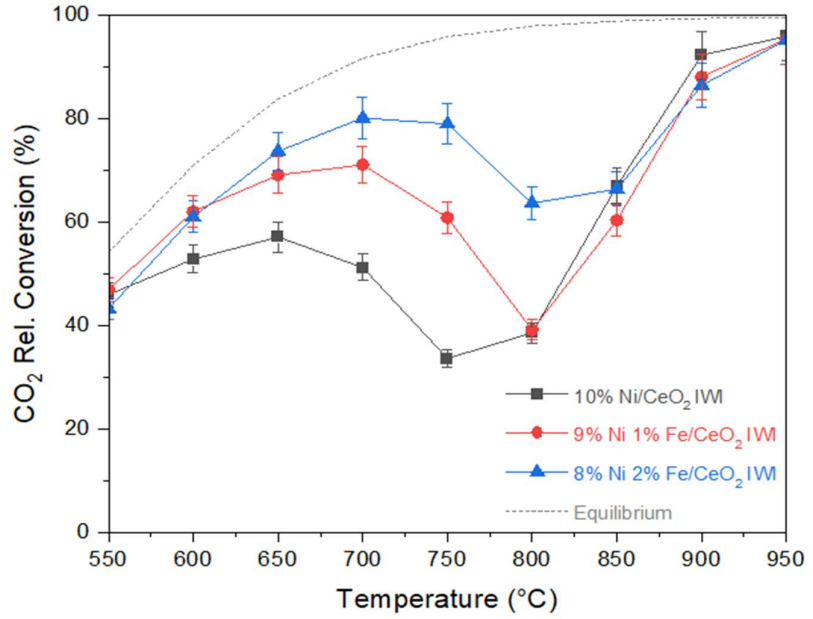

***Figure 27**: Effect of the Temperature on CO_2 Relative Conversion for Catalysts Synthesized via IWI Method.*

The analysis of the CH_4 and CO_2 Relative Conversion graphs for catalysts synthesized using the incipient wetness impregnation (IWI) method reveals significant variations in conversion rates depending on the catalyst composition. The thermodynamic trends depicted in these graphs confirm that CO_2 conversion is generally higher than CH_4 conversion, a finding that was further validated

experimentally. This observation aligns with theoretical expectations, as CO_2 decomposition is thermodynamically more favorable than CH_4 conversion under the experimental conditions tested.

The incorporation of iron (Fe) in the synthesis of bimetallic catalysts plays a pivotal role in enhancing catalytic activity at moderate to low temperatures. Specifically, the addition of Fe leads to a notable increase in reactant conversion compared to monometallic catalysts containing only 10 wt% of nickel (Ni). For this reason, the catalyst with 8 wt% Ni and 2 wt% Fe, with an atomic ratio $^{Ni}/_{Fe} = 3.81$, shows approximately a 20% increase in conversion rates in the temperature range of 650-750°C. This enhancement can be attributed to the synergistic effects between Ni and Fe, which promote more efficient catalytic pathways, possibly by altering the electronic properties of the active sites or improving dispersion on the surface of the support.

It is also crucial to consider the gradual deactivation of catalysts over time. Contrary to thermodynamic and kinetic expectations of linear conversion growth with increasing temperature, a gradual deactivation trend is observed. The addition of Fe appears to effectively delay this deactivation, shifting it to higher temperatures. This reduced deactivation in Fe-containing catalysts, particularly with the addition of 2% by weight, suggests an improved longevity in maintaining high catalytic performance. The iron could act as a stabilizing agent, preventing sintering or coke formation, which are common causes of catalyst deactivation.

At 950°C, the conversion values for the three catalysts converge due to thermodynamic and catalytic phenomena. At these temperatures, coke formation is thermodynamically inhibited, and existing coke is removed via the CO_2 gasification reaction, which is favored kinetically. The CeO_2 support further enhances this process through its redox properties, promoting coke oxidation and limiting its deposition. Simultaneously, the elevated temperature drives the endothermic DRM reaction, maximizing reactant conversions close to thermodynamic equilibrium and diminishing differences among the catalysts despite partial deactivation.

It is also possible to assess the selectivity of the catalysts under study. Selectivity is a crucial parameter in determining how efficiently the catalysts can direct the reaction towards the desired products, which in this case are H_2 and CO.

The catalysts with a higher amount of Fe in their bimetallic composition demonstrate improved performance at intermediate temperatures regarding the H_2/CO ratio, as shown in Figure 28. This enhancement suggests that the presence of Fe not only increases the conversion rates of the reactants but also influences the distribution of the products. At higher temperatures, the monometallic catalyst slightly outperforms the bimetallic ones, achieving similar H_2/CO ratio values.

However, across different temperature ranges, this ratio remains below 1. This outcome can be attributed to secondary reactions, such as the reverse water-gas shift reaction, which actively consumes the produced H_2, thereby reducing the H_2/CO ratio.

These findings underscore the significant impact of catalyst composition on optimizing both the activity and selectivity of the reaction. The improved performance of bimetallic catalysts with higher Fe at lower and intermediate temperatures represents a valuable discovery, as it opens up new possibilities for the investigation and use of bimetallic catalysts composed of two non-noble metals, such as Ni and Fe. This approach offers a cost-effective alternative to noble metal catalysts, which are typically more expensive. Such advancements could pave the way for more sustainable and economically viable catalytic processes in methane dry

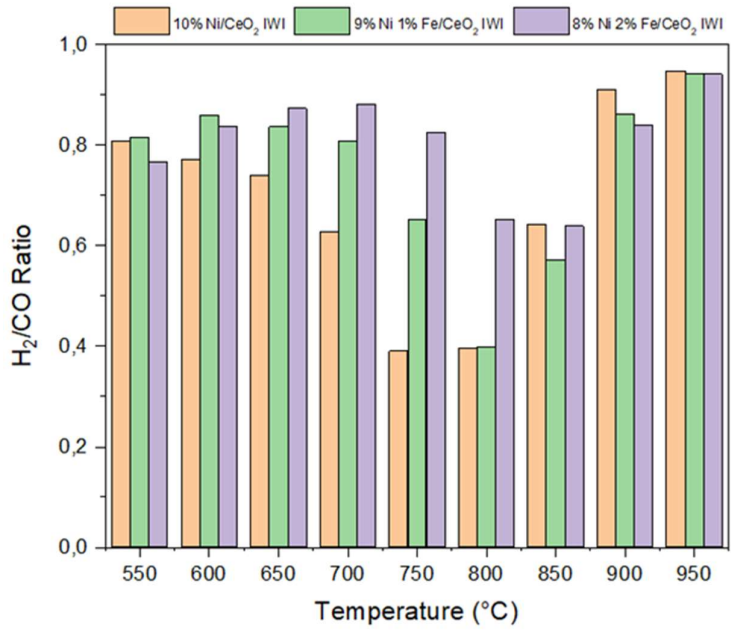

***Figure 28**: Effect of the Temperature on H_2/CO Ratio for Catalysts Synthesized via IWI Method.*

Further analysis of the catalysts synthesized using the BM method could provide additional insights into the mechanisms influencing these outcomes.

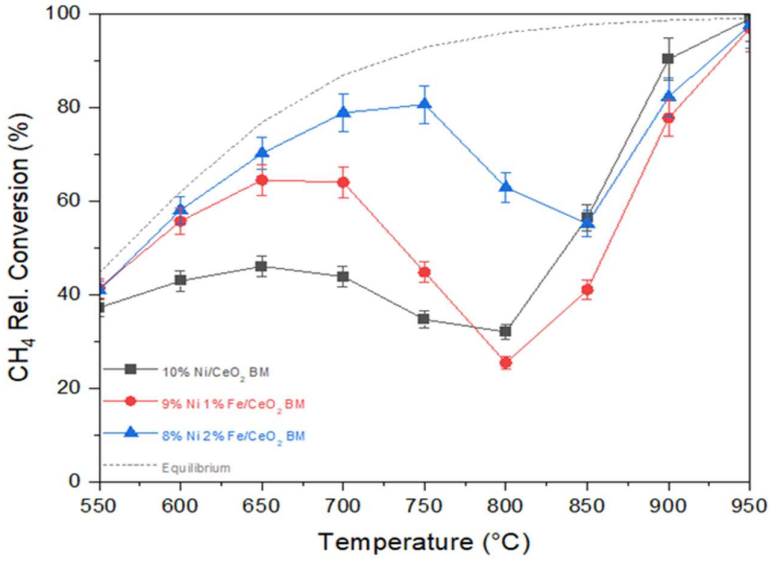

***Figure 29**: Effect of the Temperature on CH_4 Relative Conversion for Catalysts Synthesized via BM Method.*

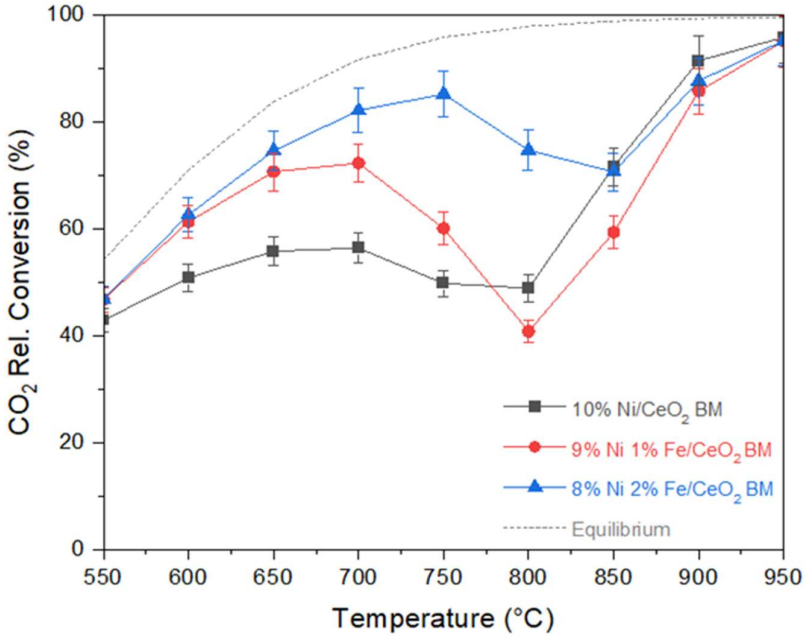

***Figure 30**: Effect of the Temperature on CO_2 Relative Conversion for Catalysts Synthesized via BM Method.*

As observed from Figures 29 and 30, the performances of the three catalysts synthesized via the BM method are comparable to those previously analyzed. The synergy between nickel and iron enhances the conversion rates of the two reactants, CH_4 and CO_2, particularly at moderate to low temperatures. This enhancement can be attributed to the improved dispersion and interaction of the active metals on the catalyst support, which promotes more effective catalytic activity.

Indeed, the bimetallic catalyst with a higher quantity of Fe demonstrates superior performance in achieving higher conversion rates within these temperature ranges. The presence of Fe appears to facilitate the catalytic process by modifying the electronic properties of Ni, leading to more efficient adsorption and activation of the reactants. Additionally, Fe may prevent the agglomeration of Ni particles, maintaining a higher active surface area and thus enhancing the overall catalytic performance.

However, despite the different synthesis technique, intermediate temperatures lead to the deactivation of the catalysts and a gradual reduction in their activity. An initial comparison reveals that the bimetallic catalyst containing only 1 wt% Fe experiences more pronounced deactivation than what was observed with the catalysts synthesized by the IWI method. This difference could be due to the varying distribution and interaction of the metal particles on the support surface, which might influence the stability and resilience of the catalysts under operational conditions.

Furthermore, the analysis includes thermodynamic studies on CO_2 and CH_4 conversion, revealing that at each temperature level, the experimental results show a higher conversion of CO_2 than CH_4. This outcome aligns with the thermodynamic predictions, as CO_2 is more readily activated and converted under the reaction conditions due to its lower activation energy and favorable reaction pathways.

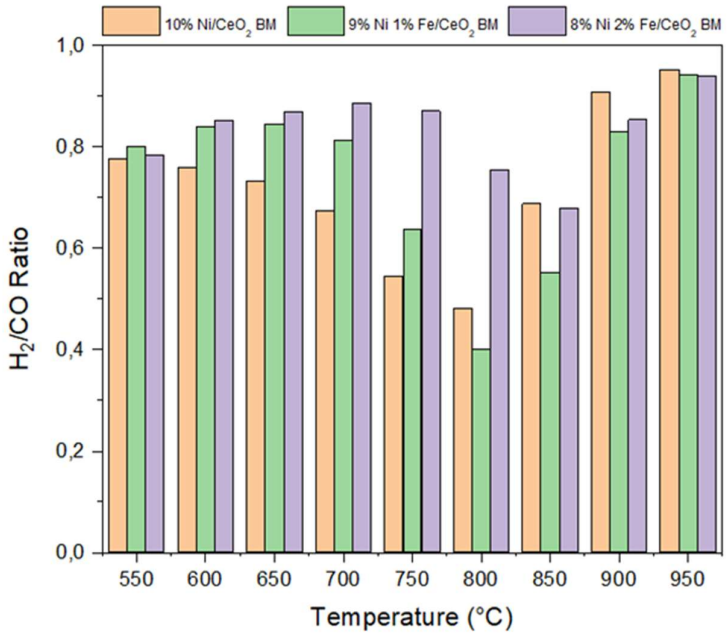

***Figure 31**: Effect of the Temperature on H_2/CO Ratio for Catalysts Synthesized via BM Method.*

An analysis of the histograms representing the H_2/CO ratio reveals that the bimetallic catalyst with a higher Fe content significantly enhances H_2 selectivity at intermediate temperatures. This improvement is particularly evident in the temperature range of 700 to 800°C, where higher H_2/CO ratios are observed. This suggests that the addition of Fe not only boosts catalytic activity but also influences the product distribution, favoring the production of H_2 over CO.

The increase in the H_2/CO ratio with higher Fe content can be attributed to the enhanced dispersion and interaction of the metal particles, which promotes more effective hydrogen production while suppressing secondary reactions, like the Reverse Water-Gas Shift reaction that consumes H_2.

From these findings, it can be concluded that the two synthesis techniques, BM and IWI, produced catalysts with similar trends in activity and selectivity. However, a detailed comparison among the three different compositions reveals that the bimetallic catalyst containing 2% by weight of Fe exhibits the highest activity and stability, even though it undergoes partial deactivation at intermediate temperatures.

Given the performance differences observed between the synthesis techniques, it is essential to further assess the advantages of each fabrication method. The BM method, known for its simplicity, cost-effectiveness, and environmental sustainability, could offer a viable alternative to traditional synthesis techniques if it can produce catalysts with comparable or superior activity and selectivity.

To evaluate this potential, a comparison was conducted between the three catalysts synthesized via the IWI technique and the best-performing catalyst synthesized via the BM method. This comparison enables a comprehensive analysis of both conversion efficiency and selectivity, allowing for the results

to be represented in a single graph. This graphical representation provides a clearer overview of the catalysts' performance in the DRM reaction.

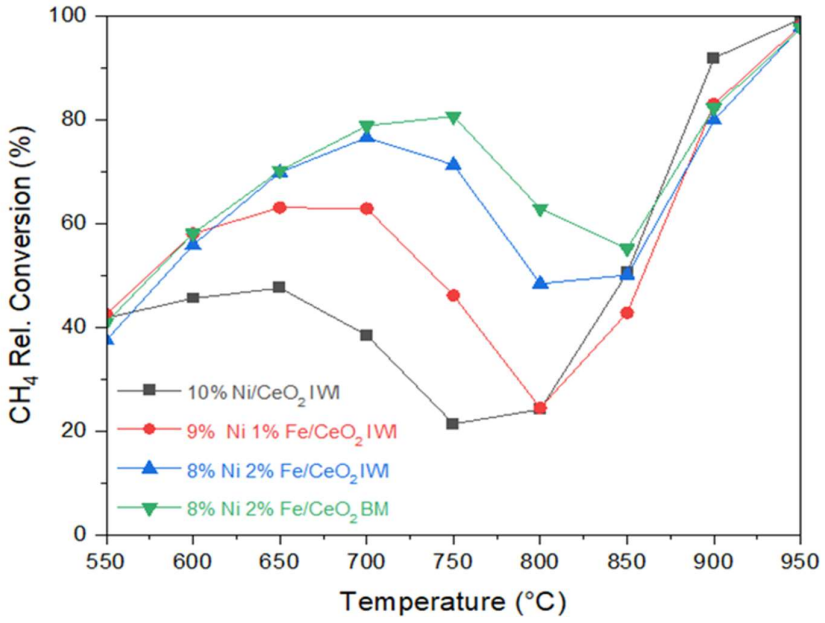

***Figure 32**: Comparison of CH_4 Relative Conversion for Catalysts Synthesized by IWI and BM methods.*

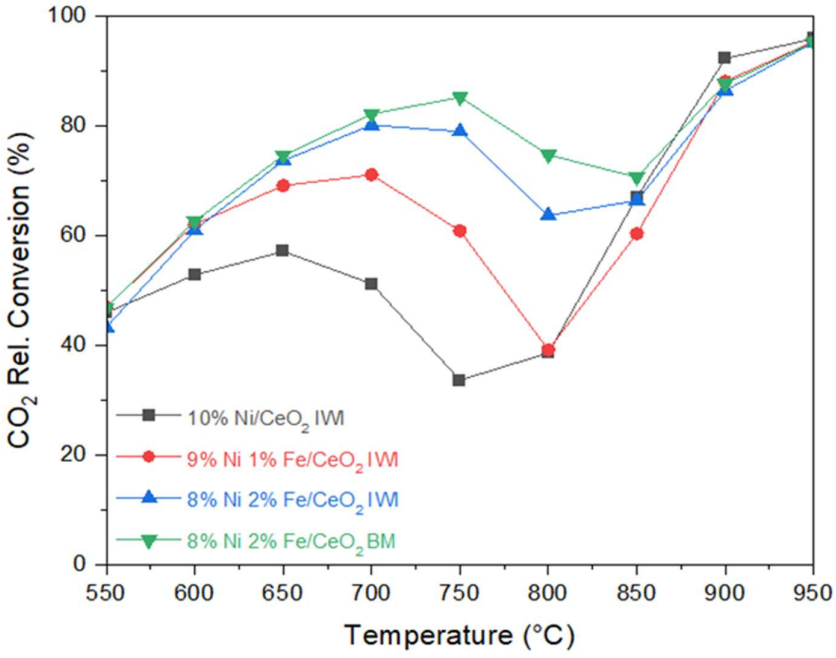

***Figure 33**: Comparison of CO_2 Relative Conversion for Catalysts Synthesized by IWI and BM methods.*

As depicted in Figures 32 and 33, the bimetallic catalyst containing 2 wt% Fe and 8 wt% Ni, prepared via the BM method, exhibits slightly superior performance compared to the equivalent catalyst

synthesized by the IWI method. Specifically, the BM catalyst demonstrates higher conversion rates for both CH_4 and CO_2 across most of the examined temperatures. This finding is significant because it demonstrates that the BM method is an innovative and sustainable synthesis approach, producing catalysts with performance comparable to those from the conventional IWI method. Although BM catalysts show higher average performance, taking into account the error bars, the results indicate that both methods can achieve similar catalytic activity under certain conditions. Thus, the BM method presents a promising alternative for catalyst preparation, offering environmental benefits while maintaining competitive performance.

The enhanced performance of the BM-prepared catalyst can be attributed to the improved dispersion and interaction of the active metal components within the catalyst matrix, a direct result of the mechanical energy applied during the ball milling process. Therefore, the BM method represents a promising alternative for the synthesis of effective bimetallic catalysts, combining ease of preparation with high catalytic efficiency. This highlights the potential of BM as a viable and advantageous synthesis technique in the field of catalyst development.

Figure 34 shows the H_2/CO ratio as a function of temperature for the same catalysts analyzed previously. From the graph, it is evident that the bimetallic catalyst with 2 wt% Fe prepared via the BM method generally demonstrates higher H_2/CO ratios across a broad temperature range compared to its IWI counterpart. This suggests a more favorable production of hydrogen relative to carbon monoxide, which is beneficial for applications requiring syngas with a higher hydrogen content.

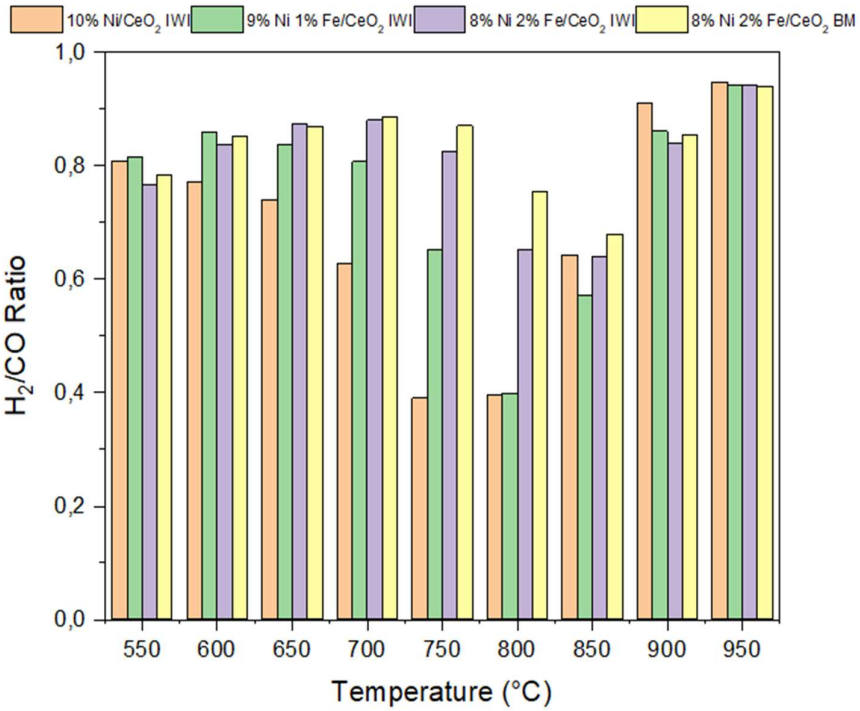

***Figure 34**: Comparison of H_2/CO Ratio for Catalysts Synthesized by IWI and BM methods.*

However, it is important to note that the differences in selectivity between the BM and IWI catalysts are not excessively large.

In conclusion, the BM method provides a simple and sustainable synthesis route that yields catalysts with improved performance characteristics. The bimetallic catalyst with 2 wt% iron prepared by BM not only achieves higher conversion rates for CH_4 and CO_2 but also offers comparable, if not better, selectivity as indicated by the H_2/CO ratio. Therefore, the BM method stands out as a viable and effective alternative for catalyst preparation, capable of delivering high catalytic activity and selectivity akin to those obtained through the traditional IWI method.

5.2 Stability Tests

The stability tests, conducted over a 24-hour duration, are crucial for assessing the long-term performance of the catalysts. Stability, alongside activity and selectivity, is one of the three key properties that define an effective and efficient catalyst. These tests provide insight into the potential degradation mechanisms and the resilience of the catalysts under extended operational conditions.

For this analysis, stability tests were performed on two of the highest-performing catalysts identified in previous activity tests: the bimetallic catalysts containing 2 wt% Fe, synthesized using the Incipient Wetness Impregnation (IWI) and Ball Milling (BM) methods, both with a $Ni/_{Fe}$ atomic ratio of 3.81. These catalysts were chosen due to their superior initial performance in CH_4 and CO_2 conversion, as well as their favorable H_2/CO ratios.

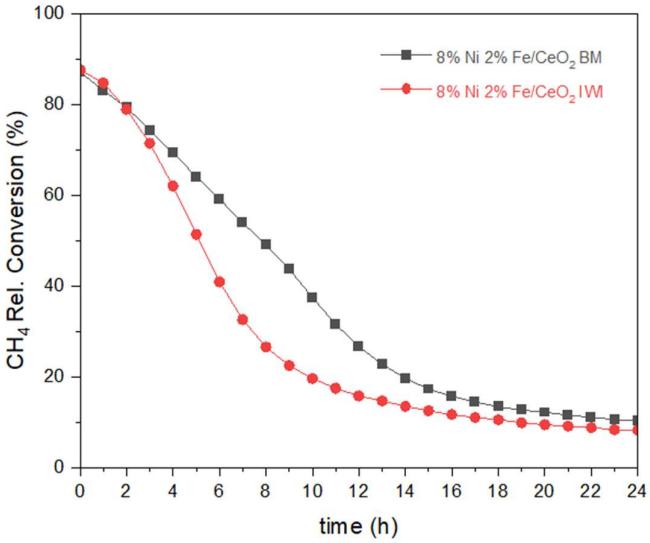

***Figure 35**: Effect of the time on CH_4 Relative Conversion for Catalysts Synthesized via IWI and BM Method at 700°C for 24 h.*

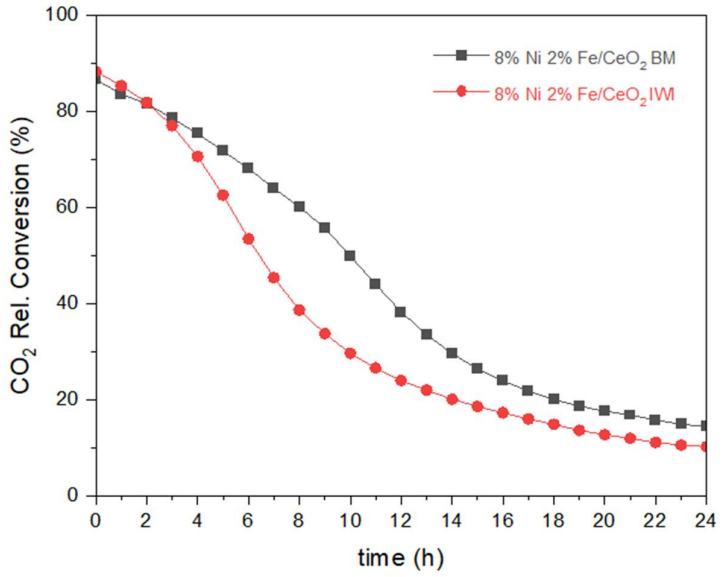

***Figure 36**: Effect of the time on CO_2 Relative Conversion for Catalysts Synthesized via IWI and BM Method at 700°C for 24 h.*

After catalyst activation through reduction, the dry reforming of methane (DRM) reaction was conducted at 700°C for 24 hours.

The comparative analysis of the stability tests, illustrated in the Figures 35 and 36, reveals a gradual decline in CH_4 and CO_2 conversion rates for both catalysts. This trend indicates progressive catalyst deactivation, a common challenge in catalytic processes that can result from factors such as sintering, carbon deposition, or the agglomeration of active metal particles.

In the CH_4 conversion graph, both the BM and IWI catalysts start with high conversion rates, around 80%, which consistently decrease over the 24-hour period. By the end of the test, conversion rates for both catalysts had diminished significantly, approaching levels seen in the absence of a catalyst. This substantial reduction underscores the extent of deactivation, which negatively impacts the efficiency of the catalytic process.

Similarly, CO_2 conversion rates follow the same declining trend, reinforcing the observation that both catalysts experience a loss of activity over time. This decline suggests that the active sites of the catalysts are becoming less effective, potentially due to changes in metal dispersion and/or the accumulation of coke over the catalyst surface.

The H_2/CO ratio graph further supports these findings, showing a decrease in selectivity as the catalysts lose activity. A lower H_2/CO ratio indicates a shift towards less favorable reaction pathways, which could impact the overall efficiency of syngas production.

Although both catalysts exhibit deactivation, the BM-synthesized catalyst demonstrates slightly better stability over time compared to the IWI catalyst. This could be attributed to the enhanced dispersion and interaction of the active metals within the catalyst matrix achieved through ball milling. However, the difference between the two is modest, indicating that both synthesis methods remain viable for producing effective catalysts.

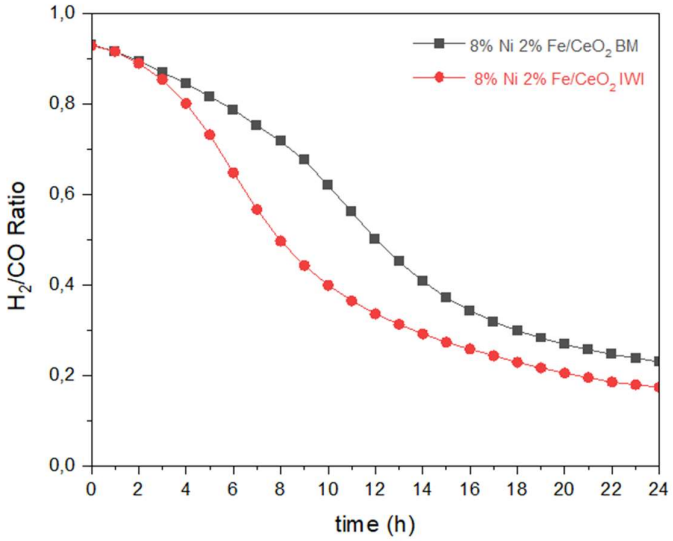

***Figure 37**: Effect of the time on H_2/CO Ratio for Catalysts Synthesized via IWI and BM Method at 700°C for 24 h.*

In conclusion, the stability tests highlight the challenges of maintaining catalyst performance over extended periods. While the BM method shows a slight advantage in stability, both methods produce catalysts that are susceptible to deactivation. These results underscore the need for ongoing research to develop strategies that enhance catalyst durability, such as optimizing synthesis conditions or exploring new materials that resist deactivation.

5.3 Catalysts Characterization

Following the catalytic performance tests, it is essential to delve into the characterization of the catalysts, both before and after the reaction. This analysis will provide valuable insights into their morphology, composition, oxidation states, and surface components. A comprehensive examination of these aspects is crucial for understanding the structural and chemical changes the catalysts undergo during the reaction, which directly influence their activity and stability. By exploring these transformations, we can better interpret the catalysts' behavior and performance, paving the way for potential improvements and optimizations.

5.3.1 Raman Characterization

In this study, Raman spectroscopy was utilized as a powerful tool to characterize the catalysts and to provide in-depth information about the nature of the active sites and the evolution of the catalyst structure under DRM reaction conditions.

We will focus on the qualitative analysis of Raman spectra. Given the nature of this analysis, the peak intensities are presented in arbitrary units (a.u.). By comparing these spectra, we aim to elucidate the compositional changes and the influence of the synthesis method on the catalyst structure.

The Raman spectrum of pure CeO_2 shows a distinct peak at approximately 465 cm^{-1}, which corresponds to the F_2g vibrational mode of the Ce-O bond in the fluorite structure (Kosacki et al., 2002). The sharpness of this peak signifies the well-defined crystalline nature of the CeO_2 support. This characteristic plays a crucial role in the catalyst's performance, as it influences the interaction between the support and the active metal species.

The introduction of 10 wt% Ni into the CeO_2 support leads to the emergence of a broad peak in the 500-600 cm^{-1} region, as observed in Figure 39. This peak can be attributed to the interaction between NiO and CeO_2, which is critical for catalytic activity. This interaction has the potential to modify the electronic properties of nickel oxide, potentially enhancing its catalytic behavior (Liu et al., 2016). Additionally, the main CeO_2 peak at 465 cm^{-1} undergoes a slight shift to around 460 cm^{-1}. This shift could be attributed to changes in particle size or crystallinity resulting from the incorporation of nickel.

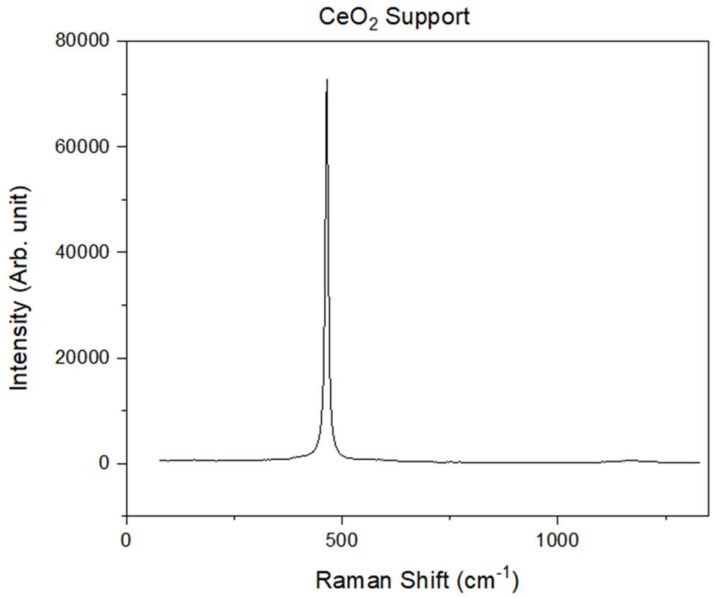

***Figure 38**: Raman spectrum of CeO_2 support.*

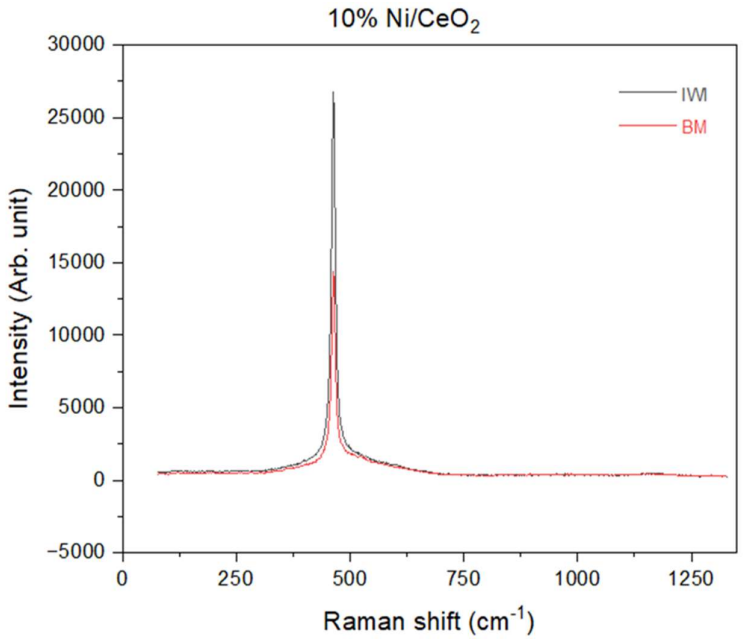

***Figure 39**: Raman spectra of 10 wt% Ni/CeO_2 catalysts prepared by IWI (black) and BM (red) methods.*

Upon introducing iron to the Ni/CeO_2 catalysts, the peak in the 500-600 cm^{-1} region intensifies, as evidenced in Figure 40. This increase suggests that the presence of iron strengthens the interaction between nickel oxide and the CeO_2 support. This reinforcement might be due to iron influencing the dispersion of nickel particles on the support or altering the electronic environment, leading to a more robust NiO/CeO_2 interaction.

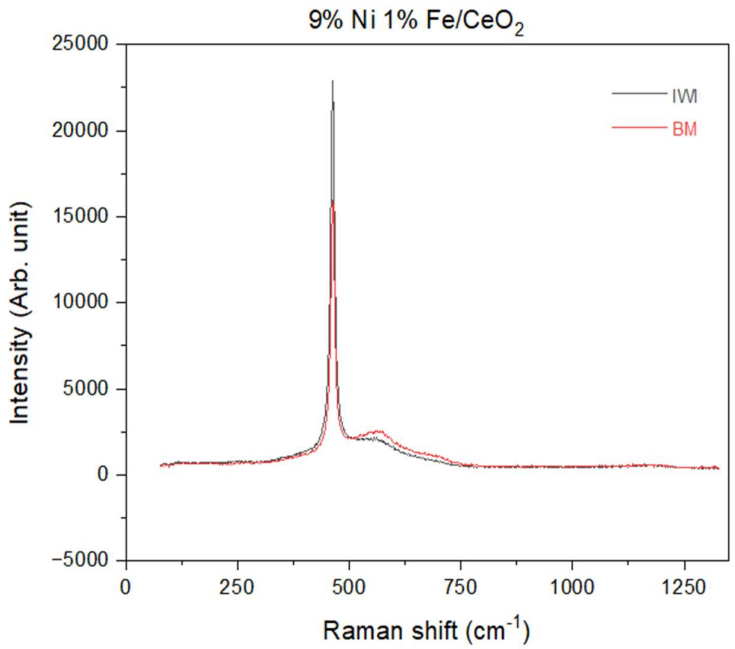

***Figure 40**: Raman spectra of 9 wt% Ni 2 wt% Fe/CeO_2 catalyst prepared by IWI (black) and BM (red) methods.*

Furthermore, the inclusion of iron introduces a new peak around 700 cm^{-1}. This peak is assigned to iron oxide species (likely Fe^{3+}) interacting either with nickel or directly with the CeO_2 support. The growing intensity of the 700 cm^{-1} peak with increasing iron content indicates that iron not only introduces new species but also influences the overall interaction dynamics within the catalyst. This effect contributes to both the NiO/CeO_2 interaction and the formation of mixed metal oxides or other complex structures.

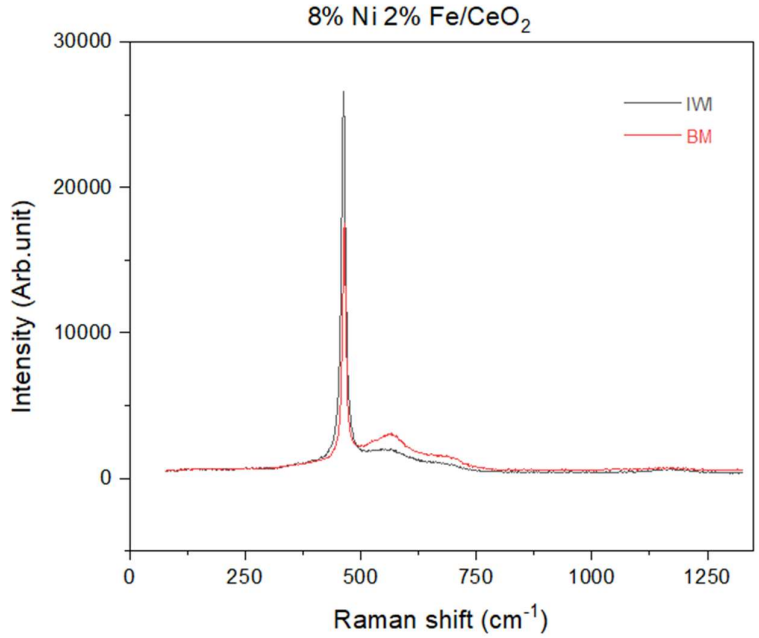

***Figure 41**:Raman spectra of 8 wt% Ni 2wt% Fe/CeO_2 catalyst prepared by IWI (black) and BM (red) methods.*

Based on the obtained results, it is evident that the synthesis method influences the properties of the catalysts. A comparison of catalysts reveals that ball milling generally leads to sharper and more pronounced Raman peaks. This observation suggests that the mechanical forces involved in ball milling enhance the metal-support interactions, likely due to improved metal dispersion and increased contact between the metal and the support. Moreover, the sharper peaks could indicate a higher degree of crystallinity or more defined structural features, which are desirable characteristics for promoting catalytic performance and stability.

After the DRM reaction, further analysis was conducted to investigate the deposition of carbonaceous species on the catalysts' surfaces. This study is crucial for understanding the nature and extent of carbon formation, which directly influences the catalysts' performance and longevity.

The Raman spectra obtained post-reaction, as depicted in the Figure 42, reveal three prominent bands: the D band (~1350 cm^{-1}), the G band (~1580 cm^{-1}), and the D' band (~1615 cm^{-1}). Each of these bands offers valuable insights into the type of carbon present (Bokobza et al., 2015):

- D band: Associated with defects and disorder in the carbon lattice, typically found in amorphous carbon structures or edge defects in crystalline graphene. A pronounced D band indicates a substantial amount of disordered or amorphous carbon, suggesting that coke formed on the catalyst surfaces may contain significant structural defects.
- G band: Corresponds to the in-plane vibrational mode of sp^2 bonded carbon atoms in a graphitic lattice. The intensity of the G band provides information about the extent of graphitic carbon formation, which is generally undesirable as it can lead to catalyst deactivation by blocking active sites or causing structural damage through carbon filament formation.
- D' band: Linked to additional structural disorder or defects in the carbon lattice, indicating polycrystalline graphitic materials or more complex defect structures. The presence of the D' band suggests a varied distribution of carbon types within the catalysts, with both graphitic and disordered carbon present.

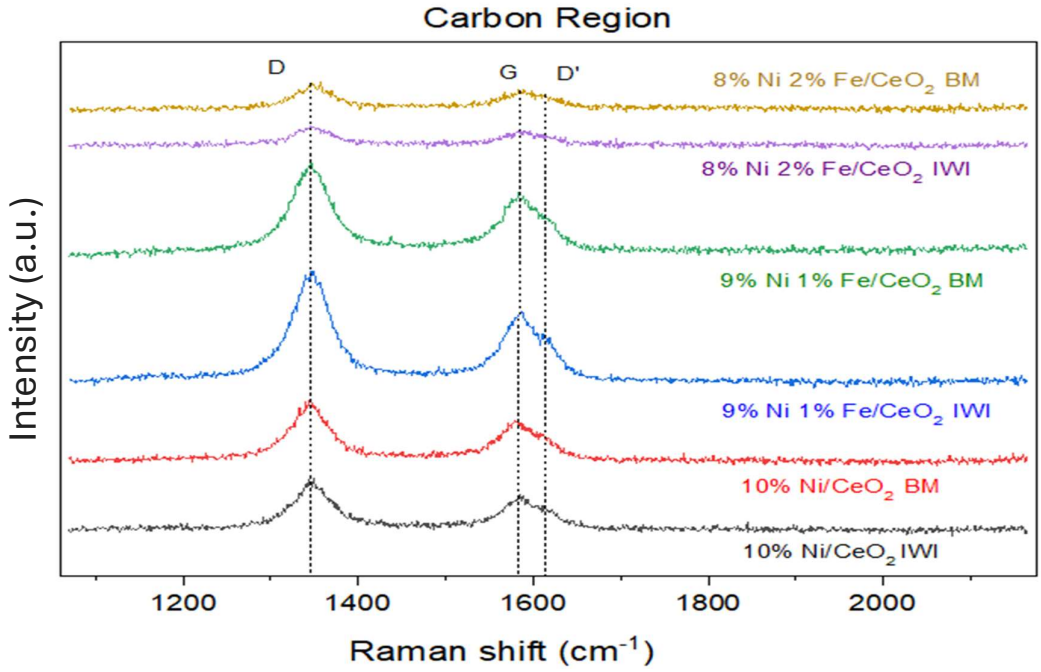

***Figure 42**: Raman spectra of the carbon region for post-reaction catalysts.*

The analysis of these Raman spectra demonstrates that all catalysts exhibit these carbon species to varying degrees, indicating the presence of amorphous carbon, crystalline or graphitic carbon, and polycrystalline graphitic carbon across all samples. The variation in peak intensities among different catalysts reflects differences in the relative amounts and distribution of these carbon components.

Furthermore, the ratio of the D band to the G band intensity, I_D/I_G, is a crucial parameter for estimating the amount of amorphous carbon relative to graphitic carbon (Bokobza et al., 2015). Higher I_D/I_G values suggest a higher proportion of amorphous carbon, which is generally easier to remove and may indicate lower deactiva'oi0ition rates. In contrast, a lower ratio points to a higher relative amount of graphitic carbon, which is more resistant to removal and can contribute to catalyst deactivation and reactor blockage.

***Table 4**: I_D/I_G Ratio for Carbon Deposits on Catalysts Post-DRM Reaction.*

COMPOSITION	I_D/I_G
10 wt% Ni_CeO_2_IWI	1.353
10 wt% Ni_CeO_2_BM	1.313
9 wt% Ni_1 wt% Fe_CeO_2_IWI	1.478
9 wt% Ni_1 wt% Fe_CeO_2_BM	1.363

In conclusion, the post-reaction Raman analysis underscores the presence of various carbon species on catalyst surfaces, with significant implications for their stability and activity in DRM. Managing the formation of undesirable carbon types, particularly graphitic carbon, is essential for prolonging catalyst life and maintaining reactor efficiency.

5.3.2 SEM Characterization

To elucidate the relationship between catalyst morphology and performance, we conducted a comprehensive analysis of two sets of catalysts synthesized via Ball Milling (BM) and Incipient Wet Impregnation (IWI). Scanning Electron Microscopy (SEM) at a resolution of 200 nm was employed to examine the nanoparticle morphology, aggregation, and size distribution both before and after the Dry Reforming of Methane (DRM) reaction.

Prior to the reaction, both ball-milled (BM) and Incipient wet-impregnated (IWI) catalysts exhibited a predominantly spherical morphology. However, differences were observed between the two synthesis methods.

Histograms were constructed to analyze the size distribution of nanoparticles, where each histogram represents the frequency distribution of a total of 50 nanoparticles within specific diameter ranges.

BM catalysts presented a more uniform and homogeneous morphology, with well-dispersed particles of relatively uniform size. This suggests a more controlled synthesis process, resulting in a material with a

higher specific surface area and better accessibility to active sites. As can be clearly seen in Figures 45, 46, and 47, the histograms of particle size distribution confirm this greater uniformity.

In contrast, IWI catalysts exhibited a more heterogeneous morphology, with a greater tendency to form broader particle size distribution. This indicates a less controlled synthesis process, resulting in a material with a lower specific surface area and potentially poorer accessibility to active sites. These initial morphological differences will significantly impact the evolution of the catalysts during the DRM reaction, influencing factors such as sintering, coke deposition, and consequently, catalytic performance.

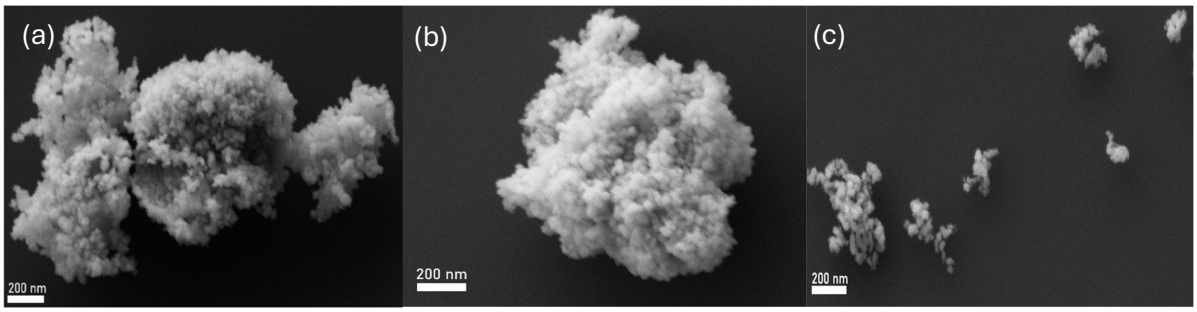

***Figure 43**: SEM images of BM catalysts pre-reaction: a) 10 wt% Ni, b) 9 wt% Ni, 1 wt% Fe, c) 8 wt% Ni, 2 wt% Fe.*

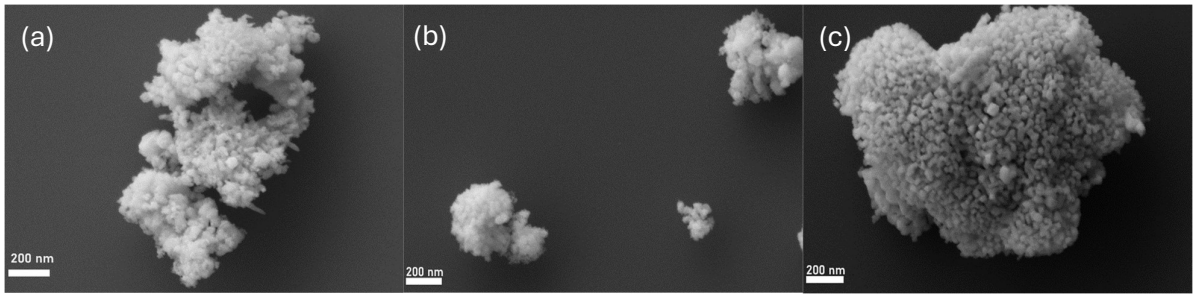

***Figure 44**: SEM images of IWI catalysts pre-reaction: a) 10 wt% Ni, b) 9 wt% Ni, 1 wt% Fe, c) 8 wt% Ni, 2 wt% Fe.*

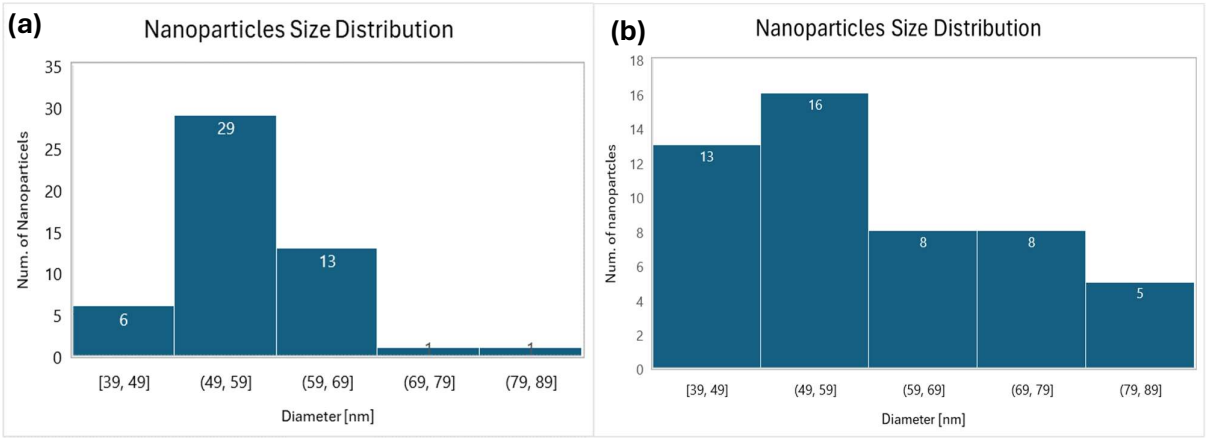

***Figure 45**: Size distribution of 10 wt% Ni nanoparticles pre-reaction prepared by (a) BM and (b) IWI methods.*

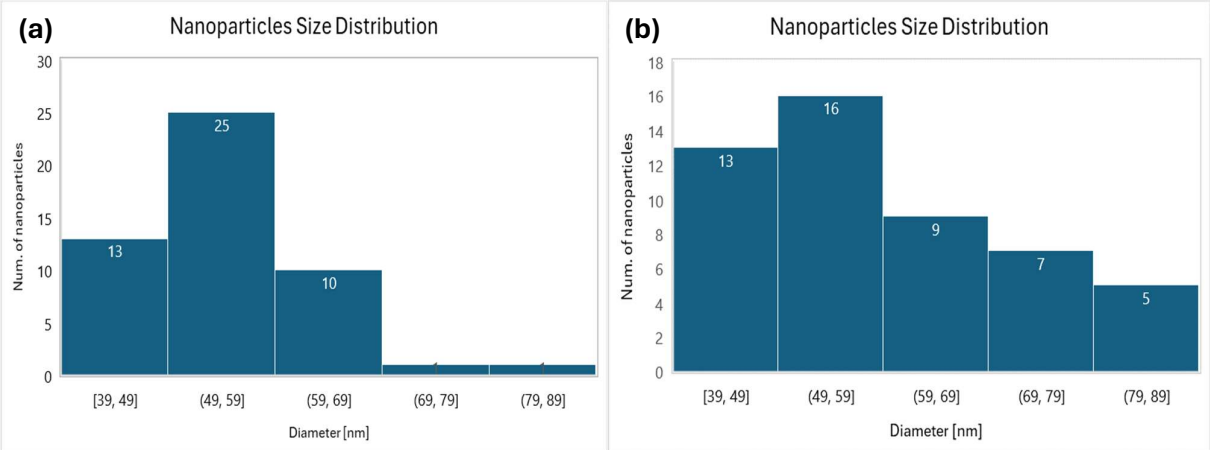

***Figure 46**: Size distribution of 9 wt% Ni and 1 wt% Fe nanoparticles pre-reaction prepared by (a) BM and (b) IWI methods.*

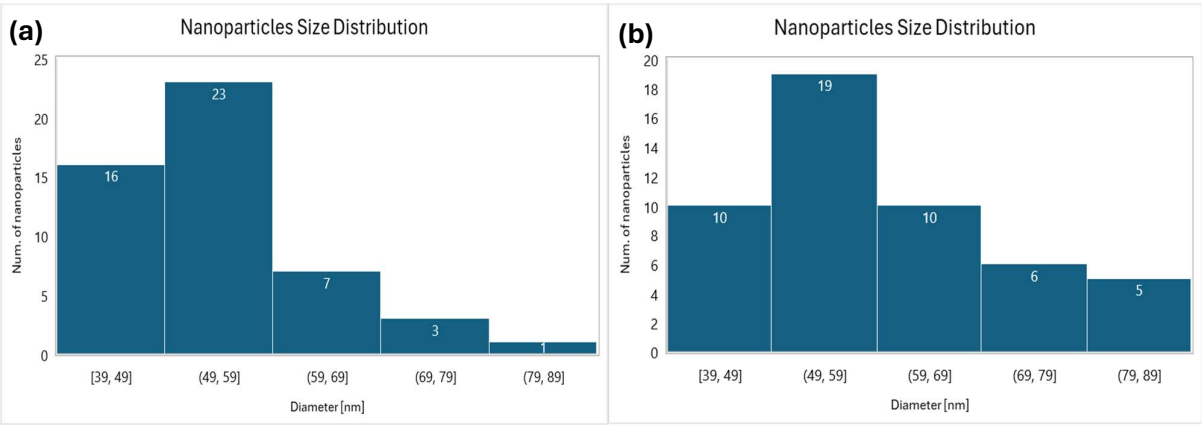

***Figure 47**: Size distribution of 8 wt% Ni and 2 wt% Fe nanoparticles pre-reaction prepared by (a) BM and (b) IWI methods.*

Post-reaction SEM analysis revealed significant morphological alterations in both BM and IWI catalysts. The most prominent changes observed were as follows:

1. *Sintering*: There was a noticeable increase in the size and compactness of nanoparticle clusters in both catalyst types, indicative of sintering of the CeO_2 support. This phenomenon suggests that the particles have undergone coalescence, resulting in the loss of active surface area.
2. *Particle Growth:* Individual particles exhibited increased size and noticeable distortion. This further confirms the occurrence of sintering, as the merging of particles not only increases their size but also alters their shape.
3. *Coke Deposition:* An amorphous layer, likely composed of coke, was detected on the surface of certain particles. This was especially prevalent in the IWI catalysts. The presence of this coke layer is detrimental, as it can block active sites and significantly reduce catalytic efficiency.

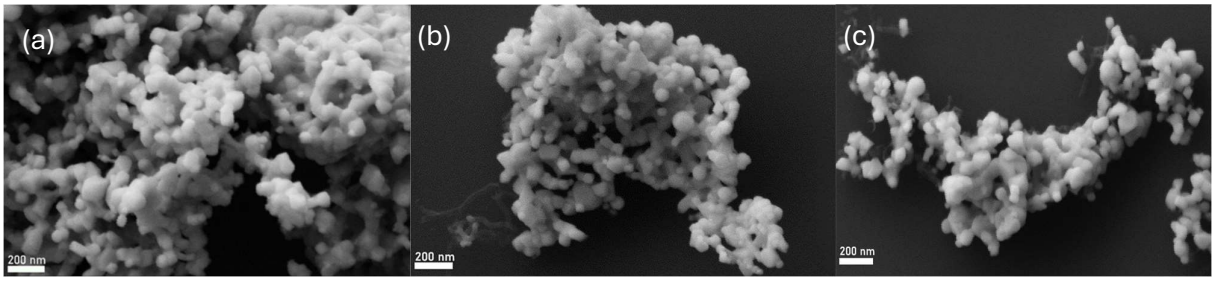

***Figure 48**: SEM images of BM catalysts post-reaction: a) 10 wt% Ni, b) 9 wt% Ni, 1 wt% Fe, c) 8 wt% Ni, 2 wt% Fe.*

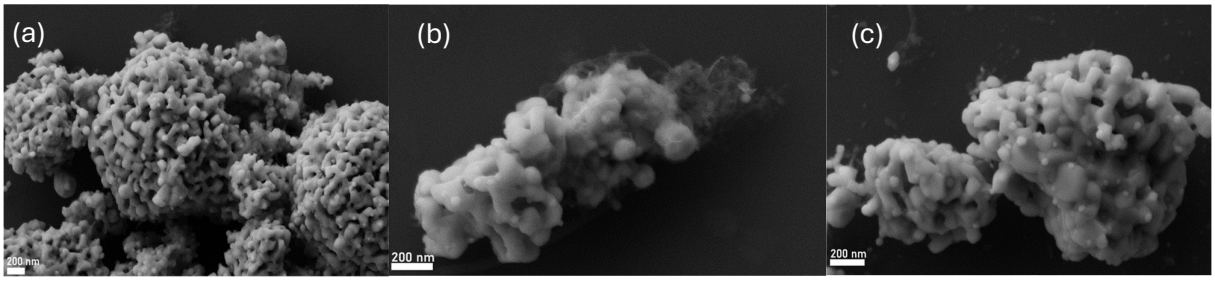

***Figure 49**: SEM images of IWI catalysts post-reaction: a) 10 wt% Ni, b) 9 wt% Ni, 1 wt% Fe, c) 8 wt% Ni, 2 wt% Fe.*

Further particle size distribution analysis supports these findings, showing a broader distribution and a shift towards larger particle sizes for both BM and IWI catalysts after the reaction. This trend, clearly illustrated in Figures 50, 51, and 52, indicates that IWI catalysts experience more extensive sintering and agglomeration, as evidenced by their particle size distribution, which shifts toward slightly larger sizes compared to BM catalysts.

These observations suggest that IWI catalysts are more susceptible to agglomeration and coke deposition, likely due to their initially less uniform morphology, which makes them more vulnerable to structural changes under reaction conditions. This increased susceptibility to morphological changes may also explain the poorer performance of the IWI catalysts in the activity and stability tests. The shift towards larger particle sizes and more pronounced agglomeration reduces the number of accessible active sites, which could account for their reduced efficiency in DRM reactions.

Sintering, agglomeration, and coke deposition degrade the structural integrity and active surface area of the catalysts, leading to diminished catalytic activity. The more severe changes in IWI catalysts correlate with their lower performance, as demonstrated by activity and stability tests.

Future work should focus on developing strategies to mitigate these morphological changes, such as optimizing catalyst preparation methods or introducing additives that prevent sintering and coke formation.

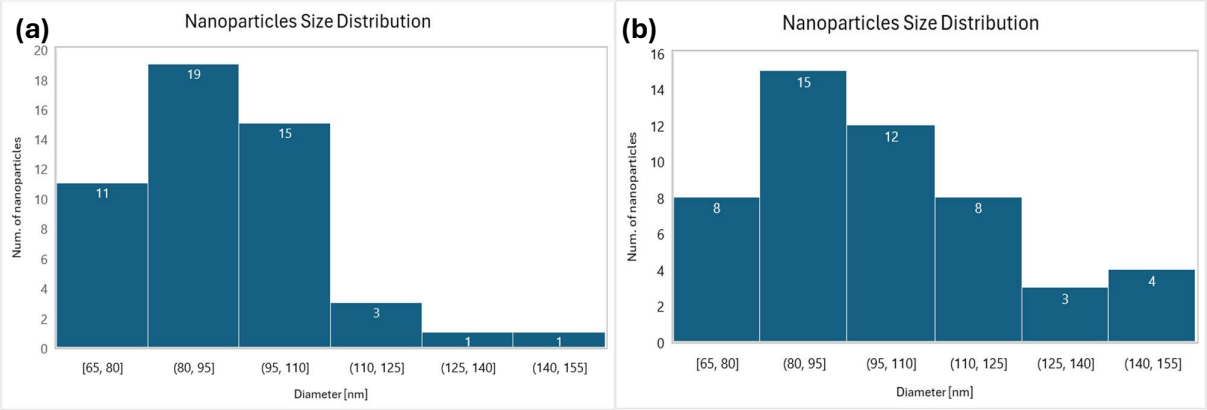

***Figure 50**: Size distribution of 10 wt% Ni nanoparticles post-reaction prepared by (a) BM and (b) IWI methods.*

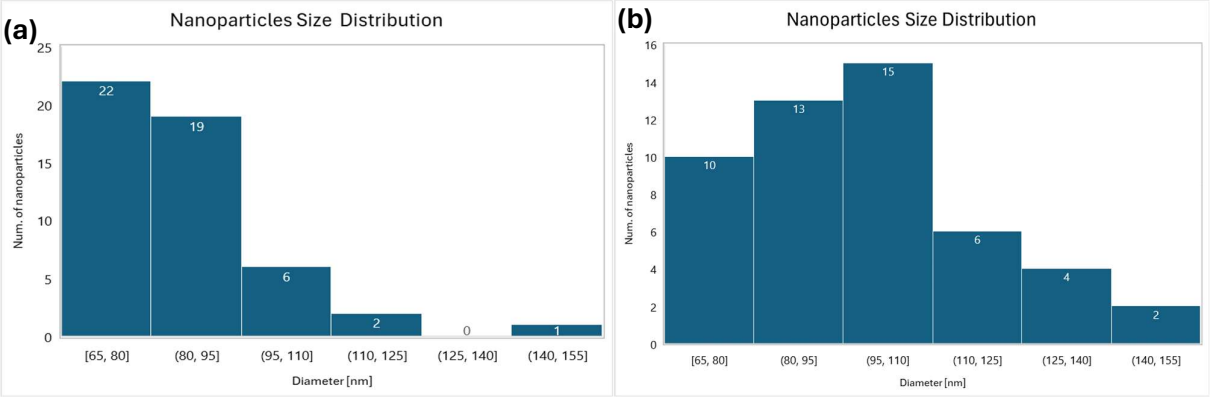

***Figure 51**: Size distribution of 9 wt% Ni and 1 wt% Fe nanoparticles post-reaction prepared by (a) BM and (b) IWI methods.*

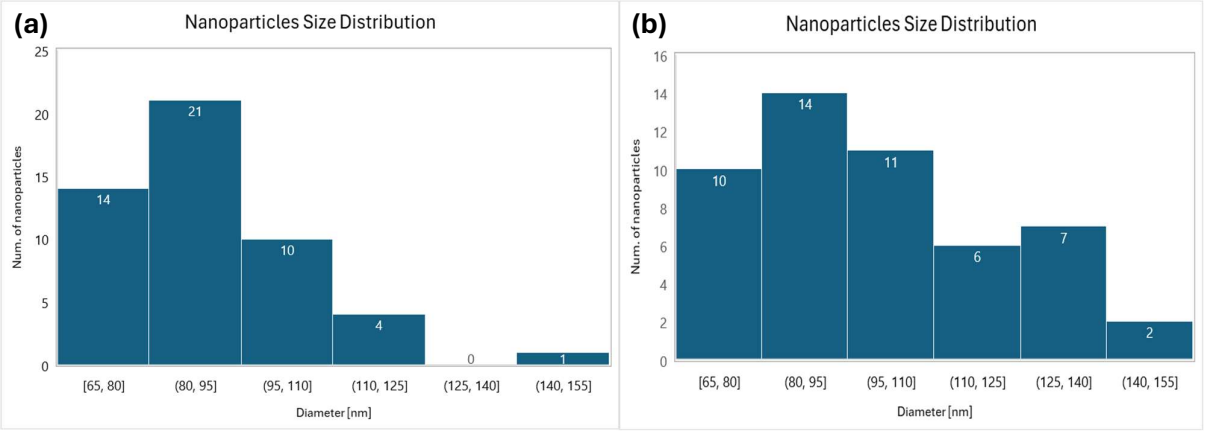

***Figure 52**: Size distribution of 8 wt% Ni and 2 wt% Fe nanoparticles post-reaction prepared by (a) BM and (b) IWI methods.*

In addition to providing insights into the morphological changes of the catalysts, SEM characterization also allows for the investigation of the elemental composition and distribution on the catalyst surface. This is achieved through Energy Dispersive X-ray Spectroscopy (EDS), which identifies the elemental makeup of the samples. Such analysis is particularly valuable for understanding the surface composition and the spatial distribution of various elements within the catalyst.

For the bimetallic catalysts, EDS confirmed the presence of iron, cerium, oxygen, and nickel. However, due to the relatively low quantities of iron (1% and 2% by weight), its precise quantification and distribution present some challenges. Carbon was also detected, which is expected due to its inherent presence in organic materials, and silicon was identified as part of the silicon substrate used for SEM analysis.

Elemental mapping revealed interesting distribution patterns. Carbon was closely aligned with the profiles of the nanoparticles, suggesting that it is either within or on the surface of the nanoparticles. In contrast, silicon was primarily observed at the edges or on the support material, consistent with the use of a silicon wafer to hold the samples during the SEM analysis.

Figures 54, 55, 56 and 57 present the elemental maps and EDS spectra for two representative BM catalysts containing 10 wt% Ni and 8 wt% Ni (with 2 wt% Fe). The results show a strong correlation between the elemental distribution and the observed morphology, reinforcing the findings from the SEM images. Furthermore, it is possible to affirm that there is a good distribution of elements across the surface, suggesting a high degree of homogeneity in the elemental composition of the catalysts.

In Figure 53, the EDS images use different colors to represent the distribution of various elements, allowing for a detailed evaluation of how each element is spread across the surface.

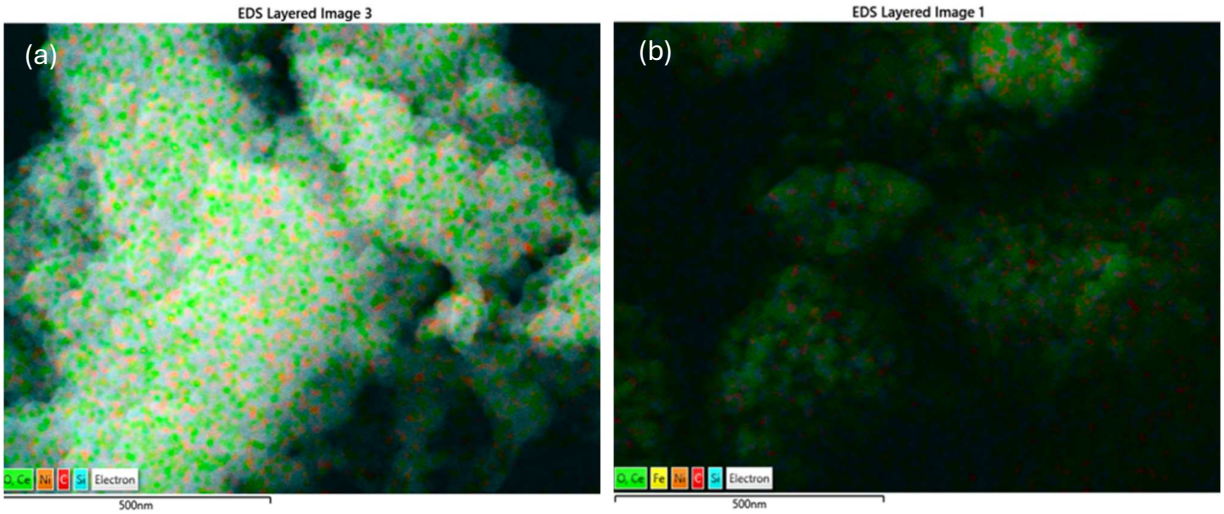

***Figure 53**: ESD images of BM catalysts with a)10 wt% Ni b)8 wt% Ni, 2 wt% Fe.*

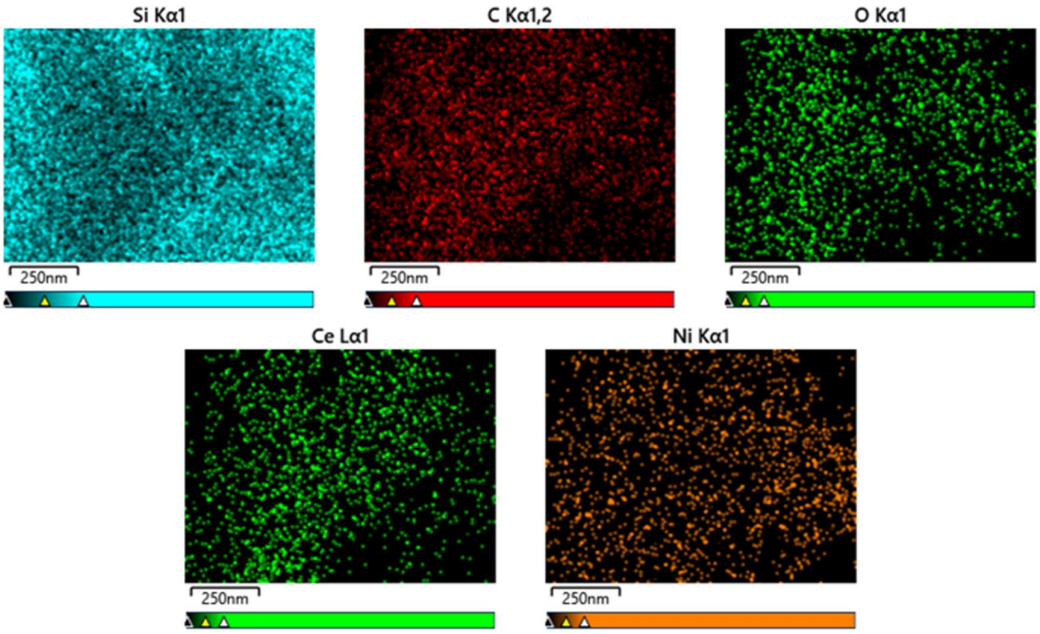

***Figure 54**: Elemental Mapping for BM catalyst with 10 wt% Ni*

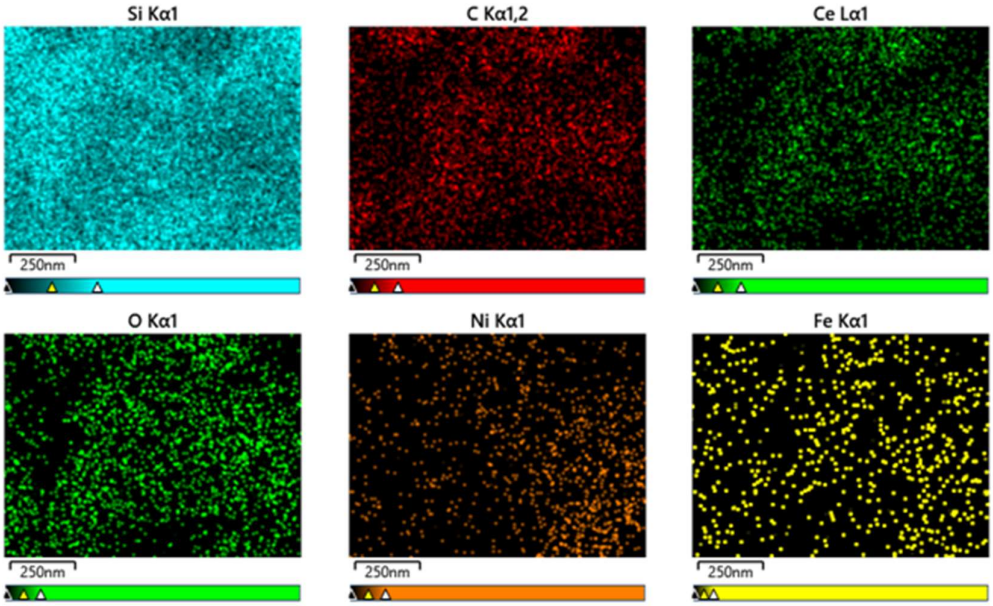

***Figure 55**: Elemental Mapping for BM catalyst with 8 wt% Ni, 2 wt% Fe.*

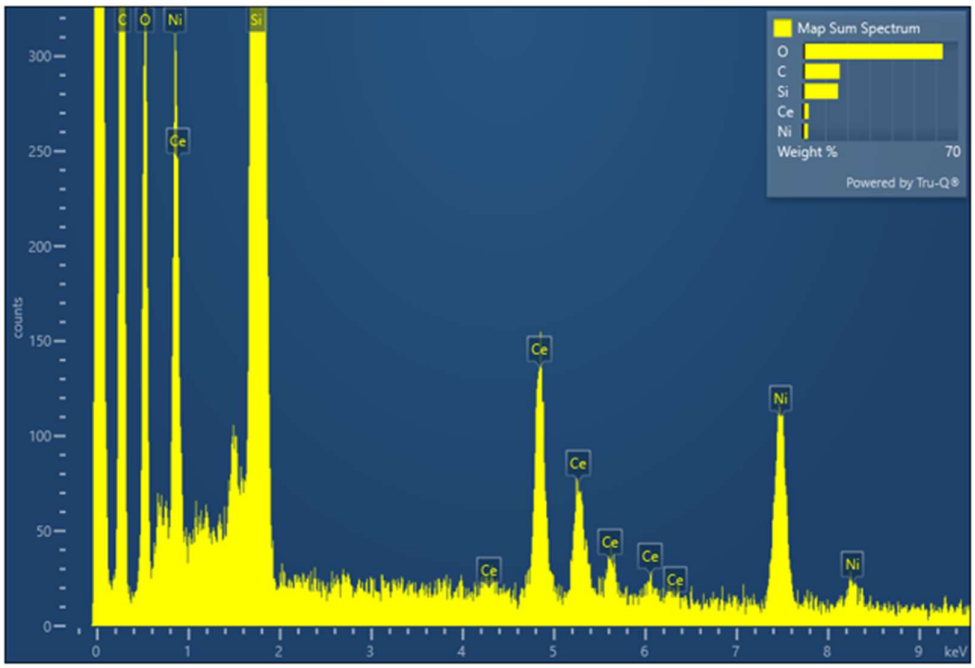

***Figure 56**: EDS spectra for BM catalyst with 10 wt% of Ni.*

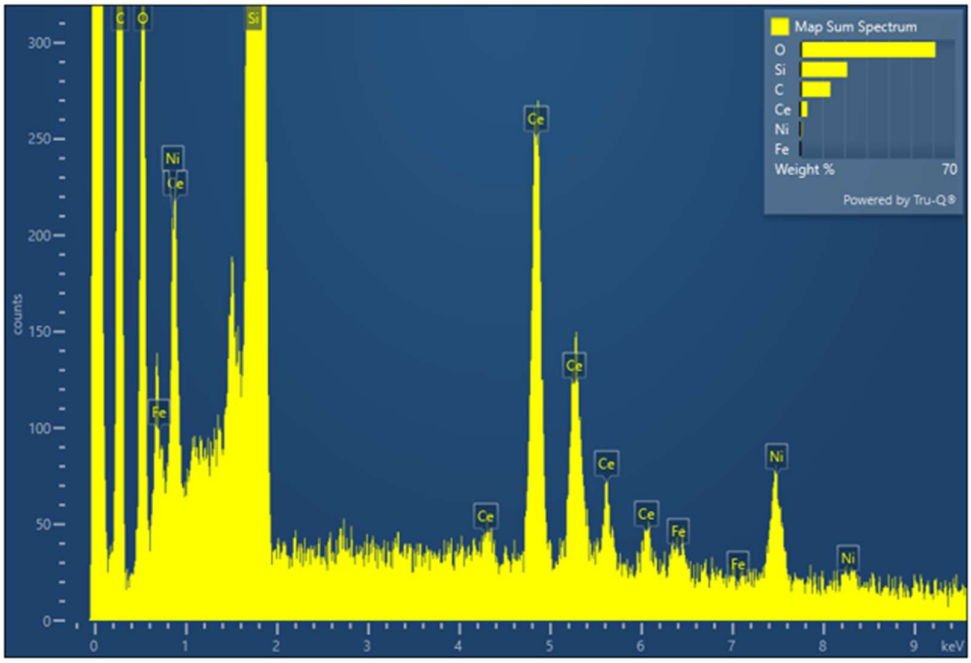

***Figure 57**: EDS spectra for BM catalyst with 8 wt% of Ni, 2 wt% Fe.*

5.3.3 XPS Characterization

X-ray Photoelectron Spectroscopy (XPS) is a powerful analytical technique used to determine the elemental composition and chemical states of elements on the surface of catalysts. For this study, XPS was employed to analyze the surface properties of two catalysts, 8wt% Ni 2wt% Fe-BM and 8wt% Ni 2wt% Fe-IWI, before and after their application in the Dry Reforming of Methane reaction. The primary goal was to understand how the oxidation states of nickel (Ni) and iron (Fe), as well as their surface distribution, influence the catalytic performance in DRM.

In addition to the analysis of the active metals, the oxidation state of cerium (Ce), present in the CeO_2 support, was also examined. This is crucial, as ceria plays a significant role in maintaining redox balance and influencing the interaction between the support and the active metal sites. The oxygen storage capacity (OSC) of ceria, governed by the Ce^{4+}/Ce^{3+} ratio, is key to catalyst stability, particularly in reactions prone to deactivation, such as DRM.

The XPS analysis revealed that nickel is present as Ni^{2+} in all the samples, both before and after the DRM reaction. However, the specific forms of Ni^{2+} differ between the catalysts:

- BM catalyst: Before the DRM reaction, Ni is present exclusively as $Ni(OH)_2$ (100%), suggesting a strong tendency for hydroxide formation under ball-milling conditions. After the reaction, Ni remains in the $Ni(OH)_2$ form, indicating stability of this phase under DRM conditions.
- IWI catalyst: For the IWI-prepared sample, the XPS data show a mixture of $Ni(OH)_2$ (62.9%) and NiO (37.1%) before the reaction. This mixture suggests that the IWI process favors partial oxidation of Ni. After the reaction, there is a slight shift, with $Ni(OH)_2$ at 60.7% and NiO at 39.3%, indicating minimal change in the nickel phases.

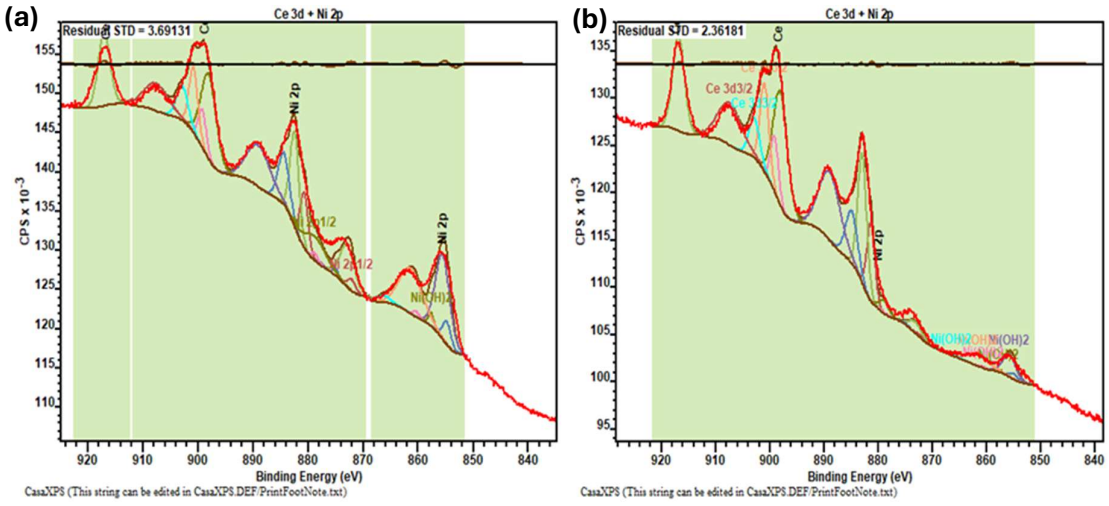

***Figure 58**: XPS spectrum of the Ce 3d and Ni 2p signals for the BM catalyst with background: a) before and b) after the DRM reaction.*

XPS analysis of the cerium oxidation states (Ce^{3+} and Ce^{4+}) highlighted distinct behaviours in the BM and IWI catalysts, both before and after the DRM reaction:

- BM catalyst: The initial Ce^{4+} content was 74.8%, indicating a predominantly oxidized state. After the DRM reaction, this percentage slightly increased to 76.9%, suggesting that the ceria support remained largely stable during the process. This minor increase reflects ceria's ability to maintain its oxygen storage and release capacity, which is essential for preventing carbon deposition and ensuring consistent catalytic performance.
- IWI catalyst: The initial Ce^{4+} content was 81.8%, indicating a more oxidized state compared to the BM catalyst. After the DRM reaction, the Ce^{4+} concentration dropped significantly to 71.5%, suggesting that the ceria support underwent partial reduction, which indicates a lower oxygen storage capacity. This pronounced reduction in cerium oxidation state may point to less effective redox cycling, potentially contributing to faster catalyst deactivation.

This difference in ceria behavior emphasizes the importance of redox properties in maintaining catalyst stability and performance in DRM. The ability of ceria to transition between Ce^{4+} and Ce^{3+} is vital for preventing coke formation and sustaining the activity of active metal sites, such as nickel and iron, throughout the reaction.

The XPS spectra of Fe 2p show distinct differences in the oxidation states of iron between the catalysts:

- BM catalyst: Before the reaction, this catalyst exhibits a small amount of metallic iron (Fe) at 13.1% and a predominant presence of Fe^{2+} at 86.9%, with no detectable Fe^{3+}. This mixture suggests that the ball milling process promotes a reducing environment or prevents the complete oxidation of Fe, potentially due to mechanical reduction and limited exposure to oxygen. After the reaction, Fe is entirely in the Fe^{3+} state (100%), indicating a significant oxidation of Fe during the DRM process.
- IWI catalyst: In contrast, this sample before the reaction shows both Fe^{2+} (31.6%) and Fe^{3+} (68.4%) in significant amounts. This indicates that the IWI process might expose Fe to a more oxidative environment or facilitate the formation of higher oxidation states, which could be stabilized by the presence of oxygen or moisture during synthesis. After the reaction, Fe is fully oxidized to Fe^{3+} (100%), similar to the BM post-reaction sample, suggesting that both catalysts experience oxidative conditions during DRM.

In addition, the XPS data also revealed important differences in the Ni/Fe ratio on the surface of the catalysts, which is a crucial parameter influencing catalytic performance. The nominal ratio for these catalysts was intended to be 4, based on the theoretical composition. However, the XPS data indicates that the actual Ni/Fe ratio on the surface is lower than 4 for all samples, especially after the reaction. It is important to note that XPS is a surface characterization technique that typically probes the top 10 nm

of the material. Therefore, the Ni/Fe ratio detected by XPS represents the composition of the surface layers rather than the bulk composition of the catalyst. If the observed surface Ni/Fe ratio is lower than 4, this does not necessarily mean that the overall bulk composition deviates from the intended value. Instead, it suggests that surface dynamics, such as segregation, diffusion, or selective reduction/oxidation, have altered the surface concentration of Ni and Fe.

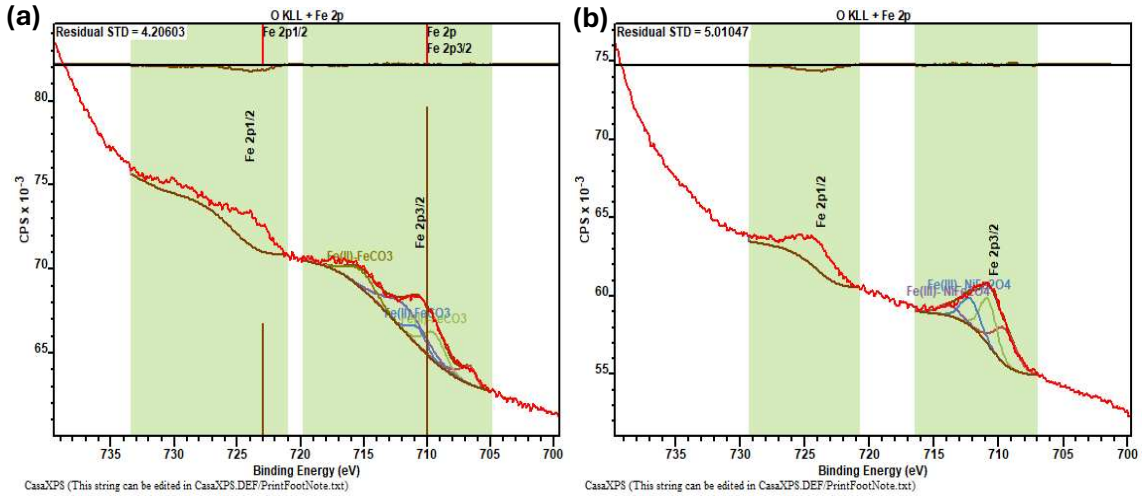

***Figure 59**: XPS spectrum of the Fe 2p signal for the BM catalyst with background: a) before and b) after the DRM reaction.*

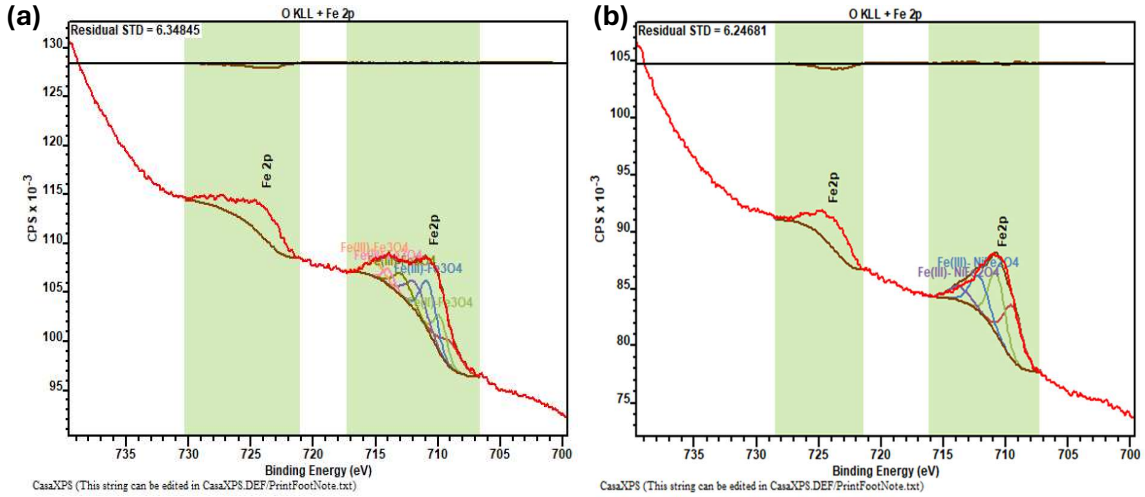

***Figure 60**: XPS spectrum of the Fe 2p signal for the IWI catalyst with background: a) before and b) after the DRM reaction.*

- BM catalyst: The initial Ni/Fe ratio before the reaction is 2.8, which is lower than expected. This could imply a preferential segregation of Fe to the surface or a higher surface dispersion of Ni. After the reaction, the Ni/Fe ratio significantly drops to 0.7, indicating a substantial

enrichment of Fe on the surface or a loss of Ni, possibly due to sintering or other reaction dynamics.

- IWI catalyst: Similarly, this sample shows a Ni/Fe ratio of 2.2 before the reaction, and 1.1 after the reaction. The decrease in the Ni/Fe ratio suggests that Fe is more stable on the surface or that Ni is more prone to sintering or reduction, leading to a change in the surface composition under DRM conditions.

A higher Ni/Fe ratio generally indicates a greater number of Ni active sites available for methane activation, which is crucial for effective DRM performance. The lower-than-expected Ni/Fe ratios observed in both catalysts suggest a reduced number of active sites on the surface, potentially impacting their catalytic efficiency. Nevertheless, the BM catalyst, with a higher initial Ni/Fe ratio compared to the IWI one, indicates a relatively greater availability of Ni sites, potentially contributing to its superior catalytic performance during the activity and stability tests. Additionally, BM catalyst benefits from a synergistic effect between different Fe oxidation states (Fe and Fe^{2+}) and the presence of Ni in the form of $Ni(OH)_2$. This combination is particularly effective in enhancing the activation of both CH_4 and CO_2 while also aiding in the management of carbon deposits. The presence of Fe facilitates CO_2 dissociation, while Fe^{2+} helps in the removal of carbon from the catalyst surface, thus maintaining catalytic activity (Kim et al., 2017).

In summary, the BM catalyst not only exhibits superior initial activity due to its higher Ni/Fe ratio but also maintains its performance over time, making it a more effective and stable catalyst for DRM than the IWI catalyst. This combination of activity and stability underpins its potential for long-term use in methane reforming processes.

***Table 5**: Ni/Fe Ratio and Oxidation States of Bimetallic Catalysts.*

			%Ni II		**% Fe**		
Sample Id	**Ni/Fe**	**%CeIV**	**$Ni(OH)_2$**	**NiO**	**Fe(0)**	**%Fe II**	**%Fe III**
BM catalyst-Before reaction	2.8	74.8	100	-	13.1	86.9	-
BM catalyst-After reaction	0.7	76.9	100	-	-	-	100
IWI catalyst-Before reaction	2.2	81.8	62.9	37.1	-	31.6	68.4
IWI catalyst-After reaction	1.1	71.5	60.7	39.3	-	-	100

Conclusions

Addressing the urgent need for sustainable methane reforming, this study explored the potential of Ni and Fe-based catalysts as cost-effective alternatives to noble metals. By comparing different compositions and synthesis methods, we aimed to develop catalysts capable of delivering high performance while being more economically and environmentally viable.

Our investigation focused on six Ni-based catalysts supported on high surface area CeO_2, evaluating how can different synthesis methods, metal compositions, and reaction temperatures affect catalytic activity, selectivity, and stability. The bimetallic catalyst prepared by Ball Milling (BM), containing 8 wt% Ni and 2 wt% Fe with a $^{Ni}/_{Fe}$ atomic ratio of 3.81, demonstrated exceptional performance, outperforming both monometallic and Incipient Wetness Impregnation (IWI)-prepared catalysts. At 700°C, the BM catalyst achieved a 30% higher CH_4 conversion compared to the monometallic Ni catalyst with 10 wt% Ni, thanks to the synergistic effects of Ni and Fe, which enhance the activation of CH_4 and CO_2.

Activity tests from 550°C to 950°C showed that the BM catalyst consistently surpassed the IWI-prepared catalysts. Even at higher temperatures (750°C to 800°C), where deactivation is more pronounced, the BM catalyst maintained about 10% higher CH_4 conversion than the IWI catalyst, despite gradual deactivation.

Selectivity, assessed through the H_2/CO ratio, was notably higher for the bimetallic catalyst with increased Fe content at medium to high temperatures, reflecting a consistent trend across synthesis methods. However, selectivity results were similar for both bimetallic catalysts with higher Fe content, suggesting that the synthesis method affects activity, while selectivity is primarily influenced by the composition of active sites.

Characterization studies provided crucial insights into why the BM catalyst performs better. X-ray Photoelectron Spectroscopy (XPS) revealed that the BM catalyst had a higher concentration of Ni active sites, which is vital for superior catalytic performance. Notably, the ceria oxidation state analysis indicated that the BM catalyst maintained greater stability in Ce^{4+} content compared to the IWI catalyst, supporting its enhanced performance. Scanning Electron Microscopy (SEM) showed that the BM catalysts had smaller, more uniform particles post-reaction, which reduced sintering and agglomeration. Raman Spectroscopy further elucidated these findings by indicating stronger metal-support interactions in the BM-prepared catalysts. This was evident from the more intense peaks in the Raman spectra, which signaled enhanced interactions between Ni and CeO_2. Additionally, post-reaction Raman analysis

confirmed the presence of both amorphous and crystalline carbon on the catalyst surfaces, consistent with SEM observations of carbon deposition. The BM catalysts exhibited less severe carbon deposition compared to IWI-prepared catalysts, contributing to their improved stability and performance.

These results highlight the ball milling method as a sustainable and effective approach for synthesizing high-performance DRM catalysts by one-step mechanochemistry, without the need of using additional reactants and harmful solvents, which is quite common in the conventional IWI methods. Bimetallic catalysts using non-noble metals like Ni and Fe offer a viable and eco-friendly alternative, showing significant potential for advancing methane reforming technologies.

Building on these findings, future research should focus on several key areas to enhance the performance and stability of DRM catalysts:

1. *Catalyst Composition Optimization:* Further investigation into the optimal Ni/Fe ratio is essential. Future studies should explore the use of different Ni and Fe precursors, the introduction of additional promoters, such as alkali or alkaline earth metals, to improve oxygen mobility and reduce carbon formation, thereby enhancing catalytic stability.

2. *Catalyst fabrication optimization:* Once the Ni/Fe ratio has been optimized, a new series of experiments should be performed to check and validate the optimal ball milling parameters (frequency, Ball-to-powder ratio, milling time, sequential addition of the metal precursors to CeO_2 instead of adding them in a single step) in order to enhance the catalytic performance and achieve the best metal-support interaction.

3. *Support Modification:* Although CeO_2 has shown promising results, alternative supports like ZrO_2 or Al_2O_3 may offer superior thermal stability and resistance to sintering. Modifying support properties to enhance interactions with active metal sites could lead to more resilient catalysts.

4. *Deactivation Mitigation:* Carbon deposition remains a significant challenge for DRM catalysts. Investigating additives like cerium or lanthanum, which may help reduce carbon buildup, is a promising strategy. Additionally, optimizing reactor conditions, including feed composition and temperature cycling, could prevent excessive carbon formation and improve long-term stability.

By addressing these critical areas, future research can advance the development of more efficient, stable, and sustainable catalysts for DRM. Such advancements will be vital in transforming methane and CO_2, both potent greenhouse gases, into valuable chemical feedstocks, thus supporting the transition toward a low-carbon economy.

Bibliography

Alhassan, A. M., Hussain, I., Taialla, O. A., Awad, M. M., Tanimu, A., Alhooshani, K., & Ganiyu, S. A. (2023). Advances in catalytic dry reforming of methane (DRM): Emerging trends, current challenges, and future perspectives. *Journal of Cleaner Production*, *423*, 138638. https://doi.org/10.1016/j.jclepro.2023.138638

Aozasa, S. (Anan, J. R. E. (Sainte S. F. D. L. (Osaka, J. P. B. (Nishinomiya, J. (2008). *Ceric oxide and method for production thereof, and catalyst for exhaust gas clarification*. https://www.freepatentsonline.com/7361322.html

Aramouni, N. A. K., Touma, J. G., Tarboush, B. A., Zeaiter, J., & Ahmad, M. N. (2018a). Catalyst design for dry reforming of methane: Analysis review. *Renewable and Sustainable Energy Reviews*, *82*, 2570–2585. https://doi.org/10.1016/j.rser.2017.09.076

Aramouni, N. A. K., Touma, J. G., Tarboush, B. A., Zeaiter, J., & Ahmad, M. N. (2018b). Catalyst design for dry reforming of methane: Analysis review. *Renewable and Sustainable Energy Reviews*, *82*, 2570–2585. https://doi.org/10.1016/j.rser.2017.09.076

Aziz, M. A. A., Setiabudi, H. D., Teh, L. P., Annuar, N. H. R., & Jalil, A. A. (2019). A review of heterogeneous catalysts for syngas production via dry reforming. *Journal of the Taiwan Institute of Chemical Engineers*, *101*, 139–158. https://doi.org/10.1016/j.jtice.2019.04.047

Bahari, M. B., Mamat, C. R., Jalil, A. A., Hassan, N. S., Hatta, A. H., Alhassan, M., Aziz, M. A., Le, V. G., Siang, T. J., & Timmiati, S. N. (2024). Mitigating deactivation in dry methane reforming by lanthanum catalysts for enhanced hydrogen production: A review. *International Journal of Hydrogen Energy*. https://doi.org/10.1016/j.ijhydene.2024.06.122

Baláž, P., Achimovičová, M., Baláž, M., Billik, P., Cherkezova-Zheleva, Z., Criado, J. M., Delogu, F., Dutková, E., Gaffet, E., Gotor, F. J., Kumar, R., Mitov, I., Rojac, T., Senna, M., Streletskii, A., & Wieczorek-Ciurowa, K. (2013). Hallmarks of mechanochemistry: from nanoparticles to technology. *Chemical Society Reviews*, *42*(18), 7571. https://doi.org/10.1039/c3cs35468g

Bartholomew, C. H. (2001). Mechanisms of catalyst deactivation. *Applied Catalysis A: General*, *212*(1–2), 17–60. https://doi.org/10.1016/S0926-860X(00)00843-7

Bokobza, L., Bruneel, J.-L., & Couzi, M. (2015). Raman Spectra of Carbon-Based Materials (from Graphite to Carbon Black) and of Some Silicone Composites. *C*, *1*(1), 77–94. https://doi.org/10.3390/c1010077

Bokov, D., Turki Jalil, A., Chupradit, S., Suksatan, W., Javed Ansari, M., Shewael, I. H., Valiev, G. H., & Kianfar, E. (2021). Nanomaterial by Sol-Gel Method: Synthesis and Application. *Advances in Materials Science and Engineering*, *2021*, 1–21. https://doi.org/10.1155/2021/5102014

Bossel, U., & Eliasson, B. (n.d.). *Energy Hydrogen Economy*.

bp. (n.d.). *bp Energy Outlook 2023*. Retrieved April 8, 2024, from https://www.bp.com/content/dam/bp/business-sites/en/global/corporate/pdfs/energy-economics/energy-outlook/bp-energy-outlook-2023.pdf

Braga, A., Armengol-Profitós, M., Pascua-Solé, L., Vendrell, X., Soler, L., Serrano, I., Villar-Garcia, I. J., Pérez-Dieste, V., Divins, N. J., & Llorca, J. (2023). Bimetallic NiFe Nanoparticles Supported on CeO_2 as Catalysts for Methane Steam Reforming. *ACS Applied Nano Materials*, *6*(9), 7173–7185. https://doi.org/10.1021/acsanm.3c00104

Bumajdad, A., Eastoe, J., & Mathew, A. (2009). Cerium oxide nanoparticles prepared in self-assembled systems. *Advances in Colloid and Interface Science*, *147–148*, 56–66. https://doi.org/10.1016/j.cis.2008.10.004

Cam, T. S., Omarov, S. O., Chebanenko, M. I., Izotova, S. G., & Popkov, V. I. (2022). Recent progress in the synthesis of CeO2-based nanocatalysts towards efficient oxidation of CO. *Journal of Science: Advanced Materials and Devices*, *7*(1), 100399. https://doi.org/10.1016/j.jsamd.2021.11.001

Castro-Dominguez, B., Mardilovich, I., Ma, L.-C., Ma, R., Dixon, A., Kazantzis, N., & Ma, Y. (2016). Integration of Methane Steam Reforming and Water Gas Shift Reaction in a Pd/Au/Pd-Based Catalytic Membrane Reactor for Process Intensification. *Membranes*, *6*(3), 44. https://doi.org/10.3390/membranes6030044

Cesário, M. R., Barros, B., Aouad, S., Gennequin, C., Abi-Aad, E., & Macedo, D. A. (2022). Understanding heterogeneous catalysis: A brief study on performance parameters. In *Heterogeneous Catalysis* (pp. 1–18). Elsevier. https://doi.org/10.1016/B978-0-323-85612-6.00001-2

Christopher A. Badurek. (2024). Biogas. In *Encyclopedia Britannica*. https://www.britannica.com/technology/biogas

Cimino, & Lisi. (2019). Catalyst Deactivation, Poisoning and Regeneration. *Catalysts*, *9*(8), 668. https://doi.org/10.3390/catal9080668

Egerton, R. F. (2016). *Physical Principles of Electron Microscopy*. Springer International Publishing. https://doi.org/10.1007/978-3-319-39877-8

Eric Hand. (2023). HIDDEN HYDROGEN. *Science*.

European Commission. (n.d.). *Progress on climate action* . https://climate.ec.europa.eu/eu-action/climate-strategies-targets/progress-climate-action_en

Filonchyk, M., Peterson, M. P., Zhang, L., Hurynovich, V., & He, Y. (2024). Greenhouse gases emissions and global climate change: Examining the influence of CO2, CH4, and N2O. *Science of The Total Environment*, *935*, 173359. https://doi.org/10.1016/j.scitotenv.2024.173359

Freni, S., Calogero, G., & Cavallaro, S. (2000). Hydrogen production from methane through catalytic partial oxidation reactions. *Journal of Power Sources*, *87*(1–2), 28–38. https://doi.org/10.1016/S0378-7753(99)00357-2

Hermesmann, M., & Müller, T. E. (2022). Green, Turquoise, Blue, or Grey? Environmentally friendly Hydrogen Production in Transforming Energy Systems. *Progress in Energy and Combustion Science*, *90*, 100996. https://doi.org/10.1016/j.pecs.2022.100996

Hess, C. (2013). In situ Raman spectroscopy of catalysts: Examples from current research. *Topics in Catalysis*, *56*(15–17), 1593–1600. https://doi.org/10.1007/s11244-013-0138-7

Hutchings, G. J., & Védrine, J. C. (2004). *Heterogeneous Catalyst Preparation* (pp. 215–258). https://doi.org/10.1007/978-3-662-05981-4_6

Hydrogen | H2 | CID 783 - PubChem. (n.d.). Retrieved April 8, 2024, from https://pubchem.ncbi.nlm.nih.gov/compound/783#section=Heat-of-Vaporization

Internation Energy Agency. (2023). *Global Hydrogen Review 2023*.

Jameel, M. K., Mustafa, M. A., Ahmed, H. S., Mohammed, A. jassim, Ghazy, H., Shakir, M. N., Lawas, A. M., Mohammed, S. khudhur, Idan, A. H., Mahmoud, Z. H., Sayadi, H., & Kianfar, E. (2024). Biogas: Production, properties, applications, economic and challenges: A review. *Results in Chemistry*, *7*, 101549. https://doi.org/10.1016/j.rechem.2024.101549

Jordan, T. (2022). Hydrogen technologies. In *Hydrogen Safety for Energy Applications* (pp. 25–115). Elsevier. https://doi.org/10.1016/B978-0-12-820492-4.00005-1

Khajenoori, M., Rezaei, M., & Nematollahi, B. (2013). Preparation of noble metal nanocatalysts and their applications in catalytic partial oxidation of methane. *Journal of Industrial and Engineering Chemistry*, *19*(3), 981–986. https://doi.org/10.1016/j.jiec.2012.11.020

Khosravani, H., Meshksar, M., Rahimpour, H. R., & Rahimpour, M. R. (2023). Introduction to syngas products and applications. In *Advances in Synthesis Gas : Methods, Technologies and Applications* (pp. 3–25). Elsevier. https://doi.org/10.1016/B978-0-323-91878-7.00014-9

Kim, S. M., Abdala, P. M., Margossian, T., Hosseini, D., Foppa, L., Armutlulu, A., van Beek, W., Comas-Vives, A., Copéret, C., & Müller, C. (2017). Cooperativity and Dynamics Increase the Performance of NiFe Dry Reforming Catalysts. *Journal of the American Chemical Society*, *139*(5), 1937–1949. https://doi.org/10.1021/jacs.6b11487

Kosacki, I., Suzuki, T., Anderson, H. U., & Colomban, P. (2002). Raman scattering and lattice defects in nanocrystalline CeO2 thin films. *Solid State Ionics*, *149*(1–2), 99–105. https://doi.org/10.1016/S0167-2738(02)00104-2

Ladna, & Gam, L. (2010). The Importance of Natural Gas Reforming. In *Natural Gas*. Sciyo. https://doi.org/10.5772/9824

Leofanti, G., Tozzola, G., Padovan, M., Petrini, G., Bordiga, S., & Zecchina, A. (1997). Catalyst characterization: characterization techniques. *Catalysis Today*, *34*(3–4), 307–327. https://doi.org/10.1016/S0920-5861(96)00056-9

Li, D., Nakagawa, Y., & Tomishige, K. (2011). Methane reforming to synthesis gas over Ni catalysts modified with noble metals. *Applied Catalysis A: General*, *408*(1–2), 1–24. https://doi.org/10.1016/j.apcata.2011.09.018

Li, P., Chen, X., Li, Y., & Schwank, J. W. (2019). A review on oxygen storage capacity of CeO2-based materials: Influence factors, measurement techniques, and applications in reactions related to catalytic automotive emissions control. *Catalysis Today*, *327*, 90–115. https://doi.org/10.1016/j.cattod.2018.05.059

Liu, W., Wang, W., Tang, K., Guo, J., Ren, Y., Wang, S., Feng, L., & Yang, Y. (2016). The promoting influence of nickel species in the controllable synthesis and catalytic properties of nickel–ceria catalysts. *Catalysis Science & Technology*, *6*(7), 2427–2434. https://doi.org/10.1039/C5CY01241D

Manan, W. N., Wan Isahak, W. N. R., & Yaakob, Z. (2022a). CeO2-Based Heterogeneous Catalysts in Dry Reforming Methane and Steam Reforming Methane: A Short Review. *Catalysts*, *12*(5), 452. https://doi.org/10.3390/catal12050452

Manan, W. N., Wan Isahak, W. N. R., & Yaakob, Z. (2022b). CeO2-Based Heterogeneous Catalysts in Dry Reforming Methane and Steam Reforming Methane: A Short Review. *Catalysts*, *12*(5), 452. https://doi.org/10.3390/catal12050452

Manna, J. (2024). Hydrogen economy and international hydrogen strategies. In *Towards Hydrogen Infrastructure* (pp. 3–38). Elsevier. https://doi.org/10.1016/B978-0-323-95553-9.00009-1

Maria Valenti. (2009). *Produzione di idrogeno per via solare*. http://www.fedoa.unina.it/3625/1/Tesi_dottorato_MARIA_VALENTI.pdf

Martín, A. J., Mitchell, S., Mondelli, C., Jaydev, S., & Pérez-Ramírez, J. (2022). Unifying views on catalyst deactivation. *Nature Catalysis*, *5*(10), 854–866. https://doi.org/10.1038/s41929-022-00842-y

Mehrabadi, B. A. T., Eskandari, S., Khan, U., White, R. D., & Regalbuto, J. R. (2017). *A Review of Preparation Methods for Supported Metal Catalysts* (pp. 1–35). https://doi.org/10.1016/bs.acat.2017.10.001

Mhadhbi, M. (2024). The interconnected carbon, fossil fuels, and clean energy markets: Exploring Europe and China's perspectives on climate change. *Finance Research Letters*, *62*, 105185. https://doi.org/10.1016/j.frl.2024.105185

Minardi, E. R., Chakraborty, S., & Curcio, S. (2015). Membrane reactors for dry reforming of methane. In *Membrane Reactors for Energy Applications and Basic Chemical Production* (pp. 99–144). Elsevier. https://doi.org/10.1016/B978-1-78242-223-5.00004-2

Mohd Fadzil, N. A., AB Rahim, M. H., & Pragas Maniam, G. (2018). Brief review of ceria and modified ceria: synthesis and application. *Materials Research Express*, *5*(8), 085019. https://doi.org/10.1088/2053-1591/aad2b5

Morales-Cano, F., Lundegaard, L. F., Tiruvalam, R. R., Falsig, H., & Skjøth-Rasmussen, M. S. (2015). Improving the sintering resistance of Ni/Al 2 O 3 steam-reforming catalysts by promotion with noble metals. *Applied Catalysis A: General*, *498*, 117–125. https://doi.org/10.1016/j.apcata.2015.03.016

Moulder, J. F. ., & Chastain, Jill. (1992). *Handbook of x-ray photoelectron spectroscopy : a reference book of standard spectra for identification and interpretation of XPS data*. Physical Electronics Division, Perkin-Elmer Corp.

OHTAKE, N., KATOH, M., & SUGIYAMA, S. (2017). High thermal-stability ceria synthesized via thermal-hydrolysis route and methane-combustion performance. *Journal of the Ceramic Society of Japan*, *125*(2), 57–61. https://doi.org/10.2109/jcersj2.16255

Pakhare, D., & Spivey, J. (2014). A review of dry (CO_2) reforming of methane over noble metal catalysts. *Chem. Soc. Rev.*, *43*(22), 7813–7837. https://doi.org/10.1039/C3CS60395D

Poggio-Fraccari, E., Abele, A., Zitta, N., Francesconi, J., & Mariño, F. (2022). CO removal for hydrogen purification via Water Gas Shift and COPROX reactions with monolithic catalysts. *Fuel*, *310*, 122419. https://doi.org/10.1016/j.fuel.2021.122419

Population Pyramids of the World from 1950 to 2100. (n.d.). Retrieved April 8, 2024, from https://www.populationpyramid.net/

Prochazka, M. (2016). *Basics of Raman Scattering (RS) Spectroscopy* (pp. 7–19). https://doi.org/10.1007/978-3-319-23992-7_2

Roduner, E. (n.d.). *Understanding Catalysis*.

Rogers Kara. (2023). Syngas. In *Encyclopedia Britannica*. https://www.britannica.com/topic/syngas

Scheller, F., Wald, S., Kondziella, H., Gunkel, P. A., Bruckner, T., & Keles, D. (2023). Future role and economic benefits of hydrogen and synthetic energy carriers in Germany: a review of long-term energy scenarios. *Sustainable Energy Technologies and Assessments*, *56*, 103037. https://doi.org/10.1016/j.seta.2023.103037

Seck, G. S., Hache, E., D'Herbemont, V., Guyot, M., & Malbec, L.-M. (2023a). Hydrogen development in Europe: Estimating material consumption in net zero emissions scenarios. *International Economics*, *176*, 100457. https://doi.org/10.1016/j.inteco.2023.100457

Seck, G. S., Hache, E., D'Herbemont, V., Guyot, M., & Malbec, L.-M. (2023b). Hydrogen development in Europe: Estimating material consumption in net zero emissions scenarios. *International Economics*, *176*, 100457. https://doi.org/10.1016/j.inteco.2023.100457

Sinar Mashuri, S. I., Ibrahim, M. L., Kasim, M. F., Mastuli, M. S., Rashid, U., Abdullah, A. H., Islam, A., Asikin Mijan, N., Tan, Y. H., Mansir, N., Mohd Kaus, N. H., & Yun Hin, T.-Y. (2020). Photocatalysis for Organic Wastewater Treatment: From the Basis to Current Challenges for Society. *Catalysts*, *10*(11), 1260. https://doi.org/10.3390/catal10111260

Stevie, F. A., & Donley, C. L. (2020a). Introduction to x-ray photoelectron spectroscopy. *Journal of Vacuum Science & Technology A: Vacuum, Surfaces, and Films*, *38*(6). https://doi.org/10.1116/6.0000412

Stevie, F. A., & Donley, C. L. (2020b). Introduction to x-ray photoelectron spectroscopy. *Journal of Vacuum Science & Technology A: Vacuum, Surfaces, and Films*, *38*(6). https://doi.org/10.1116/6.0000412

Thambiliyagodage, C., & Wijesekera, R. (2022). Ball milling – A green and sustainable technique for the preparation of titanium based materials from ilmenite. *Current Research in Green and Sustainable Chemistry*, *5*, 100236. https://doi.org/10.1016/j.crgsc.2021.100236

Theofanidis, S. A., Poelman, H., Marin, G. B., & Galvita, V. V. (2019). How Does the Surface Structure of Ni-Fe Nanoalloys Control Carbon Formation During Methane Steam/Dry Reforming? In *Advanced Nanomaterials for Catalysis and Energy* (pp. 177–225). Elsevier. https://doi.org/10.1016/B978-0-12-814807-5.00006-1

Velasco-Vélez, J. J., Pfeifer, V., Hävecker, M., Wang, R., Centeno, A., Zurutuza, A., Algara-Siller, G., Stotz, E., Skorupska, K., Teschner, D., Kube, P., Braeuninger-Weimer, P., Hofmann, S., Schlögl, R., & Knop-Gericke, A. (2016). Atmospheric pressure X-ray photoelectron spectroscopy apparatus: Bridging the pressure gap. *Review of Scientific Instruments*, *87*(5). https://doi.org/10.1063/1.4951724

Vladár, A. E., & Hodoroaba, V.-D. (2020). Characterization of nanoparticles by scanning electron microscopy. In *Characterization of Nanoparticles* (pp. 7–27). Elsevier. https://doi.org/10.1016/B978-0-12-814182-3.00002-X

Wan Xiu-Mei, Chen Chen, Fan Zhi-Bo, Lu Dan-Feng, Gao Ran, & Qi Zhi-Mei. (2016). Raman spectroscopy based on plasmon waveguide prepared with mesoporous TiO2 thin film. *Acta Physica Sinica*, *65*(13), 137801. https://doi.org/10.7498/aps.65.137801

Yang, Q., Lu, Z., Liu, J., Lei, X., Chang, Z., Luo, L., & Sun, X. (2013). Metal oxide and hydroxide nanoarrays: Hydrothermal synthesis and applications as supercapacitors and nanocatalysts. *Progress in Natural Science: Materials International*, *23*(4), 351–366. https://doi.org/10.1016/j.pnsc.2013.06.015

YANG, R. (1990). Solubility and diffusivity of carbon in metals. *Journal of Catalysis*, *122*(1), 206–210. https://doi.org/10.1016/0021-9517(90)90273-M

Acknowledgements

Ora che abbiamo concluso questa fase di discussione, voglio dedicare quest'ultimo spazio a ringraziare le persone che hanno reso possibile tutto questo.

Dedico questo traguardo alle persone più importanti della mia vita: i miei genitori. A voi, che avete sempre creduto in me fin dall'inizio, supportandomi in ogni mia scelta. A voi, che mi siete stati vicini nei momenti belli, in cui il vostro affetto mi ha fatta sentire invincibile, e nei momenti difficili, in cui ho capito cosa significhi davvero sentirsi soli. Siete stati il mio punto fermo, la mia guida, la mia eterna fonte di conforto. Mi avete insegnato che nulla nella vita è facile e che dietro ogni traguardo si nascondono fatica, lacrime e anche un po' di coraggio. Questa vittoria è tanto vostra quanto mia, e spero che il raggiungimento di questo obiettivo vi renda orgogliosi, così come voi lo siete sempre stati per me.

Un ringraziamento speciale va a mio fratello Pier, il regalo più bello che mamma e papà potessero farmi. Sei stato per me un punto di riferimento silenzioso ma costante, una presenza che mi ha dato forza anche nei momenti in cui non avevo il coraggio di ammetterne il bisogno. Grazie per la pazienza infinita con cui hai affrontato i miei sbalzi d'umore, per aver sempre trovato un modo per alleggerire l'atmosfera, anche quando la casa sembrava rispecchiare i miei stati d'animo. Il tuo modo di esserci, discreto ma rassicurante, ha significato più di quanto io sia capace di esprimere.

Voglio anche ringraziare tutti gli amici che mi hanno accompagnata in questo viaggio: le amiche di una vita, gli amici torinesi e quelli della parentesi spagnola. Il vostro affetto mi ha spronata a crescere e a inseguire i miei sogni con determinazione. Guardando indietro a questi anni, sono profondamente grata a ciascuno di voi: ogni gesto, ogni parola, ogni risata e confronto ha contribuito a farmi diventare la persona che sono oggi.

Infine, un pensiero va a me stessa. Per aver affrontato questo percorso con dedizione totale. Per aver sposato il motto "andare avanti" a qualunque costo. Per aver trovato il coraggio di sfidare i miei limiti, spingendomi oltre ciò che pensavo possibile.

Attraverso le difficoltà, verso le stelle.

Grazie a tutti.